Peter N. Gabrielse

ELASTIC SCATTERING OF POSITIVE PIONS, KAONS, AND PROTONS FROM 50 TO 175 GEV/C

by

Joel Nathan Butler

A.B., Harvard University

(1969)

Submitted in Partial Fulfillment

of the Requirements for the

Degree of Doctor of Philosophy

at the

Massachusetts Institute of Technology

August 11, 1975

Signature of Author.....[redacted].....

Department of Physics, August 11, 1975

Certified by.....[redacted].....

Thesis Supervisor

Accepted by.....

Chairman, Departmental Committee on

Graduate Students

ELASTIC SCATTERING OF POSITIVE PIONS, KAONS, AND PROTONS FROM 50 TO 175 GeV/c

by

Joel Nathan Butler

Submitted to the Department of Physics on August 11, 1975 in partial fulfillment of the requirements for the degree of Doctor of Philosophy.

ABSTRACT

Differential cross-sections for π^+P, K^+P, and PP elastic scattering were measured using the Single Arm Spectrometer Facility of the Fermi National Accelerator Laboratory. The incident momenta were 50, 70, 140, and 175 GeV/c. The measurements covered an interval in invariant four-momentum transfer t from -.05 to -.7 $(GeV/c)^2$. The angular distributions were smooth and were well described by quadratic exponential fits. The energy dependence was discussed from the viewpoint of Regge-pole models and the Geometric Scaling hypothesis. The shrinkage of the forward diffraction peak near $-t = .2$ GeV^2 for PP scattering persists at NAL energies but the rate of shrinkage has diminished. Predictions of the Geometric Scaling hypothesis seem to be satisfied for K^+P by 70 GeV/c and for π^+P and PP by 140 GeV/c.

THESIS SUPERVISOR: Lawrence Rosenson
TITLE: Professor of Physics

TABLE OF CONTENTS

		Page
ABSTRACT		2
TABLE OF CONTENTS		3
LIST OF FIGURES		6
LIST OF TABLES		8
I.	INTRODUCTION	9
	A. Theoretical Background	9
	B. Experimental Perspective	17
	C. History of the Experiment	17
II.	KINEMATICS	19
	A. Basic Kinematic Formulae	19
	B. Resolution Requirements	22
	1. Momentum Resolution	22
	2. Angular Resolution	24
III.	EXPERIMENTAL SETUP	28
	A. M6 Beam Line	30
	B. AVB System: Variation of the Scattering Angle	36
	C. Focusing Spectrometer	40
	D. Functional Description of Detectors	47
	1. Trigger Counters	52
	2. Particle Identification	54
	3. Trajectory Measurement	65
	4. Extraction of the Coordinates of the Scattered Particle	72
	E. Data Acquisition Hardware	86

1. Online Computer 86

2. Computer Interface 87

3. Gating System 90

4. Fast Electronics 91

F. Target System 96

IV. PERFORMANCE AND CALIBRATION OF THE APPARATUS 98

A. Determination of Spectrometer Properties 98

1. Transfer Matrix 98

2. Resolution in t and MM^2 103

3. Acceptance 103

B. Calibration of the t-scale 106

C. Alignment of the Beam and Spectrometer 107

D. Momentum Matching of Beam and Spectrometer 112

E. Absolute Momentum Calibration 113

V. DATA-TAKING 115

VI. ANALYSIS OF THE DATA 122

A. Pass I: Event-by-Event Analysis 122

B. Pass II: Conversion of Yields to Absolute Cross Sections 131

1. Computation of the Cross Section for Type 1 Yields 133

2. Calculation of the Cross Section for Type 2 Yields 139

3. Run Combination 142

VII. FINAL CORRECTIONS TO CROSS SECTIONS 145

A. Absorption and Decay Corrections 148

B. Contamination of Incident Particle Flux by Positrons and Muons 149

C. Removal of Electromagnetic Effects from the Cross Sections 152

1. Coulomb Scattering Corrections 153

2. Radiative Corrections 156

D. Double Scattering Corrections 157

E. Corrections for Inelastic Events Falling Inside Mass Cut 161

VIII. DISCUSSION OF SYSTEMATIC UNCERTAINTIES 164

A. Systematic Uncertainties in the Overall Scale 164

B. Systematic Errors in the t-scale 165

C. Systematic Errors in the "Differential" t-scale 166

D. Systematic Errors Arising from Uncertainties in Corrections 167

IX. RESULTS 169

X. PHYSICS DISCUSSION 187

BIBLIOGRAPHY 195

APPENDICES 197

ACKNOWLEDGEMENTS 220

BIOGRAPHICAL NOTE 222

LIST OF FIGURES

		Page
1.	Definition of kinematic quantities	20
2.	Missing mass resolution and separation of elastic and inelastic events	23
3.	T resolution as a function of energy and angle for .1 mr angular resolution	26
4.	Overview of the experiment	29
5.	M6 beam: first stage	33
6.	M6 beam: second stage	33
7.	M6 beam: third stage	33
8.	Particle trajectories in the M6 beam	35
9.	Geometry of the angle varying bends	39
10.	Optics of the Single Arm Spectrometer	43
11.	Particle trajectories in the spectrometer	45
12.	Source as viewed by the spectrometer	46
13.	Location of detectors	51
14.	Sketches of threshold and differential Cerenkov counter	55
15.	Disc Cerenkov counter	62
16.	Incident and scattered particle coordinate systems	67
17.	Specification of scattered particle trajectory at the back of the spectrometer	70
18.	Detector profiles in the spectrometer	73
19.	Explanation of spectrometer momentum calculation	77
20.	Structure of the first order transfer matrix	79
21.	Production coordinate distributions and distributions of kinematic quantities	85

22.	Schematic of the Camac system	89
23.	Fast electronics	94
24.	Calibration of spectrometer solid angle	102
25.	Total resolution $\sigma(MM^2)$ at t = 0.1 $(GeV/c)^2$	105
26.	Elimination of vertical alignment problems by averaging AVB+ and AVB- runs	111
27.	Setup for scattering at very small angles	119
28.	Example of a yields plane	129
29.	MM^2 cut on elastic events	132
30.	Integration region for acceptance integrals	138
31.	Effect of radiation on elastic yield	157
32.	Double scattering	160
33.	Affect of a small error in the differential t-scale	168
34.	Differential cross sections	174
35.	Comparison of A parameter from fit of Table 18 with optical theorem prediction	180
36.	S dependence of slope parameters B and C	181
37.	S dependence of logarithmic derivative b at $-t = .2\ GeV^2$	186
38.	Geometric scaling test for K^+P	192

LIST OF TABLES

Number		Page
1	Properties of the M6 beam (recombined mode-east branch)	34
2	Parameters of the AVB system	38
3	Summary of spectrometer optical properties	44
4	Geometry and location of scintillation counters	48
5	Threshold Cerenkov counter parameters	57
6	Properties of Differential Cerenkov counters	59
7	Geometry and location of MWPCs in the spectrometer	69
8	Transfer matrix elements from spectrometer horizontal image plane to target midplane	83
9	Particle composition of the M6 beam	120
10	Details of the run plan	121
11	Truth tables for particle identification	124
12	Descriptions of yields planes	128
13	Spectrometer transmission	151
14	Muon and positron contamination	151
15	Ratio of real to imaginary parts of the scattering amplitude at $t = 0.0$	155
16	Typical contributions of t-dependent corrections to differential cross sections	163
17	Differential cross sections for elastic scattering (rebinned)	178
18	Results of fits to $d\sigma/dt = A\ e^{Bt+Ct^2}$	179
19	Results of fits to $A\ e^{Bt}$	184
20	Total elastic cross sections and tests of geometric scaling hypothesis	185

CHAPTER I

INTRODUCTION

This report describes a measurement of π^+P, K^+P, and PP elastic scattering performed at the Single Arm Spectrometer Facility of the Fermi National Accelerator Laboratory. The incident momenta are 50, 70, 140 and 175 GeV/c and the range in invariant four-momentum transfer, t, is approximately

$$.05 < -t < 0.7 \quad (\text{GeV/c})^2 \quad .$$

The experimental technique was to use a focusing spectrometer to measure the momentum and the angle of the high energy forward-scattered particle emerging from the hadronic reaction. From this information, the invariant mass, MM^2, of the unobserved particles was calculated and used in the identification of elastic events. The observed angular distribution of the elastic events was then converted to the elastic cross section $d\sigma/dt$.

A. THEORETICAL BACKGROUND

The total cross section for hadronic reactions seems to be composed of two parts.[1] The first is contributed by reactions which individually approach approximately energy independent limiting cross-sections (a slow energy variation is not ruled out). This part is called "diffractive" by analogy to optics and includes elastic scattering and those inelastic processes called "single" and "double diffractive dissociation." The second part, which includes most other

inelastic processes, is contributed by a large number of reactions each of whose cross sections seems to go to zero as the energy increases. The approximate constancy at NAL energies of this part is achieved by a delicate dynamic balance in which new channels open up with energy in a way that compensates the declining contributions from channels with lower thresholds.

In a Regge picture,[2] elastic processes are mediated by the exchange of systems ('Reggeons' or 'Regge trajectories') with the quantum numbers of the neutral non-strange mesons. In this picture, as the energy increases the cross section is dominated more and more by the exchange of a single object called the Pomeron.[3] The Pomeron is the driving mechanism for high energy diffraction scattering.

Elastic scattering, which constitutes 10-20% of the total cross-section at NAL energies, reveals the properties of the Pomeron through the energy dependence of the slope parameter, B, of the forward diffraction peak, where

$$B = (d/dt \ \ell n \ d\sigma/dt)_{t = 0}$$

The dependence is usually parameterized as

$$B = B_0 + 2\alpha'(0) \ \ell n \ s/s_0$$

where $\alpha'(0)$ is the slope of the Pomeron trajectory, s is the square of the center of mass energy, and s_0 is a scale parameter, usually taken as 1 GeV^2.

The Regge approach gives the following expressions for the elastic scattering amplitudes:

$$f(K^+P) = f^K_{\underline{p}} + f^K_{f_0} - f^K_{\omega} + f^K_{A_2} - f^K_{\rho}$$

$$f(K^-P) = f^K_{\underline{p}} + f^K_{f_0} + f^K_{\omega} + f^K_{A_2} + f^K_{\rho}$$

$$f(PP) = f^P_{\underline{p}} + f^P_{f_0} - f^P_{\omega} - f^P_{A_2} - f^P_{\rho}$$

$$f(P\bar{P}) = f^P_{\underline{p}} + f^P_{f_0} + f^P_{\omega} + f^P_{A_2} + f^P_{\rho}$$

$$f(\pi^+P) = f^\pi_{\underline{p}} + f^\pi_{f_0} - f^\pi_{\rho}$$

$$f(\pi^-P) = f^\pi_{\underline{p}} + f^\pi_{f_0} + f^\pi_{\rho}$$

where f^j_K is the amplitude of the trajectory K's contribution to the elastic scattering of particle j($\pi^\pm$, $K^\pm$, P, or $\bar{P}$) on protons. The Regge trajectories which are expected to contribute are the Pomeron ($\underline{p}$), the f meson (f_0), the omega meson (ω), the A_2, and the rho (ρ). The ω and A_2 have odd G parity and cannot couple to the π-π vertex in π^+ and π^- elastic scattering. In general, the isopin 1 exchanges, A_2 and ρ, can be shown to be small at high energies so that only three trajectories, $\underline{p}$, f_0, and ω contribute to elastic scattering.

The Regge amplitudes f^j_K are of the form

$$f^j_K \alpha \beta^j_K(t)\, \beta^P_K(t)\, s^{\alpha_K(t)}\, \frac{1 + \tau\, e^{-i\pi\alpha_K(t)}}{\sin \pi\, \alpha_K(t)}$$

where τ is the signature of the trajectory ($\tau = +1$ or -1). No theoretical calculation of the $\beta(t)$ is available. Phenomenological inputs are therefore used to determine the $\beta(t)$. The trajectories, $\alpha(t)$, are usually taken as

$$\alpha_{\underline{p}}(t) = 1 + \varepsilon\, t \qquad (\varepsilon < 1/2)$$

and

$$\alpha_{f_0,\omega} = 1/2 + t\ .$$

While Regge models have been successful in describing and interrelating the s-dependences of many reactions and in explaining qualitatively many features of the angular distributions, the lack of a calculation of the $\beta(t)$ (Regge residues) has been a drawback.

Information on trajectories besides the Pomeron can be obtained by studying the difference between particle and anti-particle elastic cross sections. The $\underline{p}$ and f_0 trajectories have charge conjugation quantum number $c = +1$. The ω has $c = -1$. The particle and anti-particle amplitudes are

$$f(x^+P) = f_{\underline{p}} + f_{f_0} - f_\omega$$

$$f(x^-P) = f_{\underline{p}} + f_{f_0} + f_\omega$$

($x = K$ or P). The $c = +1$ term is nearly completely imaginary.[4] It follows that

$$d\sigma/dt\ (x^{\pm}P) \simeq \left|f_{\underline{p}} + f_{f_0}\right|^2 \mp 2\ \mathrm{Im}(f_{\underline{p}} + f_{f_0})\mathrm{Im}f_\omega$$

or

$$\mathrm{Im}f_{\omega} = \frac{d\sigma/dt(x^{-}P) - d\sigma/dt(x^{+}P)}{\{8[d\sigma/dt(x^{-}P) + d\sigma/dt(x^{+}P)]\}^{1/2}}$$

The "cross over point," where $d\sigma/dt(x^{+}P) = d\sigma/dt(x^{-}P)$, occurs at the t value where $\mathrm{Im}f_{\omega} = 0$.

Elastic scattering measurements at NAL energies are insufficient by themselves to isolate the Pomeron amplitude. The best one can do with elastic cross sections alone is to extract the contribution of all the c = +1 amplitudes. This is accomplished by studying the average, Σ, of the particle and anti-particle cross sections:

$$\Sigma \equiv 1/2\ [d\sigma/dt(x^{-}P) + d\sigma/dt(x^{+}P)]$$

This average eliminates the interference term between c = +1 exchanges and c = -1 exchanges. If f^{+} is the amplitude for c = +1 and f^{-} is the amplitude for c = -1, then

$$\Sigma = |f^{+}|^2 + |f^{-}|^2 .$$

It can be shown[4] that the c = +1 amplitudes dominate at high energy. While the Pomeron accounts for most of the f^{+} amplitude, the f_0 trajectory is expected to make a non-negligible contribution. Therefore,

$$\Sigma \simeq |f_{\underline{p}} + f_{f_0}|^2_{\text{nonflip}} .$$

The Regge models leave many questions unanswered. For example, why should the various elastic processes, which are all mediated by the same exchanges, have such different angular distributions? The slope parameter B is larger for protons than for pions or kaons.[5] As the energy increases, moreover, B increases for K^+P and PP elastic scattering but remains rather constant for $\pi^{\pm}P$ and K^-P scattering. For $\bar{P}P$ scattering B actually decreases with energy.[5]

These last observations are the point of departure for another approach, the dual absorptive model.[6] At intermediate energies, other systems besides the Pomeron contribute to elastic scattering. The t-channel exchanges of these systems can be related to the resonances in the s-channel.[7] According to the dual absorptive model of Harari,[6] the elastic cross section may be written

$$d\sigma/dt \simeq P_0^2(t) + 2\,R(t)P_0(t)$$

where $P_0^2(t)$ represents t-channel Pomeron exchange or non-resonant background in the s-channel and $R(t)$ is the contribution of the s-channel resonances or of normal Regge exchange in the t channel. Because $R(t)$ is small, an additional term - $R^2(t)$ - due solely to the resonances is negligible. The differences between the various elastic processes are the result of the different s-channel quantum numbers of the initial state. Since the K^+P and PP initial states have exotic s-channel quantum numbers, $R(t)$ vanishes and pure Pomeron behavior will occur at fairly low energies. The comparison of K^+P and K^-P or of PP and $\bar{P}P$ elastic scattering reveals the two functions $P_0(t)$ and $R(t)$. For example,

$$d\sigma/dt(K^+P) = P_0^2(t)$$

and

$$d\sigma/dt(K^-P) = P_0^2(t) + 2\,P_0(t)\,R(t)$$

so that

$$R(t) = \frac{d\sigma/dt(K^-P) - d\sigma/dt(K^+P)}{2\sqrt{d\sigma/dt(K^+P)}}$$

$P_0(t)$ and $R(t)$ have been obtained from data at 5 GeV/c[8] and indicate that the Pomeron amplitude gets contributions from all partial waves

$$\ell < r\sqrt{-t}$$

where r is a parameter describing the range of the interaction. The non-Pomeron contribution is dominated by the most peripheral partial waves:

$$\ell \sim r\sqrt{-t}$$

Since the appearance of a pronounced dip in the pp elastic cross section at $-t \sim 1.3$ GeV^2 at ISR energies,[9] optical models for elastic scattering have become popular.[10] This is not surprising since the approximations on which these models are based become more valid at high energies. Within this framework, elastic scattering measurements are viewed as determining properties such as the mean radius and the opacity of the incident particle. In this approach, the scattering amplitude, usually approximated as the square root of the differential cross-section,[11] is transformed into impact parameter

space. The scattering amplitude a(s,b) in impact parameter space is

$$a(s,b) = \frac{1}{\hbar c\sqrt{\pi}} \int_0^{t_{max}} \sqrt{d\sigma/dt}\; J_0\,(b\sqrt{-t})\;\sqrt{-t}\; d(\sqrt{-t})$$

where $J_0(x)$ is the cylindrical Bessel function of order zero (a derivation of this form and an explanation of the normalization of a(s,b) is given in Appendix 2). Theoretical effort centers on constructing a model which produces an amplitude a(s,b) that agrees with the data.

It should be added that elastic scattering is directly related to inclusive inelastic scattering by s-channel unitarity. One can, therefore, extract from elastic cross sections the spatial properties of inelastic scattering. This is interesting because the total cross section for PP reactions has been observed to rise at ISR energies[12] but the origin of this rise is still an open question.[13]

In conclusion, elastic scattering is an important area of investigation for the following reasons:

i) the simplicity of the final state makes it possible to do precise measurements.

ii) the theoretical problem also benefits from the two body final state so that several approaches or models have emerged which explain, at least qualitatively, the main features of the data.

iii) the mechanisms which are responsible for elastic scattering are presumably at work in other reactions--e.g. diffractive dissociation. In addition, s-channel unitarity relates elastic scattering to the totality of inelastic reactions.

From the discussion above, it is evident that many insights can be gained by the comparison of different elastic reactions. These comparisons are less reliable if they must use measurements done on different apparatus at different times. We have measured not only K^+, P, and π^+ elastic scattering, the subject of this report, but also K^-, $\overline{P}$, and π^- elastic scattering with the same apparatus.

B. EXPERIMENTAL PERSPECTIVE

Elastic hadron scattering has been studied intensively at Brookhaven, Argonne, Cern, and Serpukhov.[14] At ISR, proton-proton elastic scattering measurements have been done at $s \sim 3000$ $(GeV/c)^2$. These experiments have revealed a dip in the vicinity of $-t = 1.3$ GeV^2 and have strengthened the case for a break (rapid change of slope) in the differential cross section at $-t \simeq .12$ GeV^2.[15] At NAL, the slope of the very forward ($-t < .1$) proton diffraction peak has been measured from 8 to 400 GeV/c incident momentum.[16]

Our experiment has extended the data on $\pi^\pm$, $K^\pm$, and $\overline{P}$ elastic scattering to 175 GeV/c. We have filled in the gap in the pp coverage between Serpukhov and ISR.

The fact that all six elastic processes have been studied with the same apparatus at several energies will reduce to a very low level the relative systematic errors and provide a detailed picture of elastic scattering at NAL energies.

C. HISTORY OF THE EXPERIMENT

These measurements constitute part of the initial physics program of the Single Arm Spectrometer. They were performed in 1974 and early 1975 by a collaboration of physicists who, together with the Fermilab staff, designed and constructed the spectrometer. The members

of the Single Arm Spectrometer Group are listed below.*

The initial experimental program was called Experiment 96. The following reactions were studied at incident momenta of 50, 70, 100, 140, and 175 GeV/c:

i) Elastic K^+P, π^+P, PP, K^-P, π^-P and $\bar{P}P$ scattering between $-t$ and .05 and 0.8 (approximate) $(GeV/c)^2$.

ii) Single particle inclusive scattering of K^+, π^+, P, K^-, π^-, and $\bar{P}$ on protons over the same t interval and an interval in $x \simeq 1-MM^2/s$ (where MM^2 is the missing mass squared of the unobserved particles):

$$0.75 < x < 1$$

iii) The interactions of all six particles on deuterium targets at 50 and 140 GeV/c.

---

*Argonne National Laboratory: D. S. Ayres, R. Diebold, and G. J. Maclay.

Brown University: D. Cutts, R. E. Lanou, L. J. Levinson, and J. T. Massimo.

Cern: J. Litt and R. Meunier.

Cornell University: B. Gittelman, E. Loh, and M. Sogard.

Instituto de Fisica, INFN, Bari, Italy: L. Guerriero, P. Lavopa, G. Maggi, C. DeMarzo, F. Posa, G. Selvaggi, P. Spinelli, F. Waldner, and E. N. Anelli.

Massachusetts Institute of Technology: D. Barton, J. Butler, J. E. Elias, J. Fines, J. Friedman, H. Kendall, B. Nelson, L. Rosenson, and R. Verdier.

National Accelerator Laboratory: A. E. Brenner and G. Mickenberg.

Northeastern University: B. Gottschalk.

Stanford Linear Accelerator: R. L. Anderson, D. Gustavson, K. Rich, D. M. Ritson, and G. A. Weitsch.

CHAPTER II

KINEMATICS

A. BASIC KINEMATIC FORMULAE

In the single arm technique, the properties of only one particle are measured. From these measurements one can calculate the invariant mass of the remaining final state particles and use this quantity to identify elastic scatters. In this experiment, detailed measurements are made on the forward (high energy) scattered particle.

The relativistic statement of energy-momentum conservation is:

$$P_1 + P_2 = P_3 + P_4$$

(P_i is the four-momentum of the i^{th} particle. See Figure 1 for definitions.) The invariant mass of the unmeasured final state system ('4') is given by

$$-MM_4^2 = P_4^2 = (P_1-P_3+P_2)^2 = (P_1-P_3)^2 + 2P_2(P_1-P_3) + P_2^2$$

Since $P_2 = (0, iM_p)$ for the stationary target proton, this expression reduces to

$$MM_4^2 = t + M_p^2 + 2M_p(E_1-E_3) \qquad (1)$$

Figure 1 : DEFINITION OF KINEMATIC QUANTITIES

(a) Collision in arbitrary frame of reference

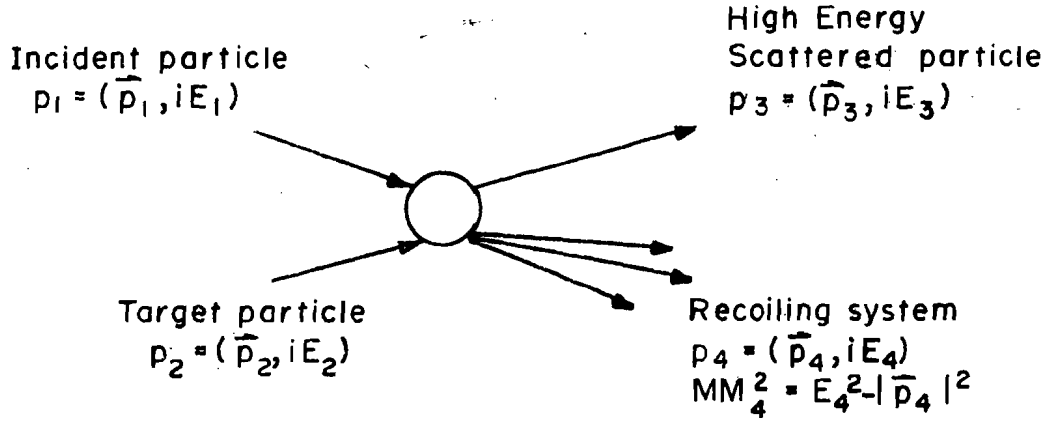

(b) Collision in the Laboratory frame (rest frame of target proton)

M_p = proton rest mass

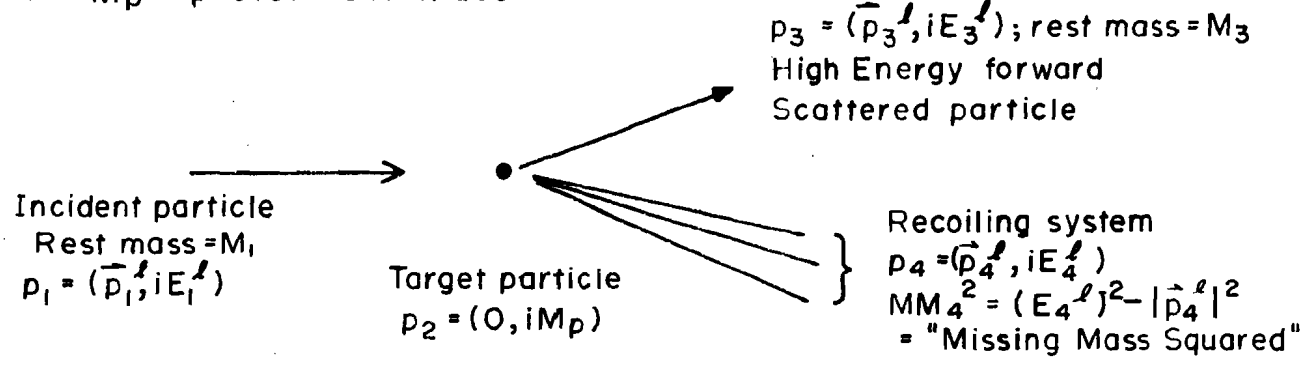

The quantity $t \equiv -(P_1-P_3)^2$ is the invariant four-momentum transfer. This quantity may be expressed in terms of the laboratory coordinates defined in Figure 1b:

$$t = (M_1^2 + M_3^2 + 2|\vec{P}_1^{\,\ell}|\ |\vec{P}_3^{\,\ell}|\cos\theta_\ell - 2\ E_1^{\ell}E_3^{\ell}) \qquad (2)$$

For the very high energies in this experiment, E_1^{ℓ} and E_3^{ℓ} can be approximated as follows:

$$E_1^{\ell} = \sqrt{|\vec{P}_1^{\,\ell}|^2 + M_1^2} = |\vec{P}_1^{\,\ell}|\sqrt{1 + M_1^2/|\vec{P}_1^{\,\ell}|^2}$$

$$\simeq |\vec{P}_1^{\,\ell}| + M_1^2/2|\vec{P}_1^{\,\ell}|$$

and

$$E_3^{\ell} = \sqrt{|\vec{P}_3^{\,\ell}|^2 + M_3^2} \simeq |\vec{P}_3^{\,\ell}| + M_3^2/2|\vec{P}_3^{\,\ell}|.$$

Then

$$t = 2|\vec{P}_1^{\,\ell}|\ |\vec{P}_3^{\,\ell}|(\cos\theta_\ell - 1) + M_1^2\left(1 - \frac{|\vec{P}_3^{\,\ell}|}{|\vec{P}_1^{\,\ell}|}\right) + M_3^2\left(1 - \frac{|\vec{P}_1^{\,\ell}|}{|\vec{P}_3^{\,\ell}|}\right)$$

$$- \frac{M_1^2\, M_3^2}{2|\vec{P}_1^{\,\ell}|\ |\vec{P}_3^{\,\ell}|} \qquad (2a)$$

Since the t range under consideration includes angles which are never greater than 20 milliradians (mr), $\cos\theta_\ell \simeq 1 - 1/2\ \theta_\ell^2$. In addition, for elastic scattering $(1 - |\vec{P}_3^{\,\ell}|/|\vec{P}_1^{\,\ell}|)$ and $(1 - |\vec{P}_1^{\,\ell}|/|\vec{P}_3^{\,\ell}|)$ are less than .005 everywhere so that

$$t \simeq -|\vec{P}_1^{\,\ell}|\,|\vec{P}_3^{\,\ell}|\theta_\ell^2 + t_{min} \qquad (2b)$$

where t_{min} is the sum of the last three terms of Eq. (2a) and is negligible.

(From here on, all angles and momenta will be in the laboratory frame unless otherwise stated. The superscript ℓ and the absolute value symbol will be omitted if the context makes it obvious that they were intended.)

B. RESOLUTION REQUIREMENTS FOR ELASTIC PHYSICS

1. Momentum resolution

The single particle spectrum in missing mass squared begins with a sharp spike at .88 GeV^2/c^4 corresponding to the mass squared of the target proton recoiling from an elastic scatter. Then there is nothing up to the kinematic threshold for inelastic scattering (see Fig. 2a). This threshold corresponds to the production of an additional pion at rest with respect to the recoiling target proton. The invariant mass of this system is given by

$$MM^2 = (M_p + M_\pi)^2 = t + M_p^2 + 2M_p(E_1-E_3) \qquad (3a)$$

where M is the mass of the pion. Neglecting the dependence on t, we have

$$E_1-E_2 \simeq P_1-P_3 = \Delta P = M_\pi\ (1 + M_\pi/2M_p) \qquad (3b)$$

Thus, the energy separation between the elastic peak and inelastic threshold is 1.07 x M_π or $\sim$ 150 meV.

The experimentally observed elastic peak is broadened by the momentum resolution of the spectrometer (see Fig. 2b). The momentum

Figure 2 : Missing Mass Resolution and Separation of Elastic and Inelastic Events

(a) MM^2 spectrum perfect resolution

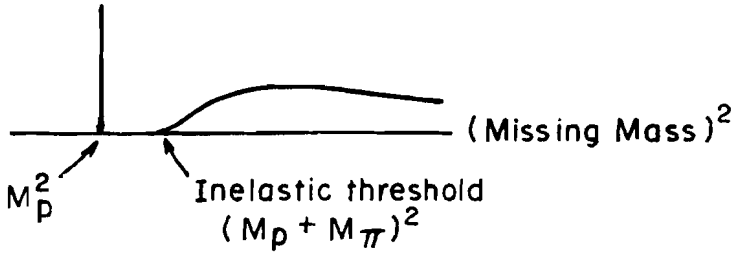

(b) MM^2 spectrum smeared by experimental resolution. The resolution shown is sufficiently good so that nearly all the elastic events fall to the left of the cut and very few inelastic events are to be left of the cut.

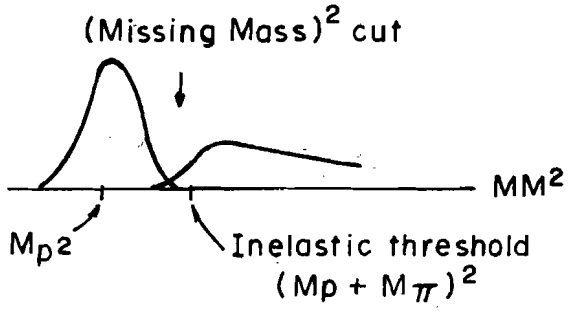

(c) Bad resolution situation

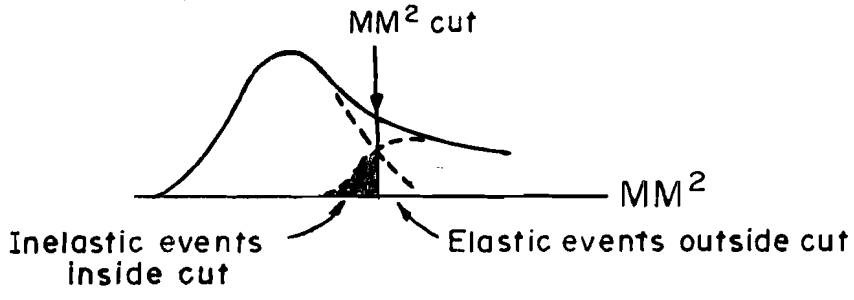

resolution to just barely distinguish elastic scatters from inelastic events on the basis of MM^2 is $\sigma_{\Delta p} \sim 1.07\ M_\pi$ so that the percent momentum resolution required is

$$\sigma\ (\Delta p/p) \simeq 1.07\ M_\pi/p \qquad (4)$$

In practice, one hopes to do at least a factor of two or three better than this. At high energies, this is a demanding requirement. For example, at 140 GeV/c, this implies a momentum resolution of .05% to .03%.

The missing mass squared resolution actually achieved will determine how clean the identification of elastic events is. For example, if the peak is completely separated from the background of inelastic events, it is easy to apply a cut on MM^2 which includes essentially all the elastic events and rejects all the inelastic ones. If this is not the case, some inelastic events may fall inside the cut and some elastic events may fall outside it. Thus, two corrections are required. It is clear that one of these corrections can be reduced at the cost of enlarging the other. This less-than-optimal situation is illustrated in Figure 2c.

2. t and angular resolution

The t resolution is dominated by the angular resolution, given that the stringent momentum resolution requirements described in the previous section are satisfied. The t resolution is related to the angular resolution by

$$\Delta t = 2\ |\vec{P}_1^{\,\ell}|\ |\vec{P}_2^{\,\ell}|\ \theta_\ell\ \Delta\theta_\ell = 2t\ \frac{\Delta\theta_\ell}{\theta_\ell} \qquad (5)$$

Since the spectrometer has a fixed angular resolution, σ_θ, at a given energy, the t resolution gets poorer as the scattering angle or the incident momentum gets larger.

The requirements on the t resolution are qualitatively different from those on the momentum resolution. Good momentum resolution is essential for the identification of elastic events. The t-resolution limits the kinds of structures that can be observed in the angular distributions. Since the angular distributions are rather smooth at high energies (indeed that is one of the reasons for going to high energies), the t resolution is not very critical. We have aimed at angular resolutions of $\sim$ .1 mr. Figure 3 shows the corresponding t resolutions at different energies and in different angular ranges.

According to equation 1, MM^2 depends also on t and so far we have failed to include the t resolution in the MM^2 resolution. It is clear from Figure 3 that this is hardly necessary. The missing mass squared resolution is much less sensitive to the angular resolution than to the momentum resolution.

It should be noted that, at fixed angle, the momentum spectrum P_1-P_3 looks very much like the MM^2 spectrum. The only difference is that the elastic events always fall around M_p^2 in missing mass squared whereas the P_1-P_3 distribution centers around $|t|/2M_p$ and therefore changes its position with the scattering angle. From equation 1, we have E_1-E_3 = $|t|/2M_p$. Energy conservation then gives T = $|t|/2M_p$ where T is the kinetic energy of the proton recoiling from the elastic scatter. Then for elastic scattering

$$-t = (P_1{}^{\ell}\theta_{\ell})^2/(1 + P_i{}^{\ell}\theta_{\ell}{}^2/(2M_p)) \qquad (6)$$

Figure 3: t Resolution (σ_t) as a Function of t, Angle, and Momentum

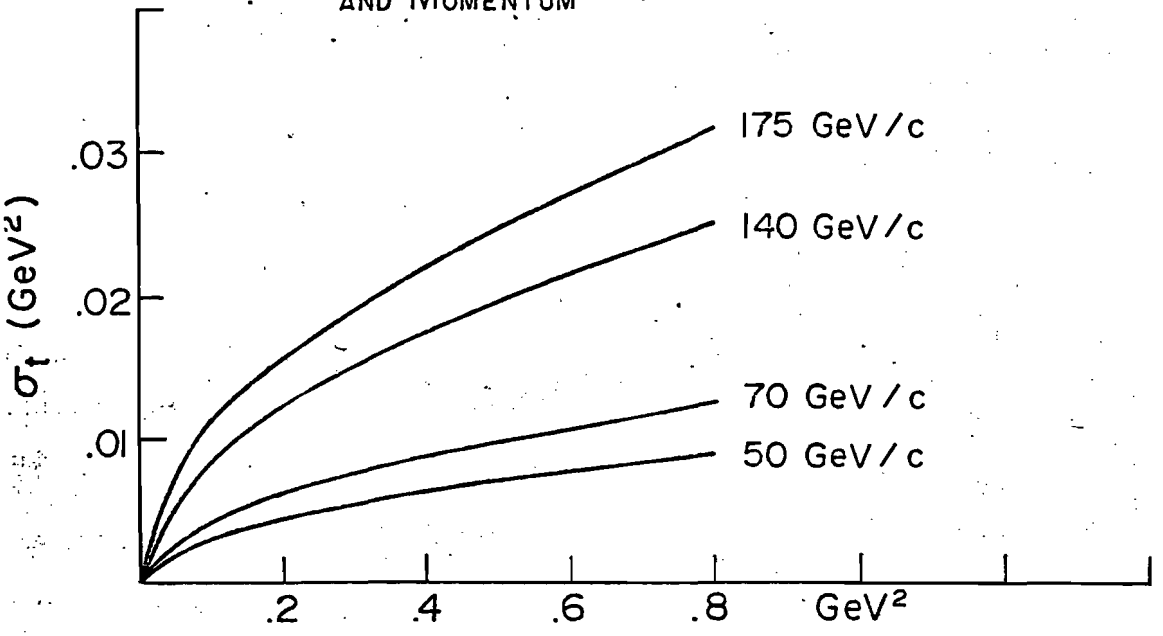

(a) σ_t vs t at 50, 70, 140, and 175 GeV/c

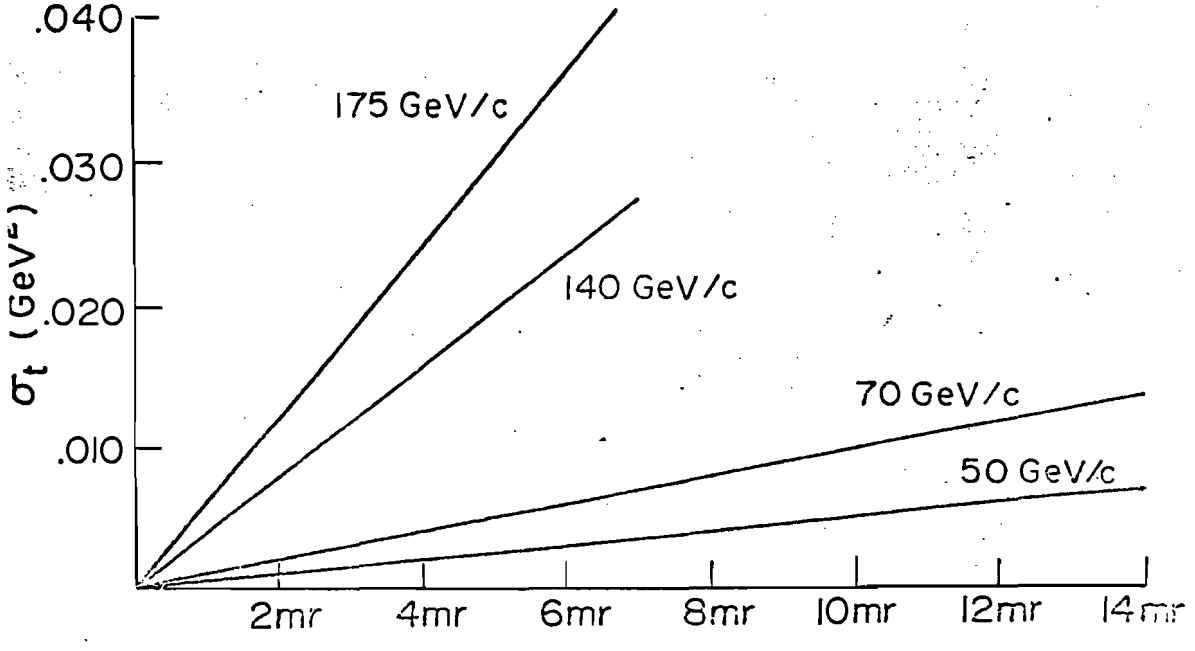

(b) σ_t vs θ at 50, 70, 140, and 175 GeV/c

3. "Transfer Coordinates" and the necessity for measurements on the incident particle

The MM^2 resolution depends chiefly on the quantity $E_1-E_3 \simeq P_1-P_3$, which will be referred to as the "transfer momentum," P_T. Since the beam typically accepts a 1% band, in momentum, it is necessary to measure the momentum of the incident particle as well as the scattered particle. A hodoscope in the beam line accomplishes this. Both the beam line momentum resolution and the spectrometer momentum resolution contribute to the final MM^2 resolution.

In experiments at lower energies, the beam divergence was frequently negligible compared to the scattering angles. At NAL energies, in this t range, the scattering angles are as small as 1-1/2 mr. The beam divergence of .2 to .3 mr at our hydrogen target is not negligible relative to these scattering angles. The angle of the incident particle at the target is measured by hodoscopes. The scattering angle of an event is the vector difference between the angle of the incident particle and the angle of the scattered particle. We refer to the true scattering angle as the "transfer angle." The angular resolution depends on the precision of angle measurements in both the beam and spectrometer.

CHAPTER III

EXPERIMENTAL SETUP

OVERVIEW OF THE APPARATUS

The proton beam is extracted from the accelerator and focused by a beam transport system onto the Meson Lab production target. See Figure 4. Charged secondaries - mainly pions, kaons, and nucleons - scatter into the M6 beam line. This 1460' beam line is instrumented with scintillation counter hodoscopes to measure the momentum and trajectory of the particles and Cerenkov counters to identify the particle type. Finally, the particles are focused onto a 50 cm long liquid hydrogen target located at the rear of the Meson Detector Building. Charged particles from interactions in the hydrogen target scatter into the 500' long focusing spectrometer where their production angles and momenta are measured by multi-wire proportional chambers and they are identified as to particle type by a system of Cerenkov counters.

The central scattering angle of the spectrometer with respect to the beam is adjusted by steering the beam in the vertical plane onto the hydrogen target. The spectrometer does not move at all. The system of three dipole magnets which accomplishes this steering is called the Angle Varying Bend system or "AVB", for short.

The next three sections describe the properties of the M6 beam, the AVB system, and the focusing spectrometer. Then follow three sections describing the experimental hardware. The first describes the

Figure 4. OVERVIEW OF THE EXPERIMENT

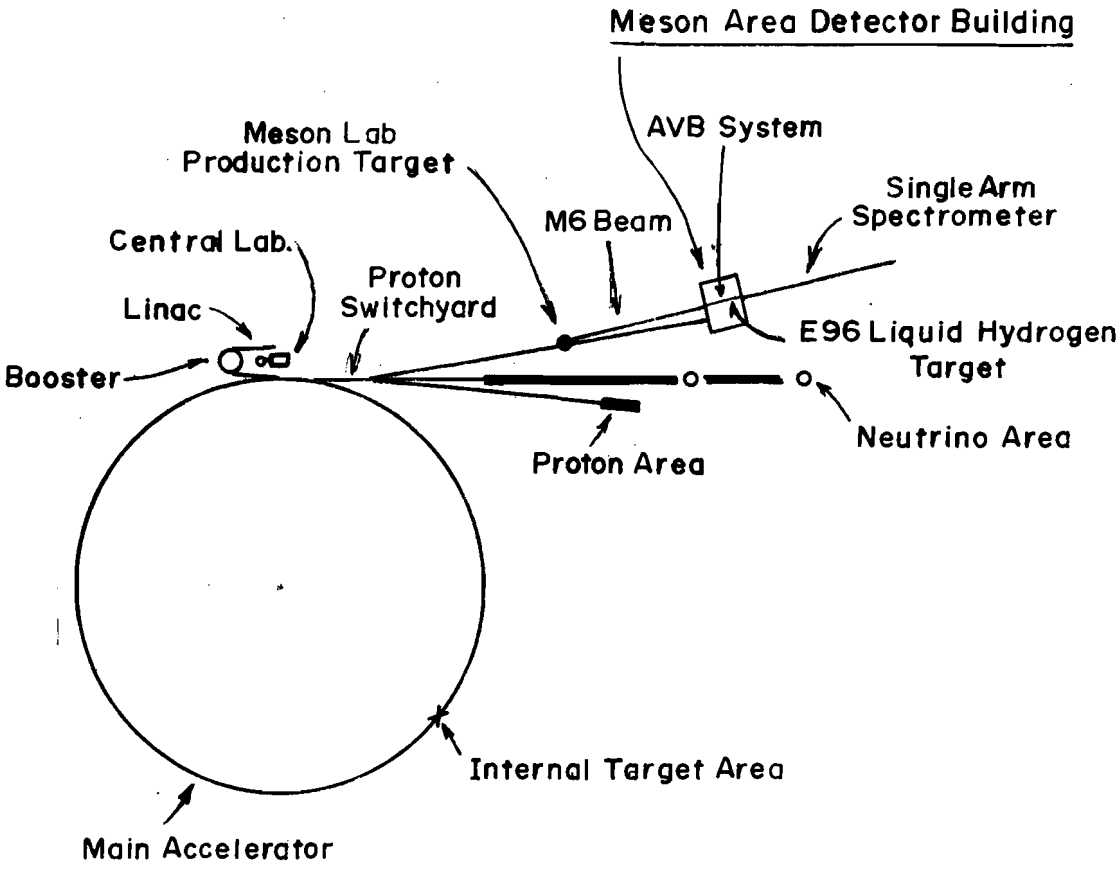

detectors in the beam and spectrometer; the second briefly discusses the data acquisition system; and the third provides information about the hydrogen target system.

A. M6 BEAM LINE

The M6 Beam Line is an unseparated charged particle secondary beam which views the Meson Lab production target at 2.7 mr. At full power, it can transport 200 GeV/c particles to targets located in the Meson Detector Building.

During this experiment, the production target was a .06" x .06" x 8" beryllium wire. Typically, 2×10^{12} 300 GeV/c protons were targeted at six second intervals. The spill length was usually about 800 milliseconds, with a duty factor varying from 30% to 70%.

The beam line consisted of three separate stages which performed the following functions:

Stage i - 'collection stage': This stage captures charged secondaries and disperses them in the horizontal plane according to momentum. At the end of this stage, the particles are focused onto a steel collimator which sets the momentum acceptance of the beam.

Stage ii - 'cleanup stage': The beam is refocused onto a hodoscope at the end of this stage. The hodoscope measures the momentum of the beam particle. The long path between the momentum collimator and the momentum hodoscope, together with the sweeping effect of the dipole magnet in this stage, produces a very clean beam with little halo in the vicinity of the hodoscope.

Stage iii - 'recombination stage': The beam is recombined in momentum and refocused to the position of the liquid hydrogen target.

Each stage consists of quadrupoles and dipole magnets. The quadrupole optics is essentially the same in all three stages. Two sets of quadrupole doublets produce point-to-parallel-to-point optics. The dipoles are located between the two doublets and bend the beam in the horizontal plane.

The components of the first stage are shown in Figure 5. Simple ray diagrams illustrate typical particle trajectories. The two septum dipole magnets capture secondaries from the production target. The central angle of the beam - 2.7 mr - is set by these septa. The collimators C2a and C2b just after the septa set the angular acceptance of the beam. The maximum acceptance is 1.7 μster. The quadrupole doublet formed by Q1 and Q2 takes a point source at the target into a parallel beam. Main ring dipoles then disperse the beam according to momentum. The second set of quads, Q3 and Q4, refocus the beam at the position labelled the "first focus." The momentum dispersion at this focus is 6.6 cm/%. (% always refers to the percent deviation of the momentum from the central momentum setting.) The collimator C3 sets the momentum bite of the beam. The maximum acceptance is 1.5%. The vertical collimator C4 sets the vertical height of the production target that the beam accepts and is generally used only to eliminate beam halo.

The second stage is shown schematically in Figure 6. It has only one bend magnet, which slightly recombines the beam. The quadrupole optics is again point-to-parallel-to-point. The momentum dispersion at the 'second focus' where the momentum hodoscope is located is 4.44 cm/%.

The third stage is represented in Figure 7. The bend magnets recombine the beam. From the exit of the bend magnets to the hydrogen

target located at the 'third focus', the beam is achromatic. The parallel region in the third stage, formed by Q11-Q12 and Q13, has suitably small angular divergence for the operation of the differential Cerenkov counters used in particle identification. The quadrupoles Q14 through Q17 form the final focus at the hydrogen target.

The magnetic optics is described to first order in Figure 8 and the most important properties are summarized in Table 1.

A system of 13 trim (vernier) magnets is provided for making minor adjustments to the beam steering. These are used to correct the steering of the beam caused by small misalignments of the quadrupoles. The trims in the second and third stage permit one to accurately center the beam on the beam line hodoscopes and on the hydrogen target.

The two quadrupoles Q5 and Q10 are "field lenses." At the first and second foci, the beam is diverging and broad horizontally because of the momentum dispersion. Q5 and Q10 provide focusing strength in the horizontal plane to help contain the beam.

Diagnostic information about the beam is provided by the beam hodoscopes and by multi-wire proportional chambers located at the second and third foci .

The fields in the magnets are set and monitored by the Meson Lab Mac computer. Information on the targeting of the primary beam is supplied through the Meson Lab Control System.

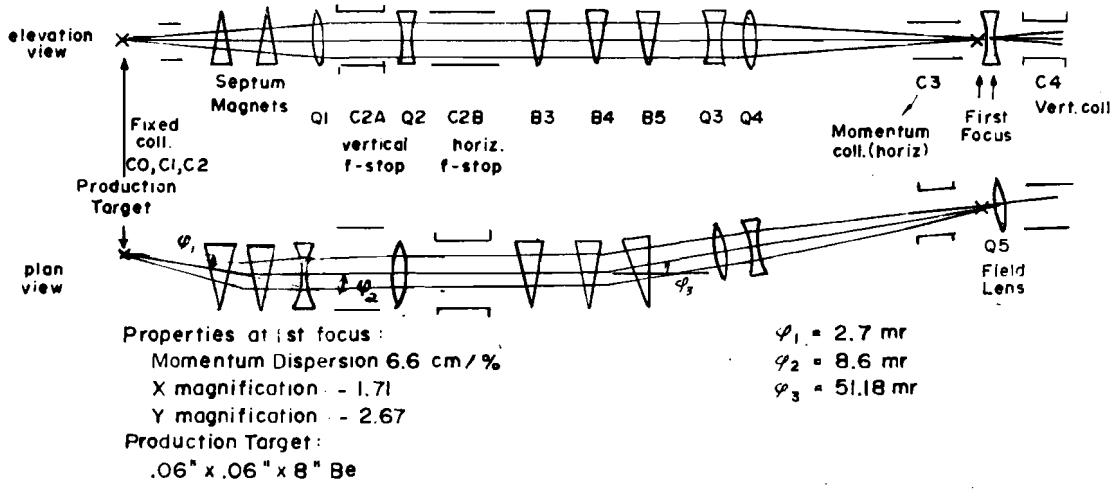

Figure 5. M6 Beam : 1st Stage

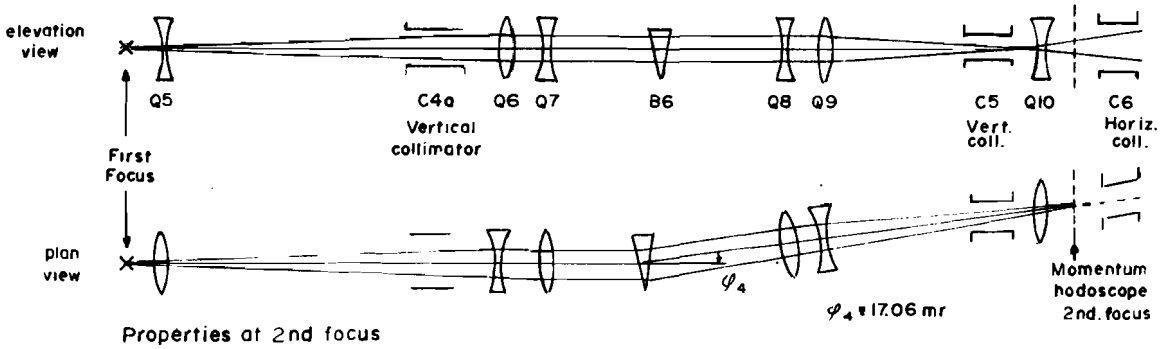

Figure 6. M6 Beam : 2nd Stage

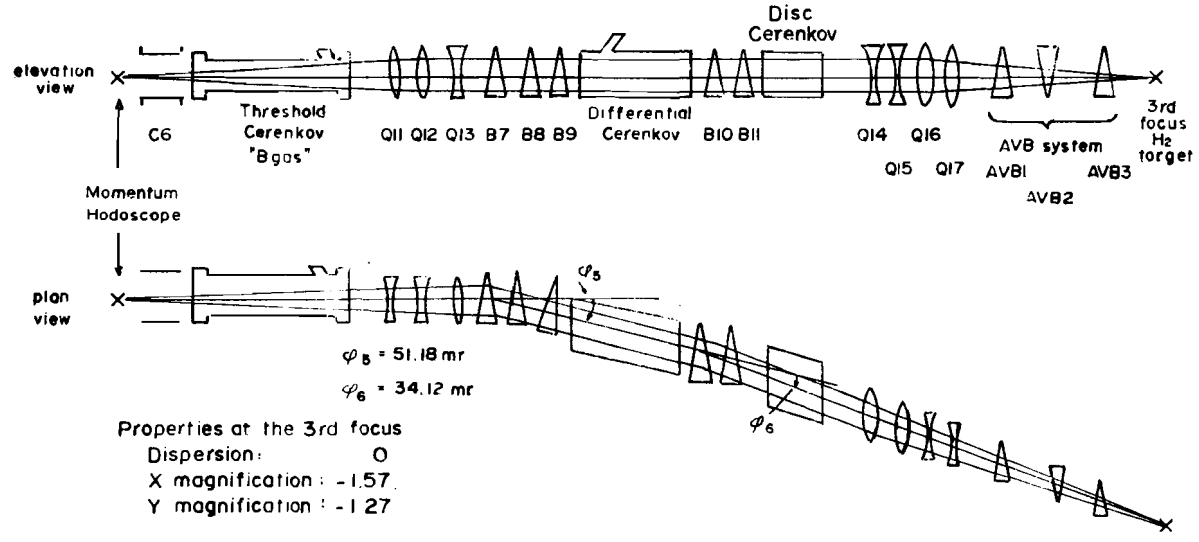

Figure 7. M6 Beam - 3rd Stage

TABLE 1

Properties of the M6 Beam
(Recombined mode-east branch)

Production Angle:	2.7 mr
Angle with respect to primary proton beam:	θ_v = 2.7 mr $\theta_h \sim 0$
Maximum momentum:	200 GeV/c
Maximum momentum bite:	1.3%
Solid Angle:	$\Delta\theta_h = \pm .56$
	$\Delta\theta_v = \pm .76$
Total =	1.7 μster
Momentum Dispersion at momentum collimator:	6.6 cm/%
Momentum Dispersion at momentum hodoscope:	4.4 cm/%
Momentum Dispersion at hydrogen target:	0
Observed Properties at hydrogen target:*	
horizontal FWHM:	∿ 8 mm
horizontal angular divergence:	∿ .1 mr (σ)
vertical FWHM:	∿ 4 mm
vertical angular divergence:	.2-.3 mr (σ)
Angular divergence in parallel region of third stage	∿.1 mr

*These beam properties are energy-dependent due to multiple scattering. They also depend on collimator settings. The numbers given were typical for the beam during data taking.

Figure 8. PARTICLE TRAJECTORIES IN THE M6 BEAM

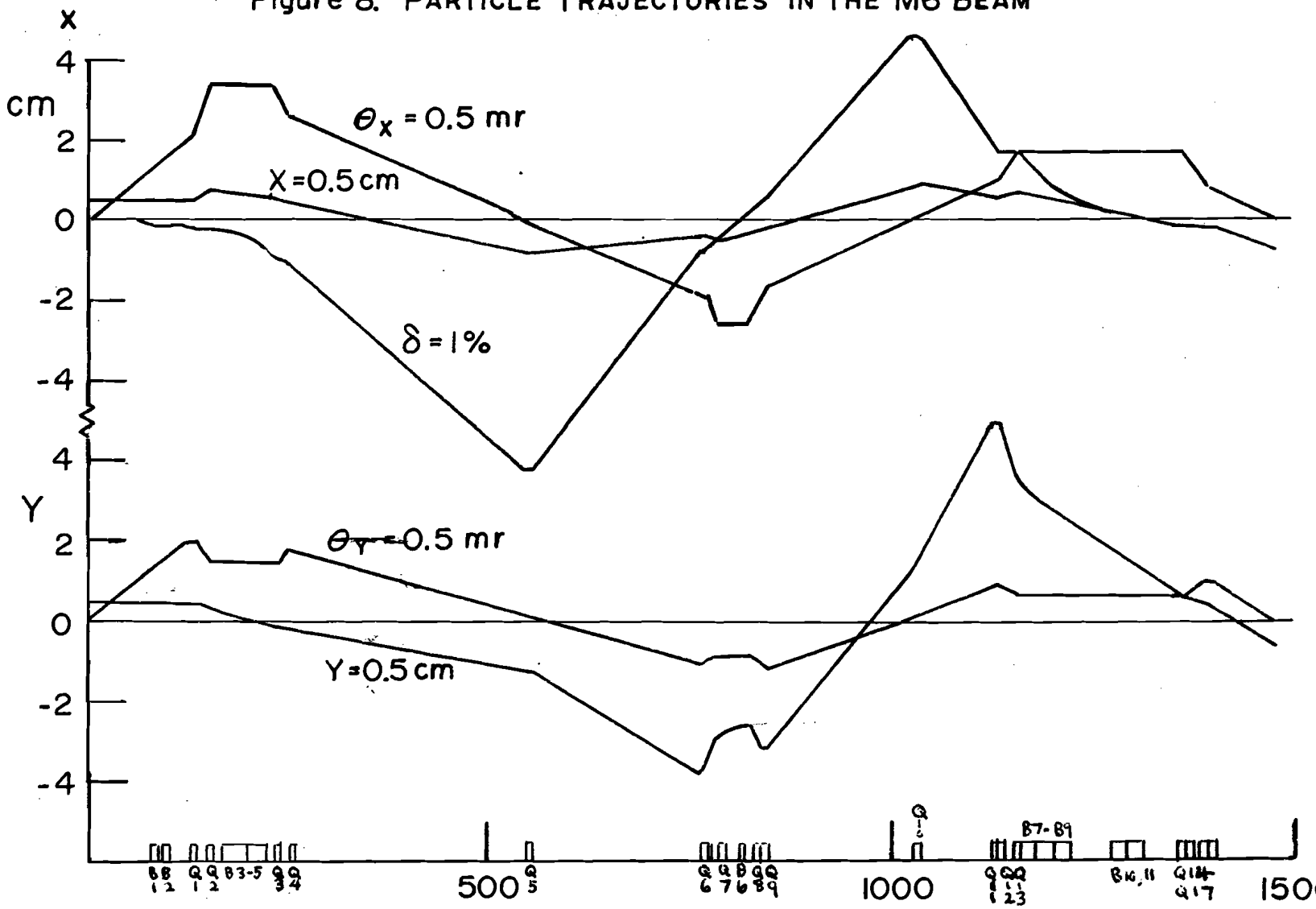

B. AVB SYSTEM - VARIATION OF THE SCATTERING ANGLE

The scattering angle is changed by steering the beam in the vertical plane onto the liquid hydrogen target. The steering system consists of three main ring dipole magnets. Its position upstream of the target and the central trajectory of the beam through it are shown in Figure 9. The first magnet bends the beam through an angle ϕ_0. The second magnet bends it with the opposite curvature through 2 ϕ_0. The last magnet bends the beam through a final angle ϕ_0. The net scattering angle, ϕ, produced by this means is 2 ϕ_0. The spacing of the magnets is arranged so that whatever the angle setting, the beam always crosses the midplane of the hydrogen target at the same point.

It should be noted that setting a certain current in the AVB implies a certain $\int B d\ell$, where B is the magnetic field. This implies a certain $P_b\ \phi$ where P_b is the central momentum setting of the beam. The quantity $P_b\phi$ is very nearly $\sqrt{-t}$ of the elastically scattered particle: $-t \simeq P_b{}^2\phi^2/(1 + P_b\phi^2/2\ m_p)$. It is more accurate to say that the AVB sets the central t setting of the spectrometer rather than the scattering angle. This makes our t scale insensitive to small uncertainties in the beam momentum.

The three AVB magnets are powered in series with a fourth 'monitor' or 'dummy' magnet. The dummy magnet is a three-foot dipole magnet located outside the beam line. A precision magnetic field probe inserted into its field is used to set and monitor the field in the three AVB dipoles. The magnetic fields of the AVB dipoles have been precisely mapped with NMR probes so that their $\int B d\ell$'s are known to $\sim$ .1%. Each magnet has also been calibrated against the dummy magnet.

The main ring dipoles have a vertical aperture of only $\pm$ 1". Since the height of the beam and its angle relative to the undeflected beam change as it passes through the AVB system, it is necessary to move the magnets to follow the trajectory if scattering angles of more than a few milliradians are to be reached. The first magnet AVB1 remains fixed. AVB2 is raised or lowered parallel to the undeflected trajectory to follow the beam. AVB3 is both raised and tilted. The parameters describing these motions are presented in Table 2, along with other parameters of the AVB system.

The hydrogen target is also tilted so that it stays parallel to the beam. This guarantees that the effective target length as seen from the spectrometer does not change as the scattering angle is varied. Two hodoscopes, BX and BY, and the trigger counter BT2 (all described below) are located between AVB2 and AVB3. They are also moved remotely to follow the vertical motions of the beam. The veto counter BTØ is attached to the target assembly and tilts with the target.

The beam can be steered onto the hydrogen target from above as shown in Figure 9a or from below as shown in Figure 9b. In this experiment, data was taken in both configurations. The combination of this data makes the experiment insensitive to small misalignments of the beam with respect to the spectrometer. This will be discussed extensively later.

The maximum excitation of the AVB dipoles corresponds to a $P_b\phi \sim 3\text{-}1/2$ GeV/c. The jacking system which moves the magnets limits the scattering angle to 100 mr if the beam is steered onto the target from above and 25 mr if the beam is steered onto the target from below.

TABLE 2

Parameters of the AVB System
(ϕ = scattering angle in milliradians)

Height of AVB2	154.53 mils x ϕ
Height of AVB3 (upstream end)	121.63 mils x ϕ
Height of BX, BY hodoscopes	127 mils x ϕ
Angle of AVB3 relative to 0°	.7488 x ϕ
Beam angle at BX, BY hodoscopes	.4975 x ϕ
Power Limit: $p\phi \propto \int Bd\ell \propto$ current	3-1/2 GeV/c
Mechanical Limit (due to maximum excursion of jacking system): maximum angle down onto target (Fig. 9a)	100 mr
Maximum angle up, onto target (Fig. 9b)	25 mr
Steering of beam spot at target:	$\sim$15 mils at ϕ = 20 mr

Figure 9 : GEOMETRY OF THE ANGLE VARYING BENDS

(a) Beam steered down onto target (elevation view)

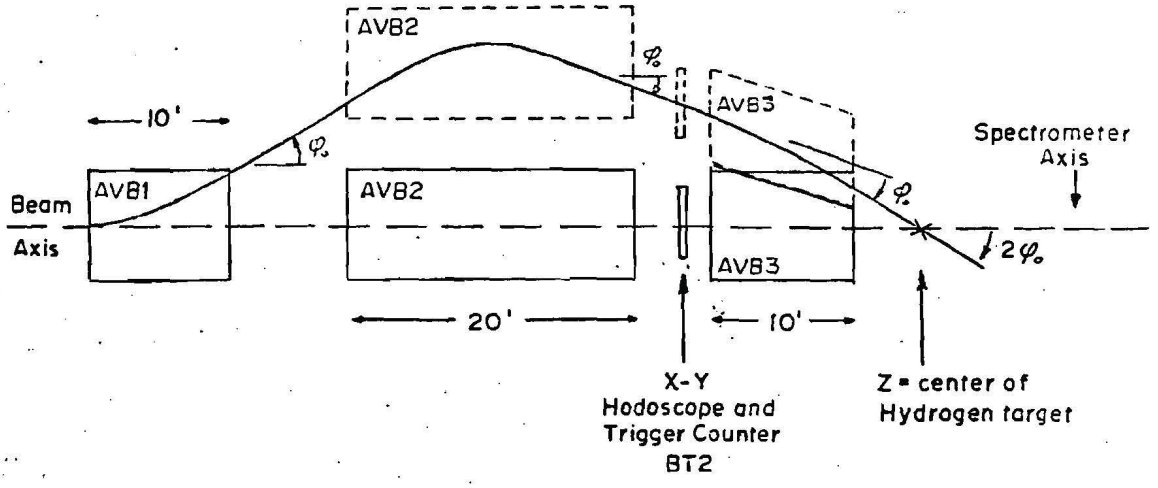

(b) Beam steered upward onto target

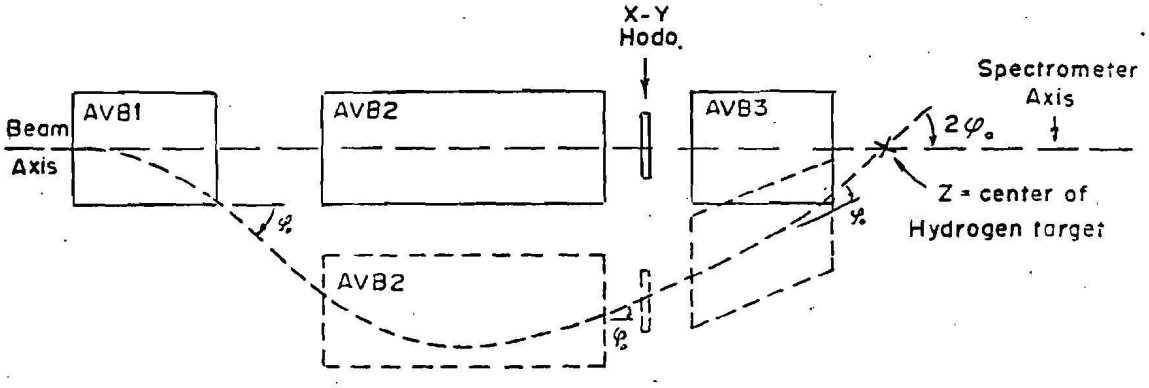

C. FOCUSING SPECTROMETER

The focusing spectrometer accepts particles scattered from the liquid hydrogen target and measures their momenta and angles. The spectrometer consists essentially of two quadrupole triplet* lenses (see Figure 10) followed by four 20' main ring dipole magnets. The first quadrupole triplet takes a point source at the target mid-plane into a parallel beam. The 60' long parallel region is suitable for the operation of a differential Cerenkov counter. A small 10' dipole magnet - the 'prebend' - is placed near the beginning of this region to sweep off-momentum particles out of the angular acceptance of the Cerenkov counter. There is a focal plane for horizontal angles at a distance of 107.27' from the target mid-plane and a focal plane for vertical angles at 88.06' from the target. At these locations, the initial angles are mapped into lateral positions. Detectors near these focal planes measure the scattering angle and allow one to establish angular acceptance cuts conveniently. The second triplet lens produces a vertical focus (image) at 269.3' and a horizontal focus (image) at 377.725'. Multi-wire proportional chambers at the vertical focus serve as profile monitors to insure that the particles are not scraping the bend magnets. This is important because of the small vertical aperture - $\pm$ 1" - of the bend magnets. The momentum analysis is performed by the four 20' main ring dipole magnets with a little help from the pre-bend. The bending is in the horizontal plane. The total bend angle of the central axis is 4.4 degrees.

---

*These are "logical triplets." The first lens consists of five quadrupoles and the second lens of six quadrupoles.

The arrangement of magnets is shown in Figure 10. Some sample rays are traced through the system to illustrate the optics.

The optics parameters of the spectrometer are presented in Table 3. These parameters are design values obtained from the computer program TRANSPORT.[17] The agreement between the design values and the actual spectrometer properties is, in general, quite good. The steps used to establish this agreement are discussed below (Section IV).

Figure 11 follows two sample rays in each plane through the system element - by - element. These 'principle rays' provide sufficient information to trace an on-momentum ray through the system. In addition, Figure 11 shows the momentum dispersion at various points along the spectrometer. These values are once again design values based on a first order treatment of the optics by TRANSPORT.

The design considerations for the spectrometer were:

i) momentum resolution sufficient to separate elastic events from inelastic ones (see Section IIB).

ii) good angular resolution ($\sim$ .1 mr).

iii) large and reasonably uniform acceptance in momentum and angle.

The object (source) which the spectrometer looks at is the region of the liquid hydrogen target that is illuminated by the beam. In the horizontal plane, the spectrometer axis is at 0° to both the beam and the target axes. The horizontal extent of the object is then just the horizontal width of the incident beam. In the vertical plane, the object size depends on the vertical beam size, the target length, and the AVB angle. This is illustrated in Figure 12. Since the vertical magnification of the spectrometer is large and the vertical aper-

Figure 10: Optics of the Single Arm Spectrometer

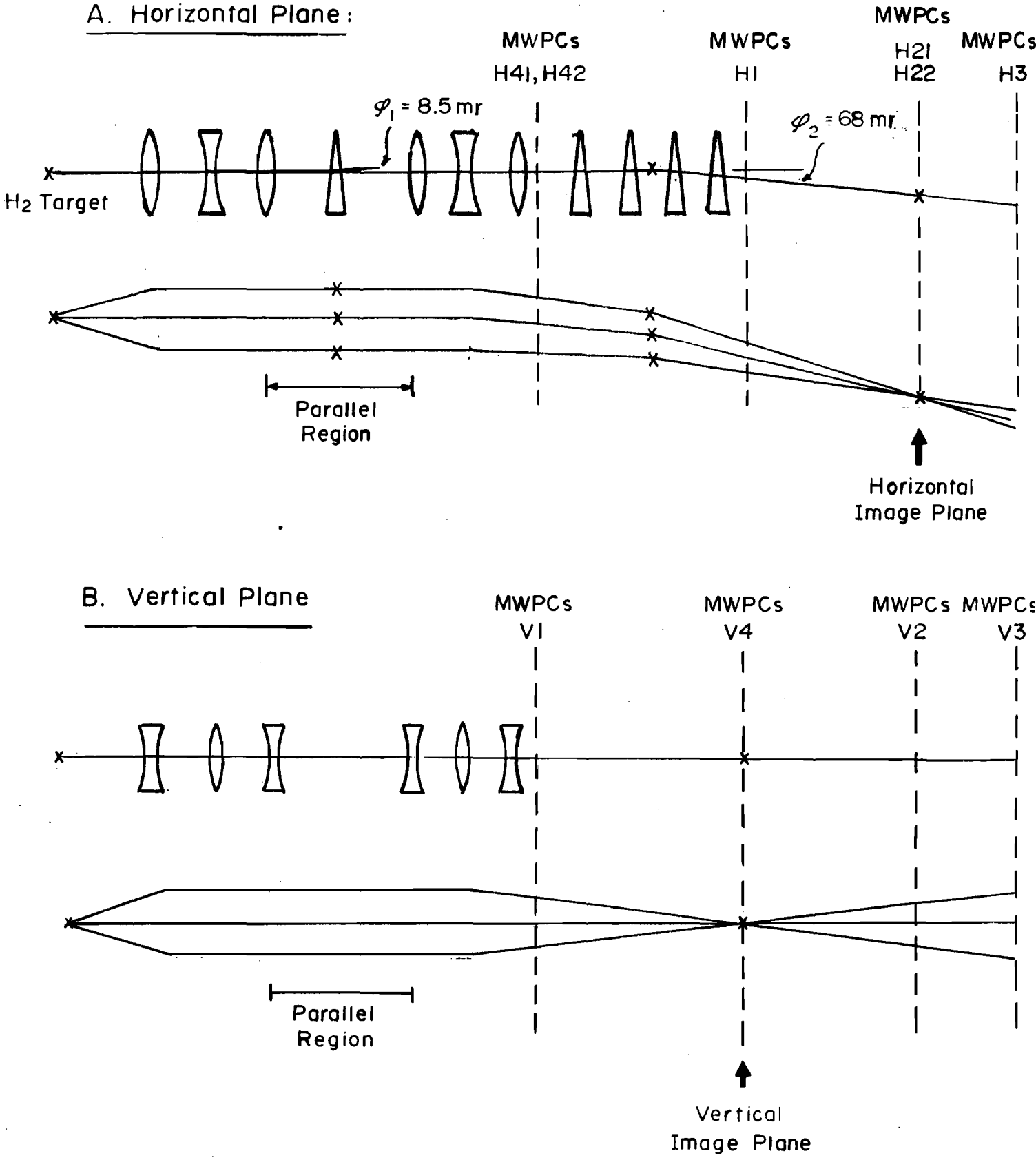

TABLE 3

Summary of Spectrometer Optical Properties

Horizontal Plane:			
Focal Plane: (107.27')	angular dispersion:		2.9 cm/mr
Image Plane: (377.7')	magnification:		1.8
	momentum dispersion:	spatial:	3.7 cm/%
		angular:	0.7 mr/%
Vertical Plane:			
Focal Plane: (88.06')	angular dispersion:		1.03 cm/mr
Image Plane: (269.3')	magnification:		4.08
	momentum dispersion:	spatial:	0.0
		angular:	0.0
Parallel Region:	beginning		78.5' from H_2 target
	end		135.8' from H_2 target
	length		57.3'
Spectrometer Acceptance:			
Horizontal angle (uniform):			1.5 mr
Vertical angle (uniform):			3.0 mr
Momentum (uniform):			5.0%
~~Total~~ Solid angle: (uniform)			~ 4.5 μster
(total)			~ 7.0 μster
Vertical height at target:			at least 9 mm
Horizontal extent at target:			~ 16mm

Solid angle as a function of veto counter setting near spectrometer focal plane: $\Delta\Omega(\mu ster) = .335\ \Delta x(cm)\Delta y(cm)$
Δx, Δy horizontal and vertical veto counter opening resp.

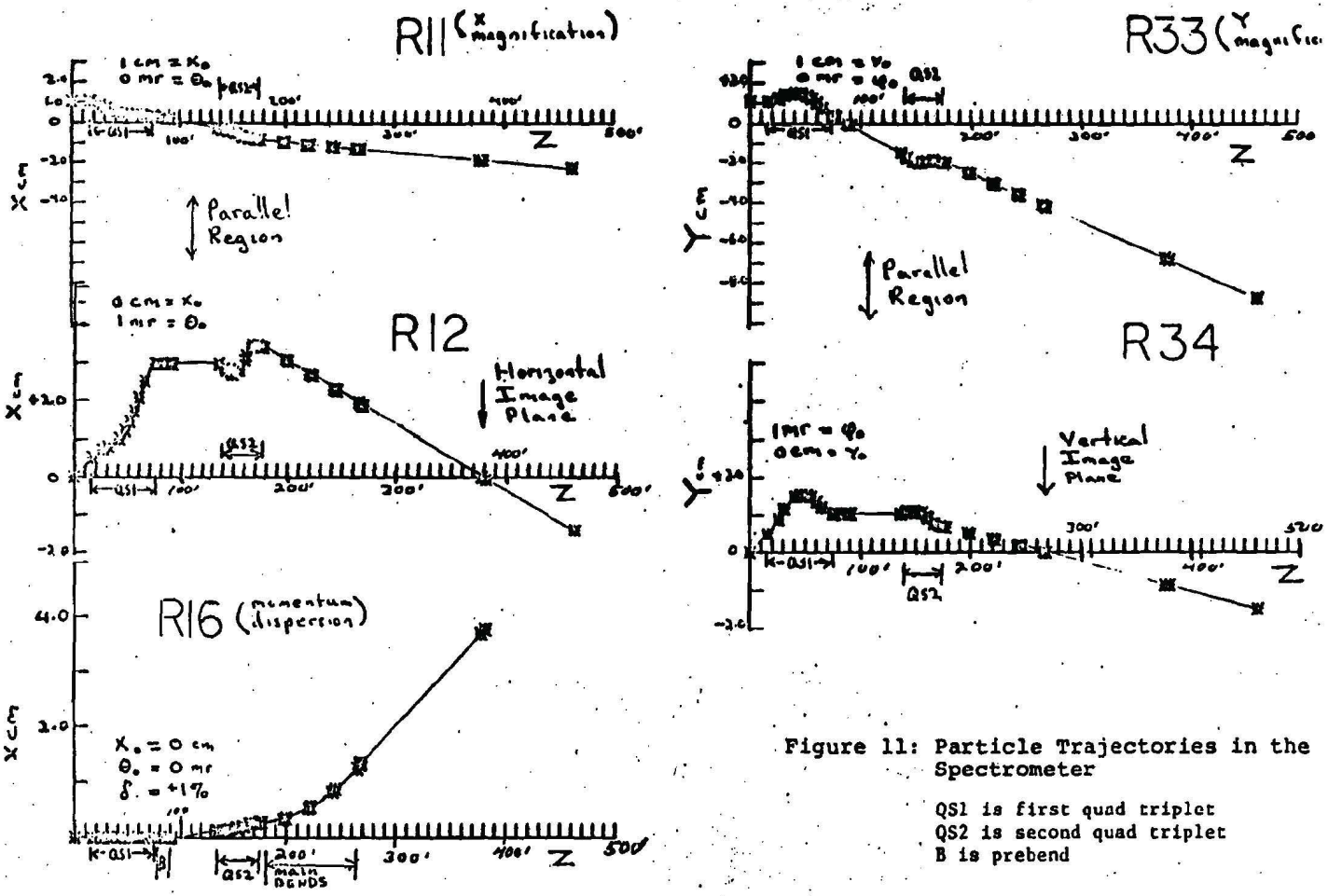

Figure 11: Particle Trajectories in the Spectrometer

QS1 is first quad triplet
QS2 is second quad triplet
B is prebend

Figure 12. SOURCE (object) AS VIEWED BY SPECTROMETER

(a) Horizontal Plane

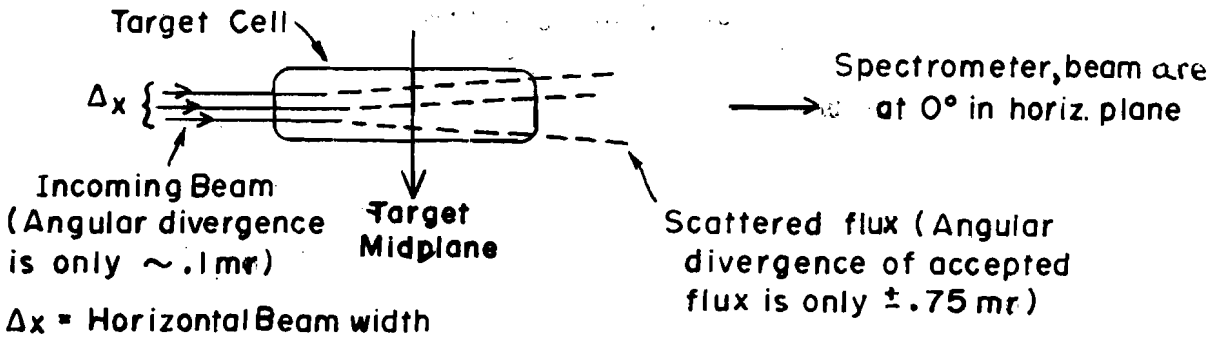

Horizontal object size ≈ Horiz. beam size at target midplane

(b) Vertical Plane

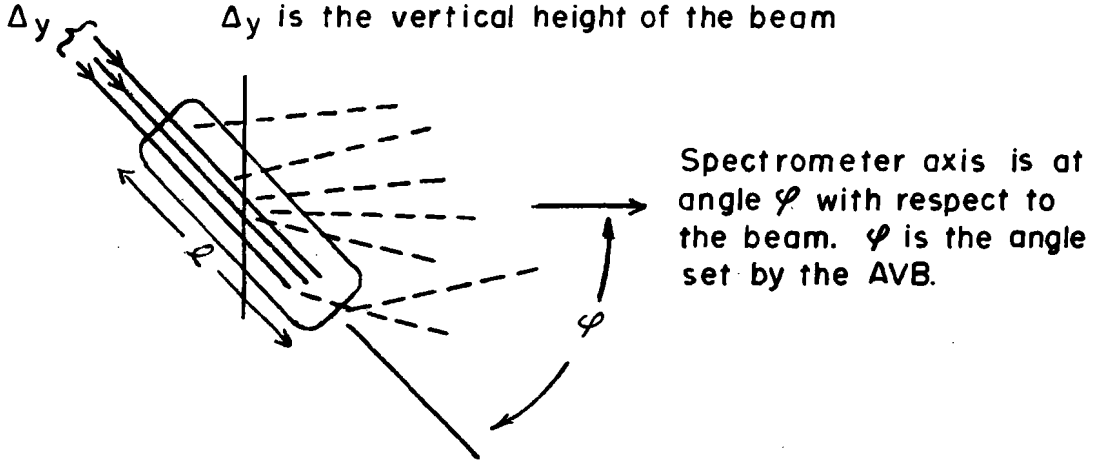

Object formed at the target midplane has a size which is approximately $\ell\varphi + \Delta y$. The vertical height increases linearly with scattering angle

ture is constrained by the aperture of the dipoles, it becomes impossible to see the whole 20" target if the scattering angle approaches 20 mr. In this experiment, we have scattered at angles up to 16 mr at 50 GeV/c. We have checked that we have full vertical acceptance by taking some data on a 10" target. The agreement between cross-sections obtained with the two targets proves that we were seeing the whole 20" target.

For a source of 16 mm x 10 mm or less, the uniform acceptance region of the spectrometer is predicted to be approximately 3.0 mr in vertical angle by 1.5 mr in horizontal angle. The uniform momentum acceptance is 5%. These numbers have been verified in several ways which are described below (Section IV).

D. FUNCTIONAL DESCRIPTIONS OF DETECTORS

Detectors located in the M6 beam, the Single Arm Spectrometer, and in the target area accomplish three general purposes.

i) to provide a fast trigger which initiates the data acquisition cycle. The trigger selects candidates for elastic scattering events.

ii) to identify the incoming particles and the fast scattered particle as pions, kaons, or nucleons.

iii) to measure the trajectory of the incident particle and the fast forward-scattered particle.

The relevant dimensions of all scintillation counters are given in Table 4.

A brief functional description of the detectors is given below. Figure 13 shows the location of the detectors along the beam and spectrometer.

TABLE 4

Geometry and Location of Scintillation Counters

Trigger Counters:

name	location from production target	height	horizontal extent transverse to beam	thickness along beam
BT1	1036.79' (second focus of M6 beam)	7/8"	2"	1/8"
BT2	1456.83 (between AVB2 and AVB3)	8 mm	16 mm	1/16"
ST1	1737.43 (exit of spectrometer bends)	2"	4"	1/16"
ST2	1932.73 (end of spectrometer)	6-1/2"	14"	1/4"

Beam Hodoscopes:

name	location	# of elements	Decode sense	element extent in decode plane	element thickness along beam
BP	1037.865' (second focus of M6 beam)	30	horitonzal	2.504 mm	10 mm
Bθ	1400.384' (just after Q17)	8	horizontal	3.385 mm	5 mm
Bϕ	1400.384'	8	vertical	3.49 mm	5 mm
BX	1454.458' (between AVB2, AVB3)	16	horizontal	0.965 mm	3 mm
BY	1456.073'	8	vertical	0.965 mm	3 mm

TABLE 4 (cont)

Spectrometer Hodoscopes:

name	location	# of elements	Decode sense	element extent in decode plane	element thickness along spectrometer axis
SF1	1559.894'	10	vertical	6.45 mm*	3 mm

*This is a third-lapped hodoscope. There are 19 logical bins of size 2.15 mm. To accomplish this the last counter on each end is 2/3 the size of the other counters, that is, 4.30 mm. The arrangement is:

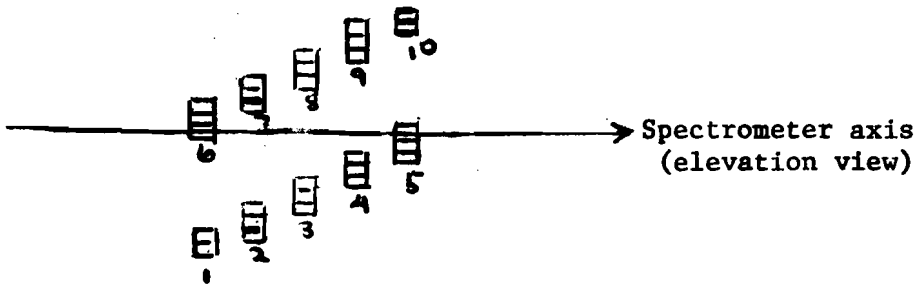

Counters 1, 10 are 2/3 the size of 2 through 8

Down

Recoil Hodoscopes:

name	location	# of elements	element thickness	length parallel to beam axis	element size transverse to beam axis
RZ**	6" below target	16	1/8"	40"	2.25"
RF1**	40" below target	32	3/8"	46"	1"

**These counters are also third-lapped. The RZ-hodoscopes have 29 logical bins 3/4" wide and 2 end bins 1-1/2" wide. The RF1-hodoscopes have 61 logical bins 1/3" wide and 2 bins of the end 2/3" wide.

TABLE 4 (cont)

Veto Counters:

name	location	size of hole	thickness along beam	horizontal	vertical	# of scintillators	# of phototubes
B3jaws	(parallel region 3rd stage)	both horizontal and vertical from 0 to ∿3"	1/2"	2"	2"	4	4
Sjaws	(spectrometer vertical focal plane	both horizontal and vertical opening variable from 0 to ∿3"	1/2"	2"	2"	4	4
BTO	(directly before target)	both horizontal and vertical opening variable. There is a fixed hole to back up the variable hole.				4 moveable + 1 fixed	1

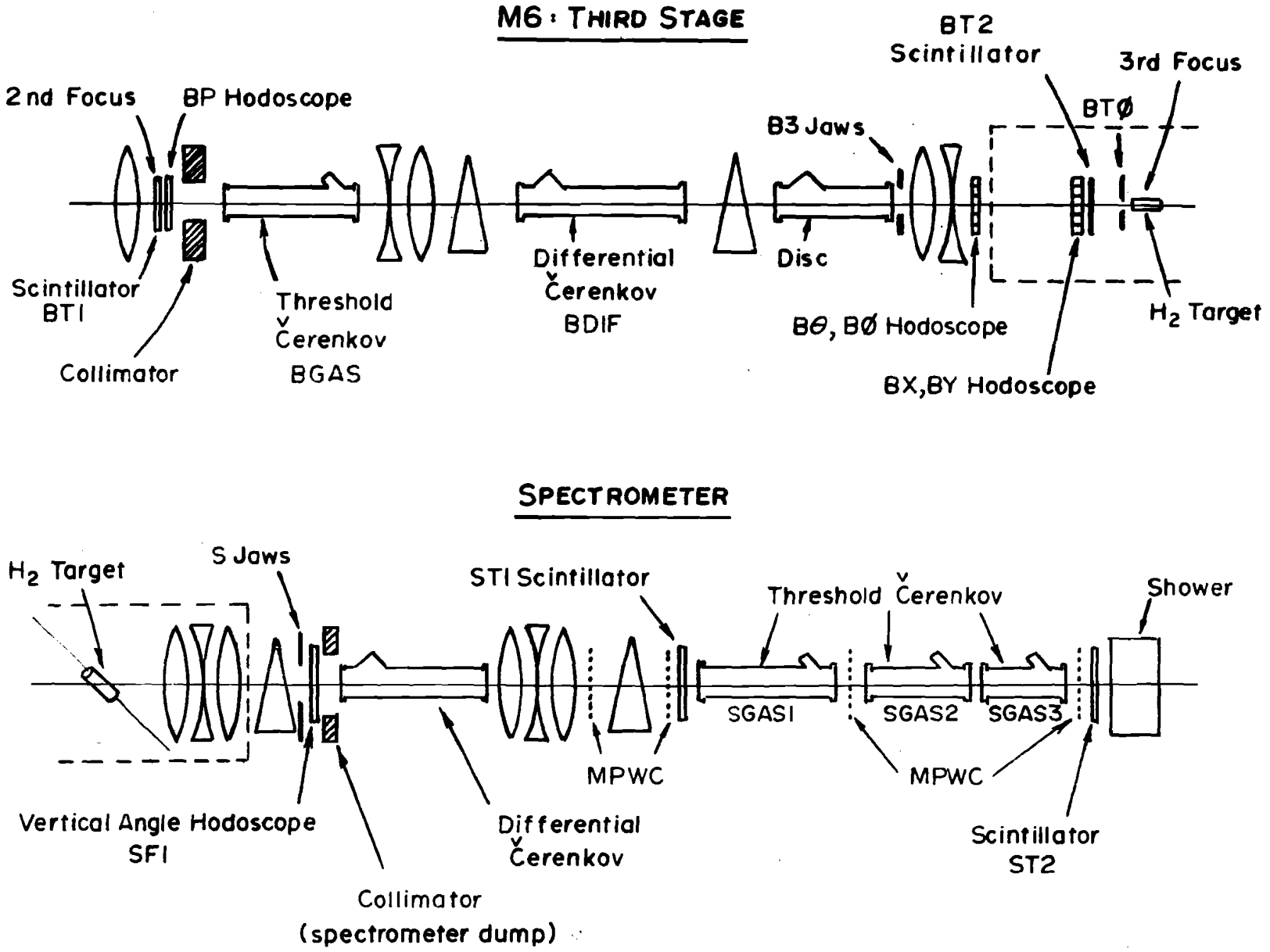

Figure 13: Location of Detectors in M6 Beam and Single Arm Spectrometer

1. Trigger counters

Beam trigger: A coincidence between the two trigger counters 'BT1' and 'BT2' formed the basic beam trigger requirement. 'BT1' was located at the second focus of the M6 beam line. BT2 was located between AVB2 and AVB3 approximately 12' from the scattering target. The last 10' bend magnet of the AVB system shields the target and the spectrometer from background from this counter. Since the position of the beam in this part of the system changes as the scattering angle is varied (see Section IIIB), 'BT2' had to move vertically. The required motion is 127 mils per milliradian of scattering angle.

Additional counters in the beam vetoed particles which were outside certain fiducial regions. A hole counter - 'BTØ' - was situated directly in front of the target. The counter consisted of four scintillators viewed by one phototube. The scintillators were attached to vanes which could be independently driven by motors to adjust the size of the rectangular hole. A scintillator with a fixed hole, viewed by the same phototube, backed up the adjustable hole. This counter was used to veto beam halo, to control the size of the incident beam, and to veto particles which would clearly have missed the hodoscopes near the target. Another hole counter - 'B3 jaws' - consisted of four square scintillators, each viewed by its own phototube, located in the parallel region of the third stage of the beam. The counters could be independently positioned so as to form a rectangular opening whose size limited the angular acceptance of the beam and contained the beam on the beam hodoscopes.

The coincidence of BT1 and BT2 was always required for a trigger. The other counters were usually used in veto.

Spectrometer trigger: The coincidence of the two trigger counters 'ST1' and 'ST2' formed the basic spectrometer trigger requirement. This coincidence constituted the electronic definition of a scattered particle. 'ST1' was located directly after the last bend magnet of the spectrometer. The rates in this region were always fairly low ($< 10^4$ counts/pulse). 'ST2' was located at the end of the spectrometer.

In addition, a variable hole counter consisting of four square scintillators each monitored by its own photo-tube could be used to veto scattered particles. Since this counter was located near the spectrometer focal plane, its square hole defined a precise solid angle acceptance. Usually, the opening was set to correspond to the uniform acceptance region of the spectrometer. The counter was only used as an electronic veto when the event rate was very high or when background from the beam in the spectrometer was very high (i.e. very small angles). These jaw counters also played an important role in the online measurement of the spectrometer solid angle.

Final coincidence: A final coincidence was formed between the 'beam trigger' and the 'spectrometer trigger' and constituted the 'event trigger'. This trigger initiated the computer data acquisition cycle which collected information about the event candidate from hodoscopes, MWPCs and Cerenkov counters. A second kind of trigger, based only on beam trigger counters, is discussed in Section IIIE.

2. Particle Identification

A total of seven Cerenkov counters are available in the M6 beam and the Single Arm Spectrometer. These provide complete identification of pions, kaons, and nucleons in both the beam and the spectrometer.

a) Beam particle identification

i) A threshold Cerenkov counter, called 'Bgas'[18] was located just downstream of the second focus. Cerenkov light was collected at the downstream end of the counter by a spherical lucite mirror and focused onto an RCA-C31000M phototube. The radiator was 18.0 meters of helium gas. The geometry of this counter is shown in Figure 14 and its vital statistics are listed in Table 5. The black acrylic tube is highly reflecting at grazing angles of incidence. The tube is used to reduce the diameter, D, of the counter which otherwise must be D = beam height + 2x counter length x maximum Cerenkov angle. The detection efficiency for this counter is dominated by photoelectron statistics. The average number of photoelectrons $\bar{n}$, is given by

$$\bar{n} = N_0 \theta^2$$

where θ is the angle of the Cerenkov light. The efficiency, ε, is then

$$\varepsilon = 1 - e^{-\bar{n}} .$$

The quantity N_0 depends on the length of the counter, the photon collection efficiency, and the quantum efficiency of the photocathode. N_0 is a useful quality factor for the counter's performance. The N_0 for this counter was typically 150 x length of counter.

The helium pressure was set so that this counter was sensitive to pions but not to kaons or protons. The coincidence signal between

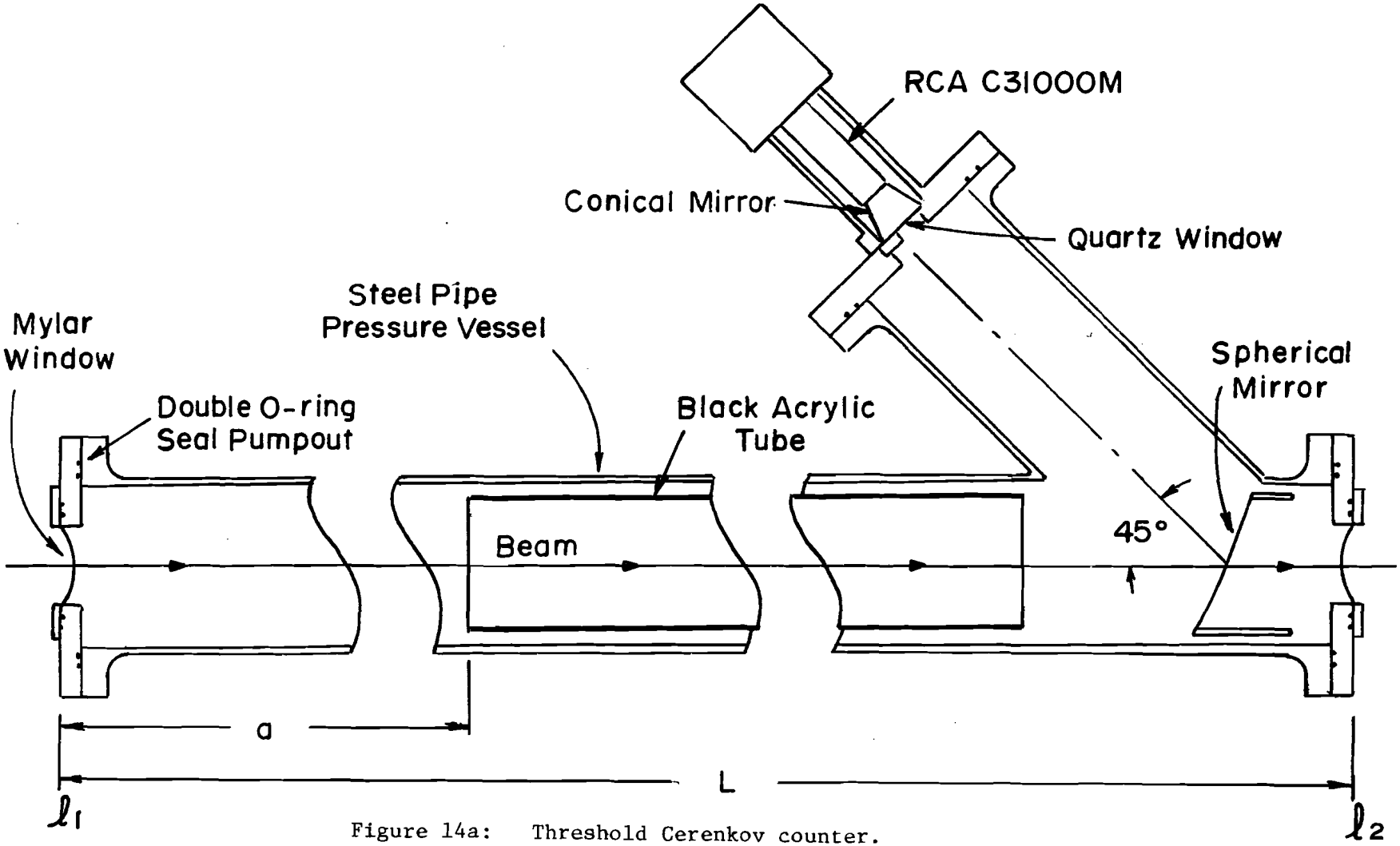

Figure 14a: Threshold Cerenkov counter.
SKETCH OF A TYPICAL COUNTER. INTERMEDIATE FLANGES ARE NOT SHOWN.

Figure 14b: NAL Differential Cerenkov Counter

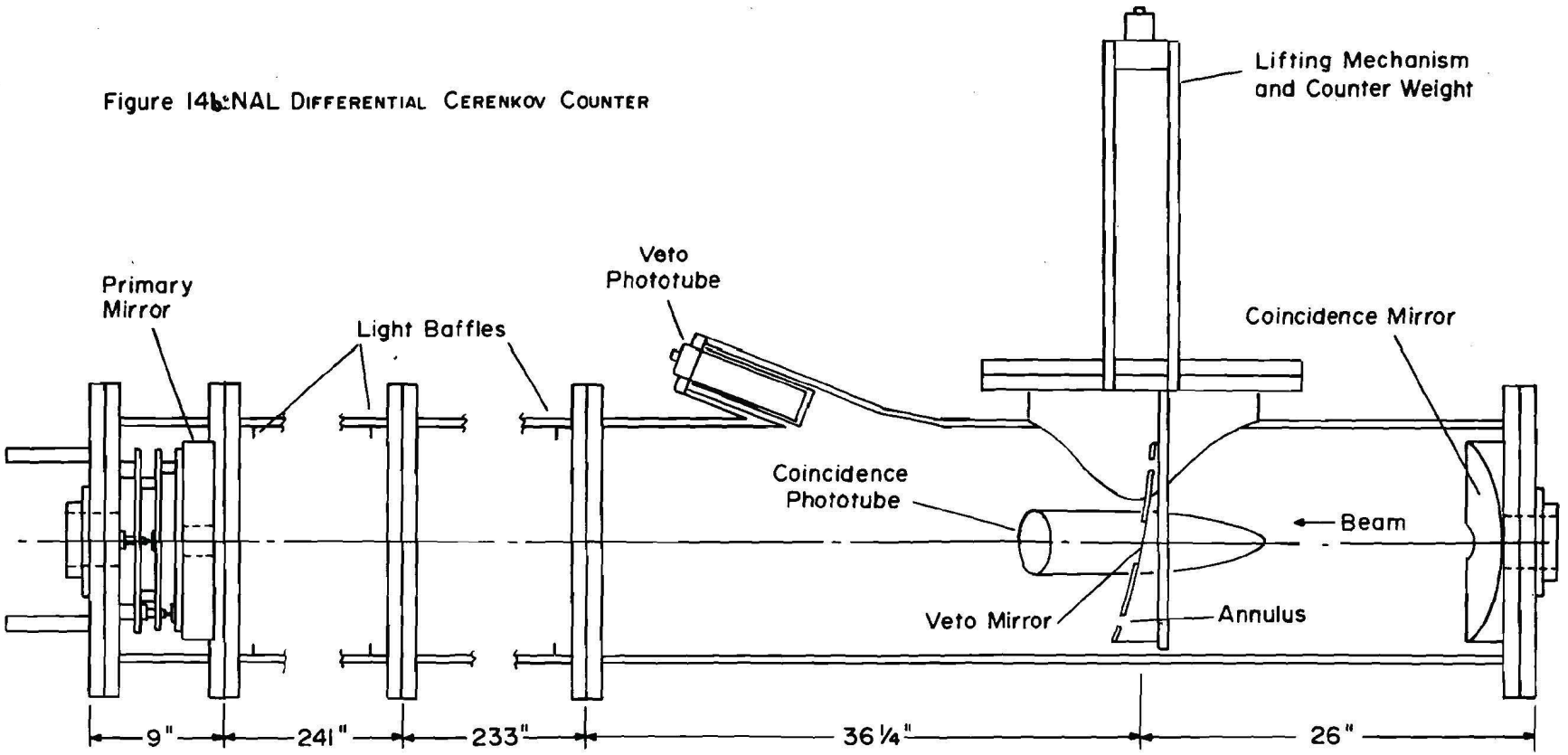

TABLE 5

Threshold Cerenkov Counter Parameters

Counter	B_{gas}	S_{gas1}	S_{gas2}	S_{gas3}
Radiator Length	18.0 m	31.5 m	14.2 m	6.9 m
Length (L), window-to-window	59'4"	104'	48'	24'
Number of pipe sections	2	3	1	1
Upstream window position (ℓ_1)	1052'	1742'	1854'	1905'
Downstream window position (ℓ_2)	1112'	1847'	1902'	1929'
Steel pipe OD	8.63"	12.75"	16.00"	16.00"
Steel pipe ID	7.98"	11.94"	15.00"	15.00"
Planned max. beam diam., entrance	3"	4.4"	8.8"	11.6"
Planned max. beam diam., exit	3"	8.8"	11.6"	13.0"
Cylindrical mirror ID	6.75"	10.75"	13.75"	13.75"
Entrance window to acrylic distance (a)	15'	33'	18.5'	3.5'
Maximum Cerenkov angle from (a)	10 mr	8 mr	10 mr	14 mr
Spherical mirror material	Lucite	Lucite	Glass	Glass
Spherical mirror thickness	1/16"	1/8"	3/32"	3/32"
Spherical mirror focal length	25"	25"	32"	32"
Pressure limit for initial expts.	29.5 PSIA	30 PSIA	75 PSIA	75 PSIA
Gas for initial expts.	He	He	N_2/He	N_2/He
Beam window material	Mylar	Mylar	Al	Al
Beam window thickness	0.005"	0.010"	0.055"	0.055"

this counter and the beam trigger was scaled to obtain the flux of pions in the beam. Flag-bit information for this counter was transferred to the computer for every event for use, both online and off-line, in particle identification.

ii) Beam differential counter

A differential counter - 'Bdif'[19] - was located in the parallel region of the third stage. This is nominally a parallel region but since it is located upstream of the recombination dipoles, there is angular dispersion associated with off-momentum particles. The angular divergence is $\sim$ .35 mr.

Cerenkov light emitted as a particle traversed 411" of radiator, either helium or nitrogen, was collected by a mirror - the 'primary mirror' - at the downstream end of the counter and formed into a ring of light travelling upstream. The pressure (index of refraction) was adjusted so that the cone of Cerenkov light from the desired particle type (i.e. with the correct mass) would fall on an annular opening cut in a second mirror - the 'anticoincidence mirror' - at the upstream end. The annulus accepted light emitted at an angle of $10 \pm .6$ mr. Light passing through the annulus was focused by a third mirror - the 'coincidence mirror' - onto either of two phototubes called 'BD1FR1' and 'BD1FR2'. Light from particles with the wrong mass would miss the annulus and would be focused by the anitcoincidence mirror onto a veto counter called 'Bdifa'. A signal from BD1FR1 or BD1FR2 was evidence that the particle had the desired mass. Rejection of unwanted particles was improved by requiring both BD1FR1 and BD1FR2 and/or by rejecting events for which BD1FA fired.

TABLE 6

Properties of Differential Cerenkov Counters

a. Beam Differential Counter

Radiating material:	helium or nitrogen
Cerenkov angle:	10 mr
Phototubes:	RCA 8850 (three) with quartz envelopes to extend response to 1800 Å.
Primary mirror:	Focal length 511" Diameter 24" Exit hole for beam 2" dia. Thickness 2"
Effective Radiator Length:	411"
Anticoincidence mirror:	Focal length 23" Diameter 13" Thickness 2" Annulus width 1-1/2 cm = 1.2 mr
Coincidence mirror:	Same diameter, thickness and focal length as anticoincidence mirror. There is no annulus and the mirror is split to send some light to the left and some to the right.

b. Spectrometer Differential Counter

Radiator:	helium or nitrogen
Cerenkov angle:	8.5 or 10.0 mr
Phototubes:	RCA 8850 (2) (quartz envelope extends response to 1800 Å.)
Primary mirror:	Focal length 382.5" Diameter 12" Thickness 2" Hole size 2-1/2" square
Anticoincidence mirror:	Focal length 23" Diameter 13" Hole size 2-1/2" square Thickness 1/4" Annular aperture 1, 1.5, 2.0 cm 1 cm = 1 mr of angular acceptance.
Coincidence mirror:	Same as anticoincidence mirror but with no annulus.

At 50 GeV/c, we set the pressure so that light from kaons fell on the annulus. At the other energies, the pressure was set to bring proton light onto the annulus. The signals were scaled to provide flux information and flag-bit information for each of the three photo-tubes was transferred to the computer for each event.

A sketch of this counter is shown in Figure 14 and Table 6a lists its important characteristics.

A two inch hole in the primary mirror is necessary to reduce multiple scattering of the beam. The effective radiator length of 411" includes the correction for the loss of Cerenkov light falling on this hole.

Alignment of the counter's axis with the beam is accomplished by pivoting the primary mirror (remotely) until the Cerenkov light falls squarely on the annulus. The counter itself does not have to be moved.

iii) Disc Cerenkov Counter

The Disc (Differential Isochronous Self-Collimating) Cerenkov counter[20] was located downstream of the recombination dipoles in the third stage. The beam is recombined in momentum and parallel in this region. A sketch of the Disc counter is shown in Figure 15.

The cone of light emitted by a particle traversing the five meters of helium radiator is collected by a mirror at the downstream end of the Disc. This light is focused onto an annular aperture at the upstream end. The aperture accepts light emitted at an angle of 24.5 milliradians. The aperture is monitored by eight Phillips 56 Duvp photo-tubes arranged in a circle.

The chief purpose of the Disc was to separate pions and kaons at very high energies. To accomplish this, it is necessary to detect the very small angular separation between two cones of Cerenkov light. The width of these cones is increased by geometric aberrations of the mirror and the chromaticity of the gas radiator. The Disc corrects for these two effects with its internal optics. A chromatic corrector, consisting of a triplet of lenses with appropriate refraction indices, suppresses the chromatic spreading by a factor of 15. An additional lens, the 'coma corrector', reduces the principle geometric aberration. The excellent angular resolution is related to the velocity resolution according to the equation:

$$\theta \, d\theta \simeq \Delta\beta \, .$$

At 140 GeV/c, the velocity resolution required for π-K separation is $\Delta\beta/\beta = 1.92 \times 10^{-6}$.

The width of the Disc aperture can be varied remotely by motors. If signals from all eight phototubes are demanded, a very precise definition of the Cerenkov cone is possible and very high rejection results. The low light level of Cerenkov radiation causes the efficiency to be reduced if all eight counters are required. If $\overline{N}$ is the average number of photoelectrons emitted from the eight photocathodes due to the Cerenkov radiation, Poisson statistics gives the efficiency as:

$$\text{efficiency} = \left(1 - e^{-\overline{N}/8}\right)^8$$

For $\overline{N} = 32$, the resulting efficiency is 86%.

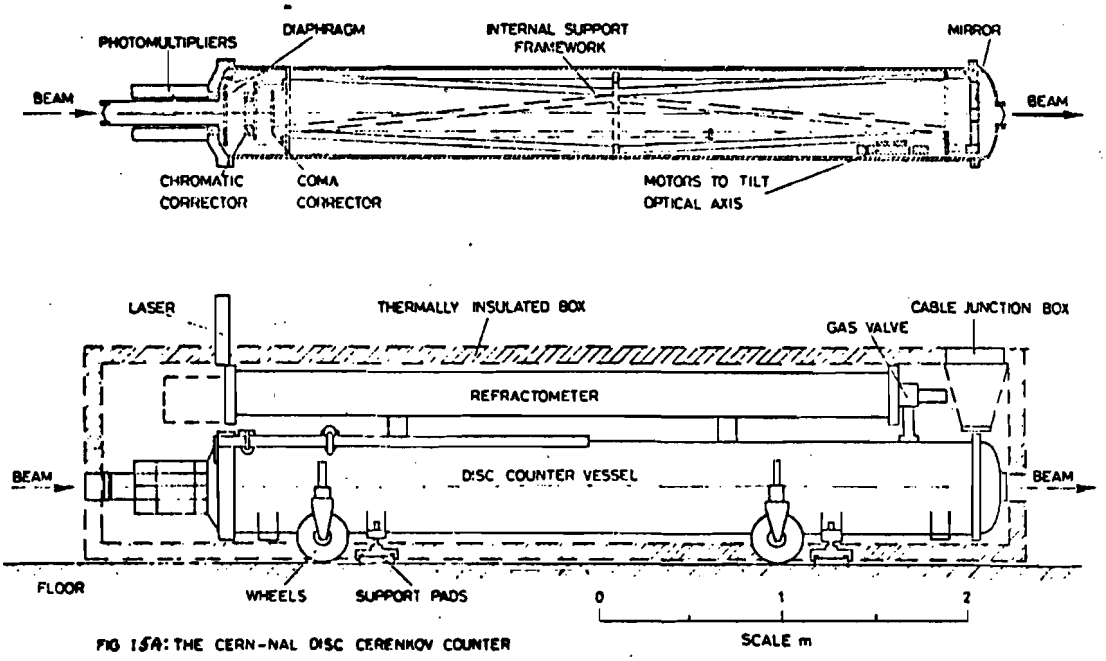

FIG 15A: THE CERN-NAL DISC CERENKOV COUNTER

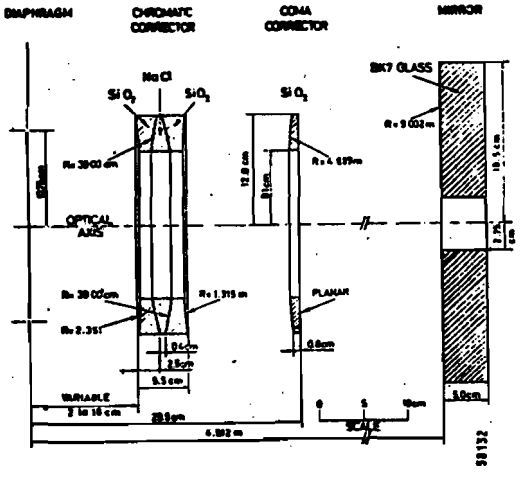

Figure 15b: Disc Optics

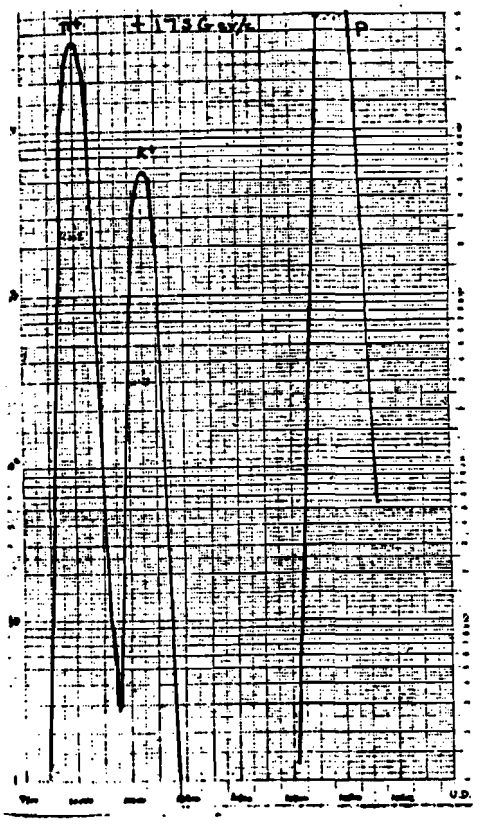

Figure 15c: Pressure Curve 175 GeV/c

Figure 15: Disc Cerenkov Counter

To improve the efficiency we have typically required any three out of four of the even-numbered counters and three out of four of the odd-numbered counters. The efficiency in this mode of operation was high, $\sim$ 95% at 140 GeV/c, and the rejection of pions from the kaon signal was several orders of magnitude.

The absolute index of refraction of the radiator is measured by a precision laser interferometer to an accuracy of 3×10^{-8}. The ability to measure the index of refraction, rather than just the pressure, enables the Disc to directly measure the momentum of the beam. This is discussed further in Section IV.

A pressure curve for the Disc is shown in Figure 15c.

Alignment of the Disc with the beam axis is accomplished by pivoting the internal optics so as to maximize the light falling on the annulus. The pressure vessel itself does not have to be moved.

At all energies except 50 GeV/c, the Disc was sensitized to kaons. At 50 GeV/c, it was set for protons. Flag-bits for each photo-tube were transferred to the computer for each event. The output of the photo-tubes was also processed by the fast electronics to obtain the flux (kaon or proton) for use in the analysis.

Spectrometer particle identification: Four Cerenkov counters were used to identify particles which scattered into the spectrometer. Three of these were threshold counters, called 'Sgas1', 'Sgas2', and 'Sgas3'. They were similar in design to the beam threshold counter. Their properties are listed in Table 5. The counters differ from each other in length, diameter, mirror construction, window material, and pressure limitations. Both helium and nitrogen were used as radiators. The pressure in Sgas1 was set below K threshold so that it was sensi-

tive only to pions. Sgas2 and Sgas3 were operated between kaon and nucleon threshold so that they counted pions or kaons. A kaon signal was formed by vetoing the π+K signal from Sgas2 and Sgas3 with the π signal from Sgas1.

The fourth Cerenkov counter, 'Sdif', is a differential counter which is similar in design to the beam differential counter described above. A large motor-driven wheel holds several different anti-coincidence mirrors. These mirrors differ in the diameter and width of the annulus. A list of the properties of this counter, including the properties of the various mirrors, is given in Table 6b. Unlike the beam differential counter, this counter has only one phototube - 'SdifR' - viewing the annulus. The phototube 'sdifa' views the light from the anti-coincidence mirror.

3. Trajectory Measurement

a) Measurement of incident particle trajectory

The trajectory of a particle incident on the hydrogen target is specified by five quantities (see Figure 16a):

i) The horizontal position at the target midplane $\equiv X_i$

ii) The horizontal angle relative to the direction of the central beam axis $\equiv \theta_i$

iii) The vertical position at the target midplane $\equiv Y_i$

iv) The vertical angle relative to the direction of the central beam axis = ϕ_i

v) The percent deviation of the particle's momentum P_i from the central momentum P_b^c of the beam: $\delta_i = (P_i - P_b^c)/P_b^c \times 100$.

These quantities are measured by five hodoscopes, BX, BY, Bθ, Bφ, and BP, located in the M6 beam (see Figure 13). The location and characteristics of the hodoscopes are given in Table 4.

The track in each hodoscope is converted to a coordinate (in cm) relative to the center of the hodoscope. Alignment procedures using the trim (vernier) magnets in the beam guarantee that the central axis of the beam passes through the center of all the hodoscopes. The incident coordinates are determined from the hodoscope coordinates as follows:

1) horizontal angle

$$\theta_i = (X(BX) - X(B\theta))/\ell_1 \times 1000 \text{ milliradians}$$

where X(BX) is the horizontal coordinate in the BX hodoscope in cm, X(Bθ) is the horizontal coordinate in the Bθ hodoscope in cm, and ℓ_1 = 1689.2 cm is the distance between the two hodoscopes.

2) vertical angle

$$\theta_i = (Y(BY) - Y(B\phi))/\ell_2 \times 1000 \text{ milliradians}$$

where Y(BY) is the vertical coordinate from the BY hodoscope in cm, Y(Bφ) is the vertical coordinate in the Bφ hodoscope in cm, and ℓ_2 = 1676.0 cm is the distance between the two hodoscopes.

3) horizontal position at target midplane

The horizontal coordinate at the target midplane is obtained by continuing the line determined by the coordinates X(BX) and X(Bφ) to the target midplane

$$X_i = X(BX) + \theta_i \times \ell_3/1000 \text{ cm}$$

$$= X(BX) \{1 + \ell_3/\ell_1\} - X(B\theta) \ell_3/\ell_1$$

where ℓ_3 = 457.2 cm is the distance from the BX hodoscope to the target midplane.

4) vertical position at the target midplane

$$Y_i = Y(BY) + \phi_i \ell_4/1000 \text{ cm}$$

$$= Y(BY) \{1 + \ell_4/\ell_2\} - Y(B\phi) \ell_4/\ell_2$$

where ℓ_4 = 433.2 cm is the distance from the BY hodoscope to the target midplane.

5) percent momentum deviation

The quantity δ_i is measured directly by the BP hodoscope. The relation between the horizontal coordinate X(BP) in the hodoscope (in cm) is

$$X(BP) = 1.576 X_0 + 4.44 \delta_i$$

Figure 16. Incident and Scattered Particle Coordinate System

(a) Incident Particle Coordinate System.

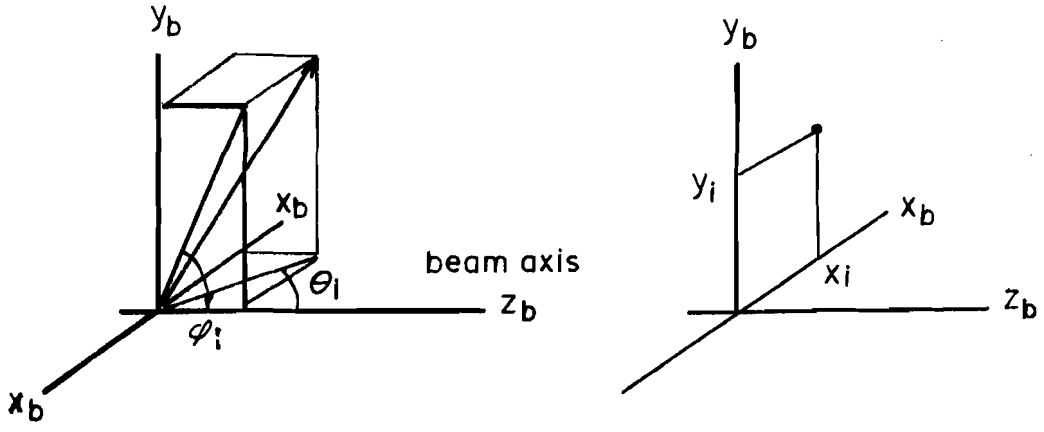

(b) Scattered Particle Coordinate System

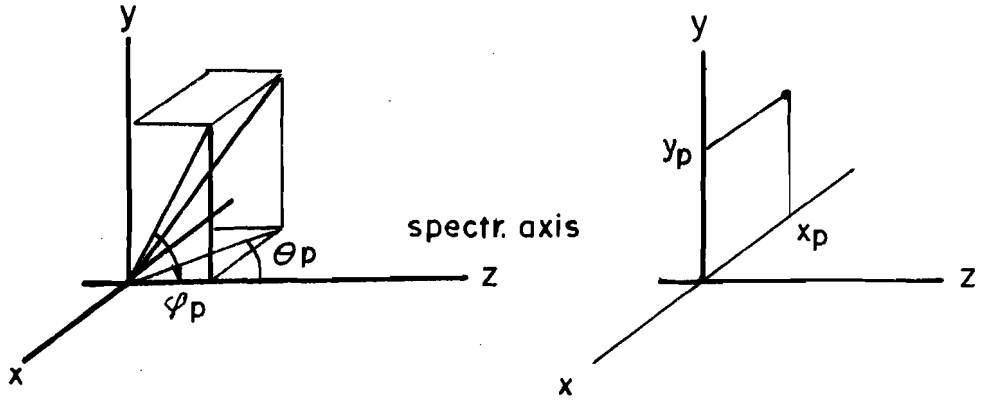

(c) Relation between Incident and Scattered Particle Coordinate Systems

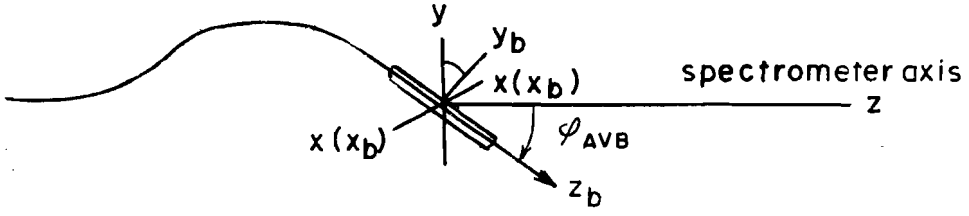

y, y_b, z are all in the same plane

The angle between y and y_b is φ_{AVB}

where X_0 is the horizontal position at the midplane of the Meson Lab Production Target. The coefficients are determined by the computer program TRANSPORT and have been verified by direct measurements on the beam.

X_0 may be any position within the 1 mm wide production target. Since it is not measured, it is set to 0 and the full target extent ΔX_0 is taken as the uncertainty* in X_0. Then

$$\delta_i = \frac{X(BP)}{4.44}\%$$

b. Measurement of the scattered particle trajectory

The trajectory of the scattered particle is measured by a system of ten multi-wire proportional chambers. The chamber sizes, wire spacings, number of wires, and locations are given in Table 7. The design of these chambers is described elsewhere.[21]

The chambers V1, V2, V3, and V4 are located after all the quadrupoles in the spectrometer. They define the projection of the trajectory on the vertical plane. This projection is a straight line and we choose to describe it by giving the vertical angle, ϕ_s, and the vertical position, Y_s, at the location of the chamber V2 (near the horizontal image plane). See Figure 17a.

---

*The uncertainty of the momentum measurement is

$$\sigma_{\delta_i} = \frac{1}{4.44\sqrt{12}} \sqrt{\Delta^2(BP) + (1.576\ \Delta X_0)^2}$$

where $\Delta(BP)$ is the hodoscope element size. The $1/\sqrt{12}$ comes from averaging the flat distribution of primary beam particles over the production target and the flat distribution of secondary particles over the hodoscopes.

TABLE 7

Geometry and Location of MWPCs in Spectrometer

Name	Location	# of 32 wire groups	# of wires	Sensitive Region horiz x vert (mm) (mm)	Decode Sense
V1	1645.54' (after last spectrometer quad)	2	64	180 x 128	vertical
H41	1644.18'	2	64	128 x 345	horizontal
H1	1738.13' (after last bend magnet)	2	64	128 x 180	horizintal
V4	1739.20' (spectrometer vertical focus)	1	32	280 x 64	vertical
H21	1847.58' (spectrometer horizontal focus)	4	128	256 x 90	horizontal
H22	1848.24'	4	128	256 x 90	horizontal
V2	1849.91'	1	32	280 x 64	vertical
H3	1930.17' (end of spectrometer)	5	160	320 x 190	horizontal
V3	1931.39'	2	64	345 x 128	vertical
H42	1646.45'	2	64	128 x 180	horizontal
Total wires:			800		

All chambers have 2 mm wire spacing.
H22 and H21 are offset horizontally by 1 mm to form a single logical chamber with 1 mm spacing.
H41 and H42 are arranged the same way.

Figure 17. SPECIFICATIONS OF THE SCATTERED PARTICLE TRAJECTORY AT THE BACK OF THE SPECTROMETER

(a) Vertical Plane (elevation view)

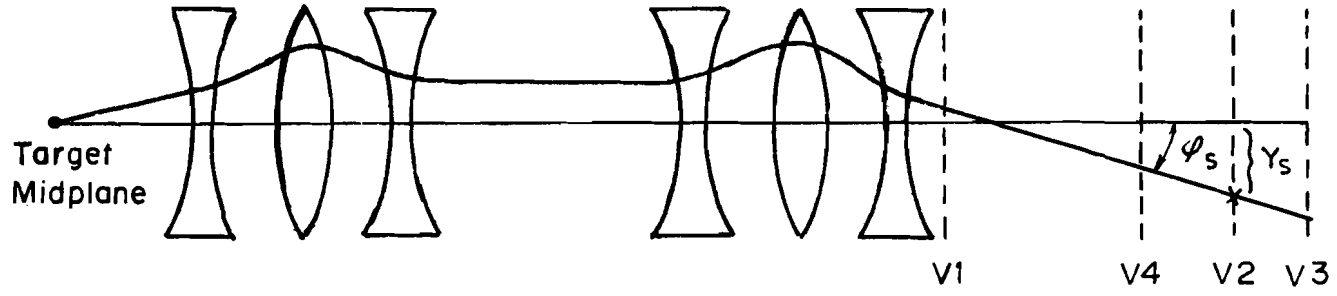

(b) Horizontal Plane (plan view)

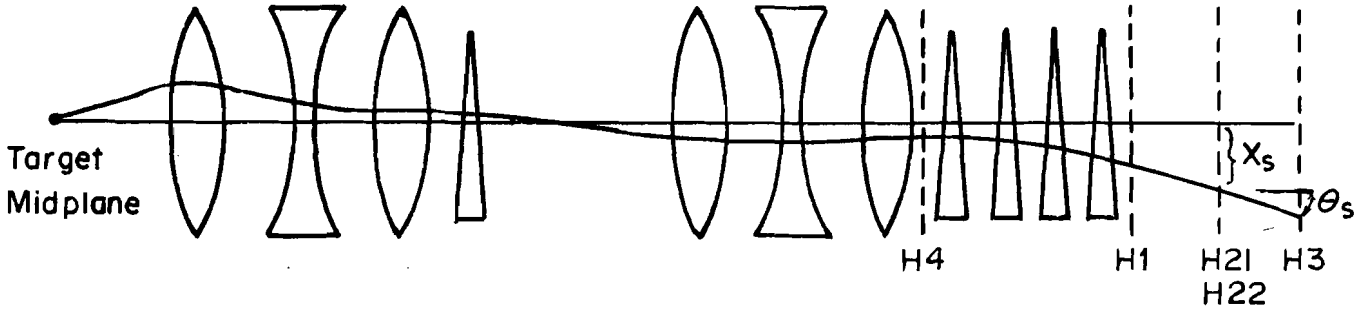

Y_s, φ_s, X_s, and θ_s specify the particle trajectory at the back of the spectrometer as measured by the MWPCs

The chambers H1, H21, H22, and H3 are located after all the magnets in the spectrometer. They define the projection of the trajectory on the horizontal plane. The planes H21 and H22 are located about 2 cm apart. They each have 2 mm wire spacing and are offset laterally by 1 mm with respect to each other. They function logically as a single chamber with 1 mm spacing. We choose to define the line by giving the horizontal position, X_s, and the horizontal angle, θ_s, at the position half way between H21 and H22 (the horizontal image plane). See Figure 17b.

The eight wire chambers mentioned above measure the horizontal and vertical positions and angles at the horizontal image plane. The next section explains how these quantities are traced back through the spectrometer to give the momentum and scattering angles of the particles.

Two additional wire planes, H41 and H42, are available for checking the optical properties (especially the horizontal acceptance) of the spectrometer and for special tracking procedures which are used in the analysis of inelastic scattering.

A scintillator hodoscope - SFI - consisting of ten counters, overlapping by thirds (see Table 4), is located at the vertical focal plane. This hodoscope measures the vertical height at the focal plane which is proportional to the vertical projection of the scattering angle measured from the spectrometer axis. The ten third-lapped counters form nineteen logical bins each subtending .22 mr at the target midplane. This hodoscope was primarily used to align the beam and spectrometer axes. It also provided a variable aperture which could be used to select events for online analysis.

Sketches of profiles of the scattered flux are shown for each chamber in Figure 18. In the vertical plane, the dominant feature is the sharp drop of the yield across the aperture due to the exponential variation of the cross section. Thus, SFI and the wire chambers V1, V2, and V3 all have most of their rate towards the small angle (small t) side of the spectrometer. At V4, the distribution is symmetric because V4 is at the vertical image plane. The position here is completely independent of scattering angle. In the horizontal plane, the dominant feature is the dispersion of the scattered flux according to momentum. At H1, the tail on the right side of the distribution is caused by the inelastic events bending away from the higher momentum (stiffer) elastic events. By H2, there is a clear elastic signal sitting on top of a broad low inelastic tail which extends to the right. The profile in this chamber does <u>not</u> represent our momentum resolution. It is smeared by the beam momentum bite and the horizontal object size. The calculation of the missing mass squared is discussed below. The profile in the plane H41 represents mainly the azimuthal angle bite of the spectrometer and is, therefore, nearly flat.

4. <u>Extraction of the coordinates of the scattered particle</u>

The trajectory at the target of the scattered particle is specified by the following five quantities (measured with respect to the spectrometer axis):

i) The horizontal position at the target midplane $X_p(X_1)$

ii) The projection of the scattering angle onto the horizontal plane $\theta_p \quad (X_2)$

iii) The vertical position at the target midplane $Y_p(X_3)$

iv) The projection of the scattering angle onto the vertical

Figure 18. DETECTOR PROFILES IN THE SPECTROMETER

(a) Vertical Plane (elevation view),

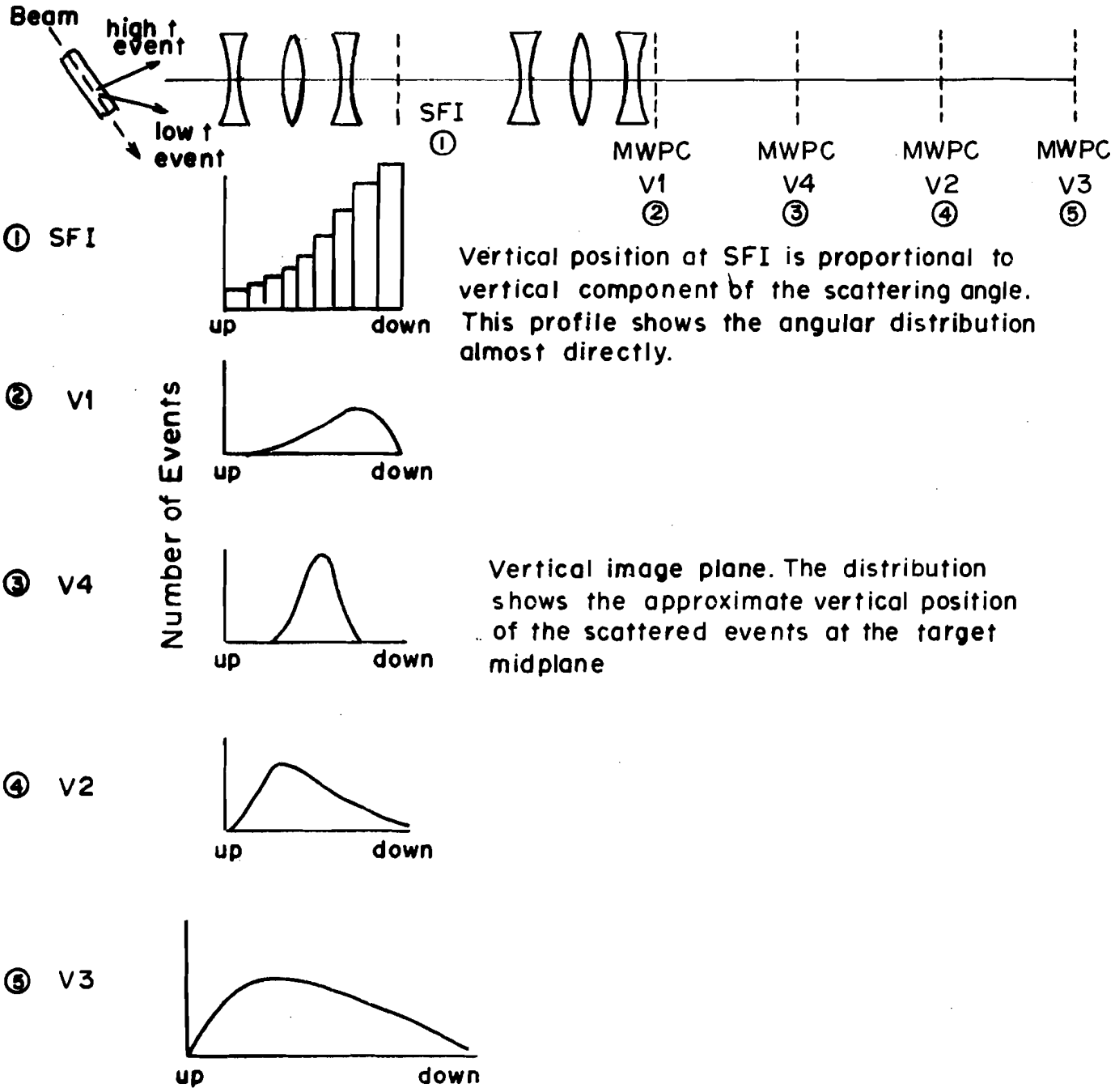

(b) Horizontal Plane (plan view)

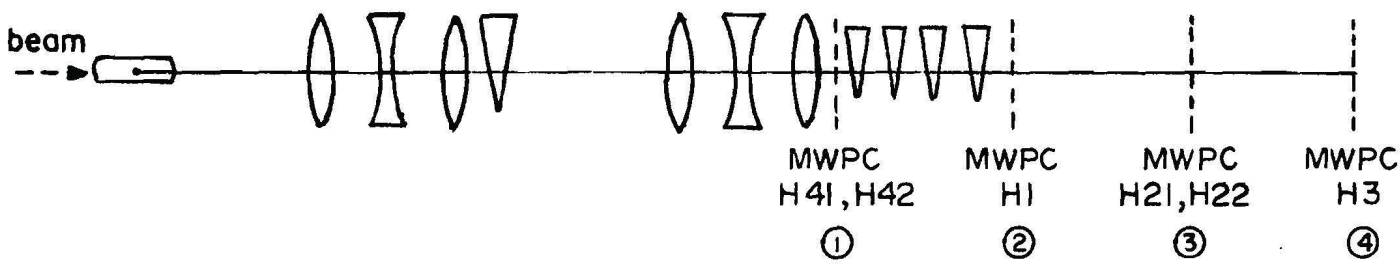

① H41 H42

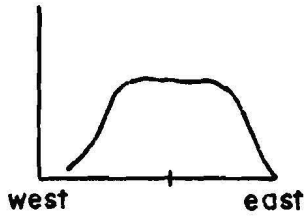

Reflects the horizontal angle acceptance. Shows a nearly flat (azimuthal) angle distribution.

② H1

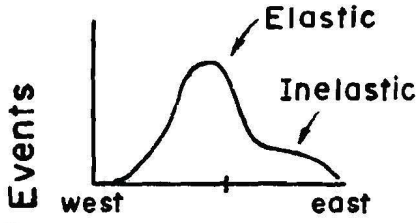

Located after the dipole magnets. Elastic and inelastic events begin to separate.

③ H21 H22

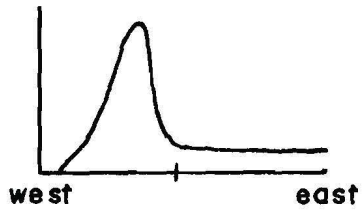

Horizontal image plane. Exhibits elastic peak smeared by beam momentum and width of beam at target

④ H3

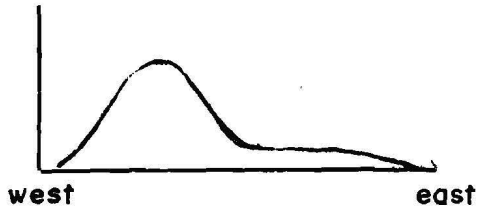

Located at the end of the system

plane ϕ_p (X_4)

v. The momentum deviation δ_p relative to central momentum, P_s^c, of the spectrometer: $\delta_p = \delta_s = (P_s - P_s^c)/P_s^c \times 100\%$ (X_5).

P_s is the momentum of the scattered particle. See Figure 16b.

In order to determine these five quantities from the trajectories measured at the end of the spectrometer, it is necessary to trace the rays measured in the MWPCs backward through the magnets of the spectrometer to the target. It is obvious that the four quantities measured in the MWPCs are insufficient for this purpose. If the scattered momentum were known, then four quantities would be sufficient. An additional horizontal coordinate upstream of the bend magnets must be measured to pin the momentum down. For our spectrometer, the best resolution is achieved by using the horizontal position of the scattered particle close to the target. This coordinate is obtained by assuming that all interactions occur at the target midplane. Then the coordinate can be approximated by the horizontal position at the target midplane of the incident particle. That is, $X_p \simeq X_i$. All this is illustrated in Figure 19. This approximation is very good. Consider a particle which scatters very far from the target midplane - say at the upstream end of the target. The error in our approximation is $\Delta X_p = \ell(\theta_i + \theta_p)$. θ_i is never larger than .2 mr and θ_p is never larger than $\sim$ .8 mr. ΔX_p for a 20" target in this worst case is $\sim$ .5 mm. When a proper average over the target length is taken, the average error is $\sim$ .15 mm. This error is less than the error due to the granularity of the BX-hodoscope.

To summarize, the five coordinates of the scattered particle at the target are determined by five quantities: the horizontal and verti-

cal position at the spectrometer horizontal focus, the horizontal and vertical angles at the same location, and the horizontal interaction point at the target midplane obtained approximately from the incident horizontal coordinate measured by the beam hodoscopes.

To obtain the scattered coordinates, one must still trace the rays back through the spectrometer. This involves integrating the equations of motion through the field distributions of the spectrometer. Since the phase space of the spectrometer is very small, it is sufficient to use a power series expansion about the central trajectory to solve the equation of motion for the lowest few orders only. This is the approach of the computer program TRANSPORT which performs these expansions for many commonly used field distributions. The input to TRANSPORT specifies all the field distributions - the position and fields of quadrupoles, dipoles, and drift spaces. The output consists of sets of "transfer matrices" which give at each position along the spectrometer a matrix which relates the coordinates at this position to the initial coordinates.

We consider a particle which leaves the target midplane with coordinates $\vec{X}^{\circ} = (X_p, \theta_p, Y_p, \phi_p, \delta_s)$. The coordinates of its trajectory as it passes through the plane at a distance z along the central trajectory and perpendicular to it are

$$x_{z_i} = \sum_{j=1}^{5} R_{ij}^{0\to z} X_j^{\circ} + \sum_{j,k=1}^{5} T_{ijk}^{0\to z} X_j^{\circ} X_k^{\circ} + \text{higher order terms}$$

or

$$\vec{x}_z = R^{0\to z} \vec{X}^{\circ} + \vec{X}^{\circ T} T^{0\to z} \vec{X}^{\circ}$$

Figure 19. EXPLANATION OF SPECTROMETER MOMENTUM CALCULATION

(a) Use of coordinate at target midpoint to determine momentum

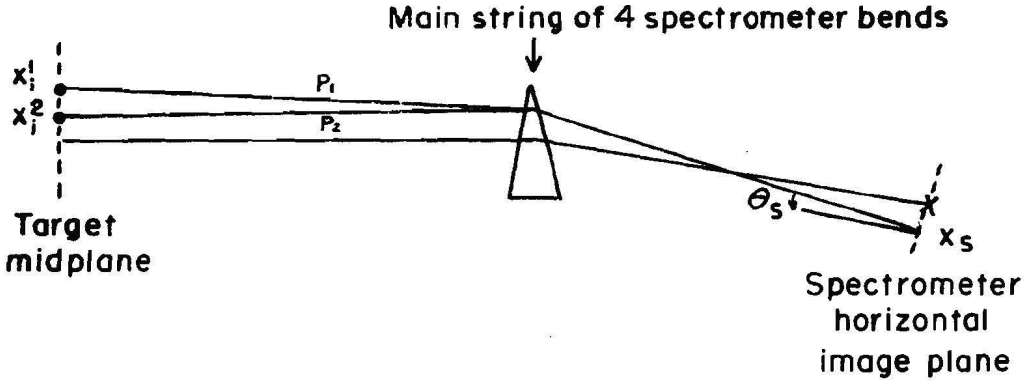

X_s, θ_s are insufficient information to trace the particle back to target midplane unless its momentum is known. If the position of the particle at the target midplane is known, then the momentum of the particle can be determined. Only if it has momentum P_2 can a particle leaving the image plane from X_s with angle θ_s reach X_i^2.

(b) Approximation of scattered particle X coordinate by incident particle X coordinate

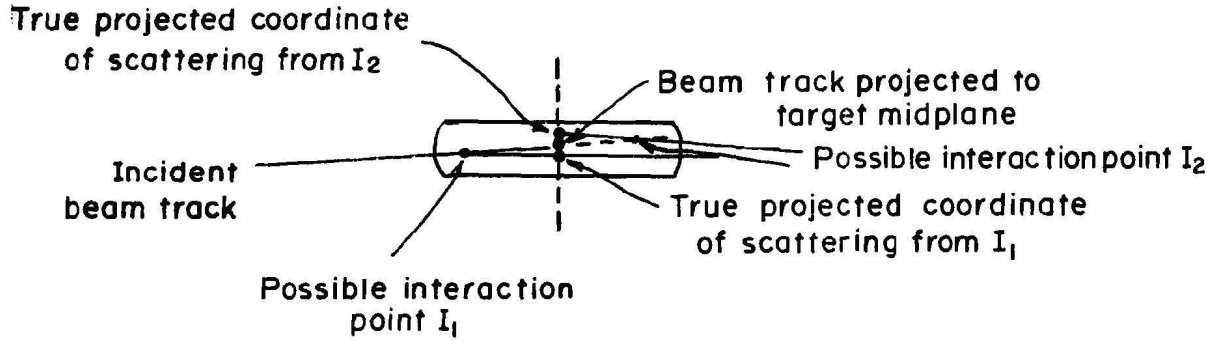

The matrix R and the tensor of third rank T are calculated by TRANSPORT from the field distribution between the target and the location z. The relation can be inverted to give the coordinates at the origin in terms of those at the plane z (correct through the second order):

$$X_i^0 = \sum_{j=1}^{5} (R^{z\to 0})_{ij}\, x_z^j + \sum_{j,k=1}^{5} T^{z\to 0}_{ijk}\, x_z^j\, x_z^k \text{ and higher order terms.}$$

The 'reverse' transformations $R^{z\to 0}$ and $T^{z\to 0}$ are related to the forward transformations as follows:

$$(R^{z\to 0})_{ij} = (R^{0\to z})^{-1}_{ij}$$

where the -1 denotes the usual matrix inverse and

$$(T^{z\to 0})_{ijk} = \sum_{\ell,m=1}^{5} (R^{0\to z})^{-1}_{j\ell} T^{0\to z}_{i\ell m} (R^{0\to z})^{-1}_{km} .$$

Many of the 25 elements of the R matrix are trivial. For example, $R_{5i} = 0$ if $i \neq 5$ and $R_{55} = 1$ follows from the fact that the momentum is a constant of the motion. The symmetry of our spectrometer about the horizontal midplane causes the x and y parts of the matrix to decouple, i.e. $R_{13} = R_{14} = R_{23} = R_{24} = R_{31} = R_{32} = R_{41} = R_{42} = 0$. Since the momentum analysis is in the horizontal plane, $R_{35} = R_{45} = 0$. Figure 20 shows the structure of the simplified matrix.

The non-trivial reverse first order matrix elements for the spectrometer are shown in Table 8a.

First Order Decode.

The matrix equation for tracing a ray back to the target is

Figure 20. STRUCTURE OF THE FIRST ORDER TRANSFER MATRIX. (for a midplane symmetric system of magnets)

$$R = \begin{pmatrix} R_{11} & R_{12} & 0 & 0 & R_{15} \\ R_{21} & R_{22} & 0 & 0 & R_{25} \\ 0 & 0 & R_{33} & R_{34} & 0 \\ 0 & 0 & R_{43} & R_{44} & 0 \\ 0 & 0 & 0 & 0 & 1 \end{pmatrix}$$

$$\begin{Bmatrix} X_i \\ \theta_p \\ Y_p \\ \phi_p \\ \delta_s \end{Bmatrix} = \begin{bmatrix} R^{-1} & 0 & 0 & 0 & R^{-1} \\ R^{-1}_{21} & R^{-1}_{22} & 0 & 0 & R^{-15}_{25} \\ 0 & 0 & R^{-1}_{33} & R^{-1}_{34} & 0 \\ 0 & 0 & R^{-1}_{43} & R^{-1}_{44} & 0 \\ 0 & 0 & 0 & 0 & 1 \end{bmatrix} \begin{Bmatrix} X_s \\ \theta_s \\ Y_s \\ \phi_s \\ \delta_s \end{Bmatrix}$$

where X_i is known from the beam hodoscopes. Then

$$X_i = R^{-1}_{11} X_s + R^{-1}_{15} \delta_s$$

or

$$\delta_s = \frac{X_i - R^{-1}_{11} X_s}{R^{-1}_{15}}$$

After δ_s is determined, the other quantities are obtained by direct matrix multiplication:

$$\theta_p = R^{-1}_{21} X_s + R^{-1}_{22} \theta_s + R^{-1}_{15} \delta_s$$

$$Y_p = R^{-1}_{33} Y_s + R^{-1}_{34} \varphi_s$$

$$\phi_p = R^{-1}_{43} Y_s + R^{-1}_{44} \phi_s$$

The resolution of the spectrometer measurements follows from these quantities

$$\sigma^2(\delta_s) = \frac{\sigma^2(X_i) + (R^{-1}_{11})^2 \sigma^2(X_s)}{(R^{-1}_{15})^2} = \frac{\Delta^2(BX) + (R^{-1}_{11})^2 \Delta^2(H_2)}{12\ (R^{-1}_{15})^2}$$

where $\Delta^2 H_2$ is the wire spacing of the planes at H_2.

$$\sigma\ (\delta_s) = .03\%$$

This does not include the contribution of multiple scattering. Design resolutions which include the effects of multiple scattering are given in Figure 25 in Section IV.

Second Order Decode:

The second and higher order terms can modify the formulae presented above. For this spectrometer, only the second order terms are of any magnitude and even most of these are negligibly small. The principle source of second order contributions are the so-called 'chromatic aberrations.' These terms reflect the fact that the horizontal image plane is at H2 only for particles at the central momentum. Other particles image either upstream or downstream of H2. The significant second order terms are listed in Table 8b. The decode for the momentum is

$$X_i = R_{11}^{z\to 0}\ X_s + R_{16}^{z\to 0}\ \delta_s + T_{126}^{z\to 0}\ \delta_s\theta_s + T_{166}^{z\to 0}\ \delta_s^{\,2}$$

The solution of this quadratic equation is

$$\delta_s = \frac{-(R_{16} + T_{126}\theta_s) + \sqrt{(R_{16} + T_{126}\theta_s)^2 - 4\ T_{166}\ (R_{11}X_s - X_i)}}{2\ T_{166}}$$

where the sign is determined by requiring this solution to reduce to the first order solution for $\theta_s = 0$. Once δ_s is known the other quantities are obtained directly from the reverse transformations.

Although the algorithms above constitute the complete recipe for inverting the spectrometer trajectories, it is profitable to consider the inversion of the trajectory at the focal plane. We have pointed out that at the focal plane production angles are very nearly mapped into lateral positions. The decode, in first order, from the vertical focal plane, f_v, to the target is

$$Y_{f_v} = R_{34}^{0\to f_v}\phi_s \text{ where } R_{34} = 1.03 \text{ cm/mr}$$

and from the horizontal focal plane, f_h, is

$$X_{f_h} = R_{12}^{0\to f_h}\theta_s \text{ where } R_{12} = 2.90 \text{ cm/mr}$$

These are modified slightly by chromatic aberrations, since the focal planes for off-momentum particles really occur at slightly different places.

The hodoscopes SFI and the spectrometer jaw counters are located near the vertical focal plane. The jaw counters can be used as vetoes. A fixed opening ΔY (jaws) corresponds to an angle bite $\Delta\phi_p = \Delta Y \text{ (jaws)}/R_{34}$ and similarly ΔX (jaws) corresponds to $\Delta\theta_p = X_{f_h}/R_{12}$. The hodoscope SFI gives an alternative measurement of the scattering angle ϕ_p which can be compared to the measurement from the wire chambers. The optics at SFI depends only on the first quad triplet set while the wire chambers optics depends on both sets. The comparison checks the integrity of the second quad triplet.

Both the hodoscope and the jaw counters are used in calibration and alignment procedures which are described later.

TABLE 8

Transfer matrix elements from spectrometer horizontal image plane to target midplane

a. First order transfer matrix

Horizontal plane	Vertical plane
$R_{11} = -0.547$	$R_{33} = -0.245$
$R_{12} = 0.0$	$R_{34} = 0.818$
$R_{21} = 0.1625$	$R_{43} = 0.752$
$R_{22} = -1.828$	$R_{44} = -6.60$
$R_{15} = 2.029$	
$R_{25} = 0.692$	

(All other elements are zero except R_{55} which is 1.0.)

b. Second order transfer matrix

$$T_{115} = 1.532 \times 10^{-2}$$
$$T_{125} = -1.476 \times 10^{-1}$$
$$T_{155} = 3.037 \times 10^{-2}$$
$$T_{215} = 4.879 \times 10^{-3}$$
$$T_{225} = -7.34 \times 10^{-3}$$
$$T_{255} = -1.90 \times 10^{-2}$$
$$T_{335} = 1.66 \times 10^{-2}$$
$$T_{345} = -1.68 \times 10^{-1}$$
$$T_{435} = -5.56 \times 10^{-3}$$
$$T_{445} = 8.55 \times 10^{-2}$$

Distributions of decoded quantities are shown in Figure 21. The production momentum distribution shows a sharper elastic peak than the H2 distribution but it is still not very sharp. This is because of the spread in the beam momentum.

Calculation of Kinematic Quantities:

The quantities obtained from the beam and spectrometer decode algorithms described above are measured relative to the central beam and spectrometer settings. Three offsets must be applied to convert these to absolute momenta and scattering angles. Let the central beam momentum setting be P_b^c, the spectrometer momentum setting be P_s^c, and the AVB angle - the angle between the beam and spectrometer axis - be called ϕ_{AVB}.* Then for a given event the beam momentum P_b is

$$P_b = P_b^c(1 + \delta_I/100)$$

the spectrometer momentum P_s is

$$P_s = P_s^c(1 + \delta_s/100)$$

and the scattering angle Φ is

$$\Phi = \{(\phi_p + \phi_{AVB}(P_b) - \phi_I)^2 + (\theta_p - \theta_I)^2\}^{1/2}$$

From these quantities, t and MM^2 can be computed according to equations 1 and 2 of Section II.

---

*The AVB is chromatic so that ϕ_{AVB} is a function of the true beam momentum P_b.

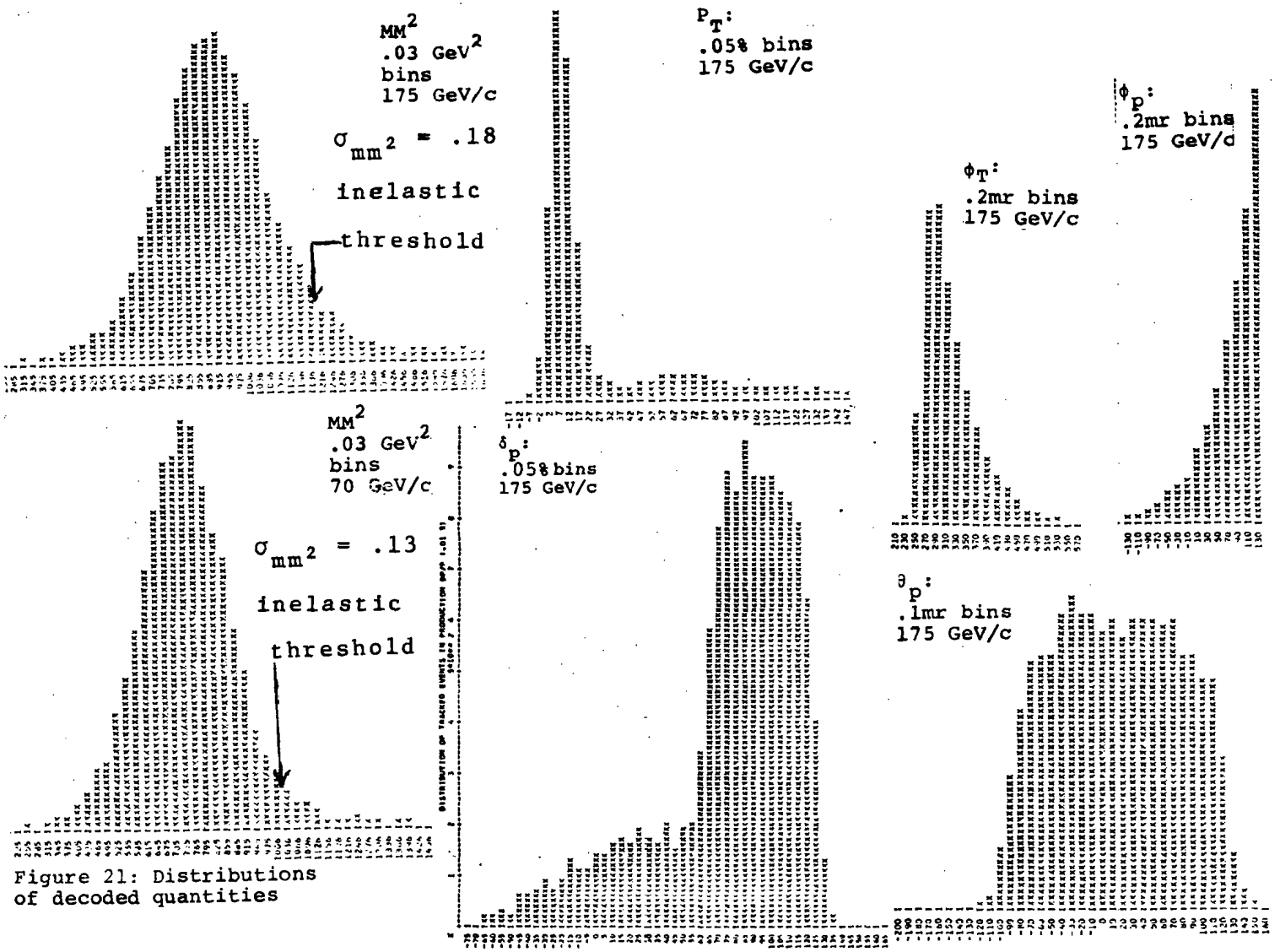

Figure 21: Distributions of decoded quantities

Three additional quantities, the "transfer coordinates" will be used instead of t and MM^2 in the cross section calculation:

$\theta_T \equiv$ "Transfer horizontal angle" $\equiv \theta_p - \theta_I$

$\phi_T \equiv$ "Transfer vertical angle" $\equiv \phi_p + \phi_{AVB} - \phi_I$

$\delta_T \equiv$ "Transfer momentum" $\equiv (P_i - P_s)/P_b$

Distributions of kinematic quantities are shown in Figure 21. The quantity "Transfer momentum" shows a sharp elastic peak. The MM^2 has an even sharper peak. The inelastic cross section appears on the high MM^2 side of the distribution.

E. DATA ACQUISITION HARDWARE

1. Online Computer

Data acquisition was managed by a PDP-11, model 45 computer. The configuration included an RF11/RS11 fast disk, an RK-11 Decpack Disc Cartridge System, a Dectape unit, a TU10 Magtape unit which wrote nine-track tapes at a density of 800BPI, a Versatec line printer, a Decwriter, a card reader, and two display scopes.

The computer acquired data for each event and wrote it onto magnetic tape. In addition to event-by-event information, the computer logged onto tape the contents of scalers and the settings of magnets, pressures, positions, etc. Each event was also analyzed online. Distributions of struck elements were maintained for each detector and could be viewed on display scopes. These distributions were necessary for tuning the beam and spectrometer and monitoring their stability.

Efficiencies for each detector were calculated online. The momentum and angles for each event were reconstructed and sorted into distributions which formed the basis of an online cross-section calculation performed at the end of each run. Scaler ratios and other status and diagnostic information were also available to the experimenter. The online analysis was essential for monitoring the performance of the apparatus and permitted quick detection of problems.

The online computer was capable of completely analyzing and writing to tape approximately 200 events per pulse. These rates were achieved during runs at small t-values. Thus our computer rate limit was 2000 events/minute.

2. Computer Interfaces

Two separate computer interfaces were used to connect the PDP-11 to the rest of the equipment. The first was a "Camac system" which handled all the interfacing except for the MWPC data. The second was a special interface designed specifically to handle data from the MWPCs. These two interfaces are described briefly below.

Camac System

Camac is an international standard for interfacing devices to a digital controller. It is thoroughly documented in the following publications:

> Camac, a modular instrumentation system for data handling AEC # TID-25875
>
> Camac, organization of multi-crate system AEC # TID-25876

A schematic of our Camac system, which used commercially available data buffers, scalers, and ADCs to store analog data from counters, is shown

in Figure 22. Information from hodoscope counters, Cerenkov counters, and from several other sources were strobed into registers whenever an event occurred. These registers were read into the computer over the Camac "dataway" and "branch highway." The actual conversion of standard Camac signals to signals which could be handled by the PDP-11 was performed by an EG & G BD-011 Branch Driver. The BD-011 sent the data directly to the computer memory by DMA (Direct Memory Address) Transfer--a feature of the PDP-11. Since the trigger electronics was gated off as soon as an event occurred, only one data strobe was generated and there could be no accidental superposition of information from more than one event. After the data for an event was completely transferred to the computer, all data registers in the Camac were cleared and the trigger electronics was re-enabled.

The Camac interface was also used to connect several other devices to the computer. Field probe readings, pressure and temperature sensors, magnet shunt voltages, and phototube voltages were all made available to the computer through the Camac system.

Control of the experiment, the starting and stopping of runs, was accomplished by sending electronic pulses to the computer via Camac.

The Wire Chamber Interface:

A specially designed interface transferred data from the wire chambers to the computer.[21] When the fast electronics generated an event trigger, strobe pulses were distributed to all the wire chambers. The pulses on the wires are amplified, reshaped, and delayed by means of a 1.3 μsec one-shot to allow time for the strobe to be received from the fast logic. The strobes then gated the pulses on the wires into 32-bit data registers located on the housing of the chamber electronics.

Figure 22. SCHEMATIC OF CAMAC SYSTEM

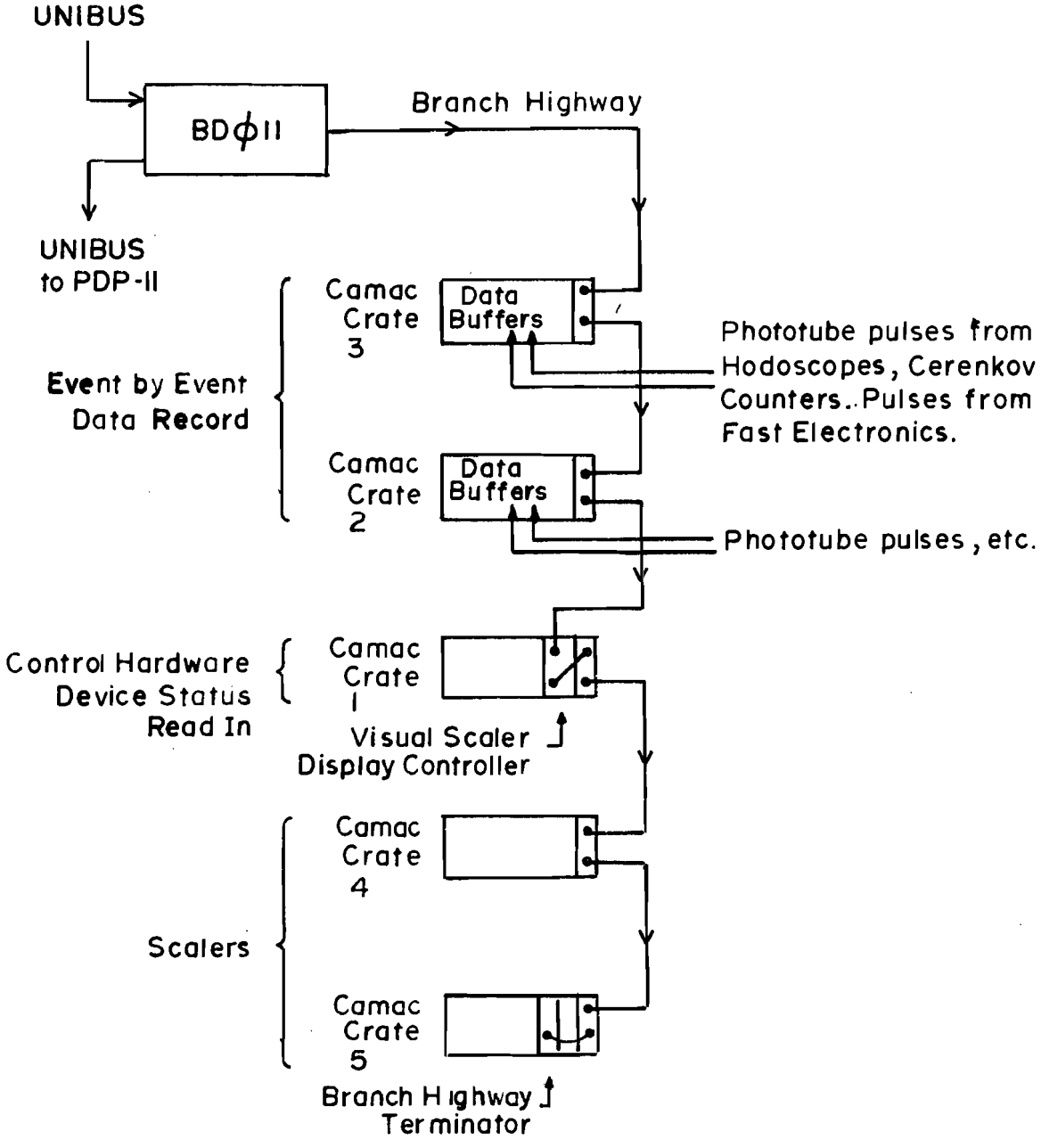

When the computer initiates the read-in cycle, the bits in the registers are moved (one register at a time) into a shift register located in the the Central Interface Unit - CIU - which is located near the PDP-11 and is attached to its unibus. A clock strobe causes the bit string to be shifted. When a 'hit' is detected in the most significant bit, all clocks are inhibited and their values are transferred to the computer via DMA. Thus the scaled clock pulses constitute the address of a struck wire. Since only the addresses of the wires actually struck need to be transferred to the computer, the read-in process is very fast. The clock frequency is 5 mHz. A typical event had only $\sim$ 15 hits out of a total of $\sim$ 800 wires in the MWPC system. Reading of the Camac system and the MWPCs was interleaved.

3. The Gating System

Three different levels of gating were required to guarantee the integrity of the data. These are described briefly here.

"Fast (event) gate" Once an event was received it took approximately 200 μsec to read it into the computer. It was necessary to gate the electronics off so that only one trigger was generated and only one set of strobes was distributed to the various devices. If this had not been done, registers would have filled up with information from several events and their contents would have been meaningless. In addition, flux scalers had to be inhibited so that they counted flux only during the computer live time - that is, while the computer is not reading in data. These inhibitory gates had to be released when the computer finished acquiring the data for an event.

Spill gating: This gate was synchronized to the accelerator cycle and enabled the electronics only during the 800 milliseconds of slow spill.

Glitch remove: This gate inhibited the electronics during portions of the 800 millisecond spill which were unsuitable for data-taking. For example, fast extracted beam was sent to the bubble chambers as frequently as four times during the slow spill. High intensity bursts of beam often accompanied these bubble chamber "pings." Signals are provided to experimenters to mark the time of these occurrences. The glitch remove circuitry received these signals and gated the trigger electronics during the high intensity spikes.

4. Fast Electronics

The primary functions of the fast electronics are i) to generate event triggers based on pulses coming from the trigger counters; ii) to count the beam flux for use in normalizing the observed yields to produce the final cross sections.

Additional functions are i) to provide diagnostic information on the performance of Cerenkov counters, trigger counters, and the stability of the apparatus in general ii) to provide the means for making calibration and background studies which were necessary for getting final cross sections.

Beam Event Triggers and Spectrometer Event Triggers

One arm of the fast electronics processes the beam trigger counter pulses and produces a beam coincidence 'BT' if all requirements are satisfied. Another arm processes the spectrometer trigger counter pulses and produces a spectrometer coincidence 'ST' if all the requirements are satisfied. Two separate triggers are developed from these

two signals. A spectrometer event is defined as the coincidence BT•ST. These events are candidates for scattering events. The second trigger occurs on a sample of events which make beam coincidences BT but not spectrometer coincidences. That is, it occurs on the condition BT·$\overline{ST}$. This results in the recording on tape, interspersed with scattering events, of a sample of beam which is unbiased by the requirement of scattering into the spectrometer. The use of these events in the cross-section calculation is discussed below. An electronic countdown circuit allows the experimenter to adjust the sampling rate. Typically, the beam events are counted down so that they occur at approximately the same rate as spectrometer events.

Simultaneous Measurement of Several Reactions:

The M6 beam contains mainly π's, K's, and nucleons. Since the spectrometer trigger is manufactured only from trigger counters and makes no selection based on Cerenkov signals, the reactions

1) $\pi + P \rightarrow \pi +$ anything

2) $K + P \rightarrow K +$ anything

3) $N + P \rightarrow N +$ anything $\qquad (N = P, \overline{P})$

are recorded together with reactions like

4) $\pi + P \rightarrow K +$ anything .

In principle, nine reactions are measured on each polarity of the beam. In practice, most of these reactions do not occur when the spectrometer momentum is set for elastic scattering.

Beam Particle Countdown:

The composition of the M6 Beam is determined by the dynamics of the interaction between the 300 GeV/c incident protons and the nuclei of the production target. At 50 GeV/c, about 80% of the beam was π^+ and there were only a few percent K^+. At 175 GeV/c, about 90% of the beam was protons. The experimenter would probably prefer nearly equal numbers of the three particles. In runs where the event rate is low (less than $\sim$ 200 events/pulse) so that the computer can record nearly every scattering event, the experimenter cannot improve his situation, However, at kinematic settings where the event rate is so high that events are coming in faster than the computer can handle them ("computer limited"), the experimenter can electronically suppress triggers on the majority (most abundant) particle flux and essentially restructure the beam composition. This is accomplished by special countdown or suppression circuits which allow only every 2^nth particle of a given type to make a trigger. "n" is selected by means of a switch on the front panel of the circuit. The countdown circuitry was used at small angles to count down π^+, π^-, or protons.

Figure 23a is a block diagram that gives an overview of the fast logic. Figure 23b shows the basic beam logic including the beam countdown. Figure 23c shows the spectrometer logic.

The switching between various logic configurations was facilitated by the front panel programming capabilities of the LeCroy Logic Units (364, 365 Logic units) which were used in the electronics.

Figure 23: Fast Electronics

a. Overview

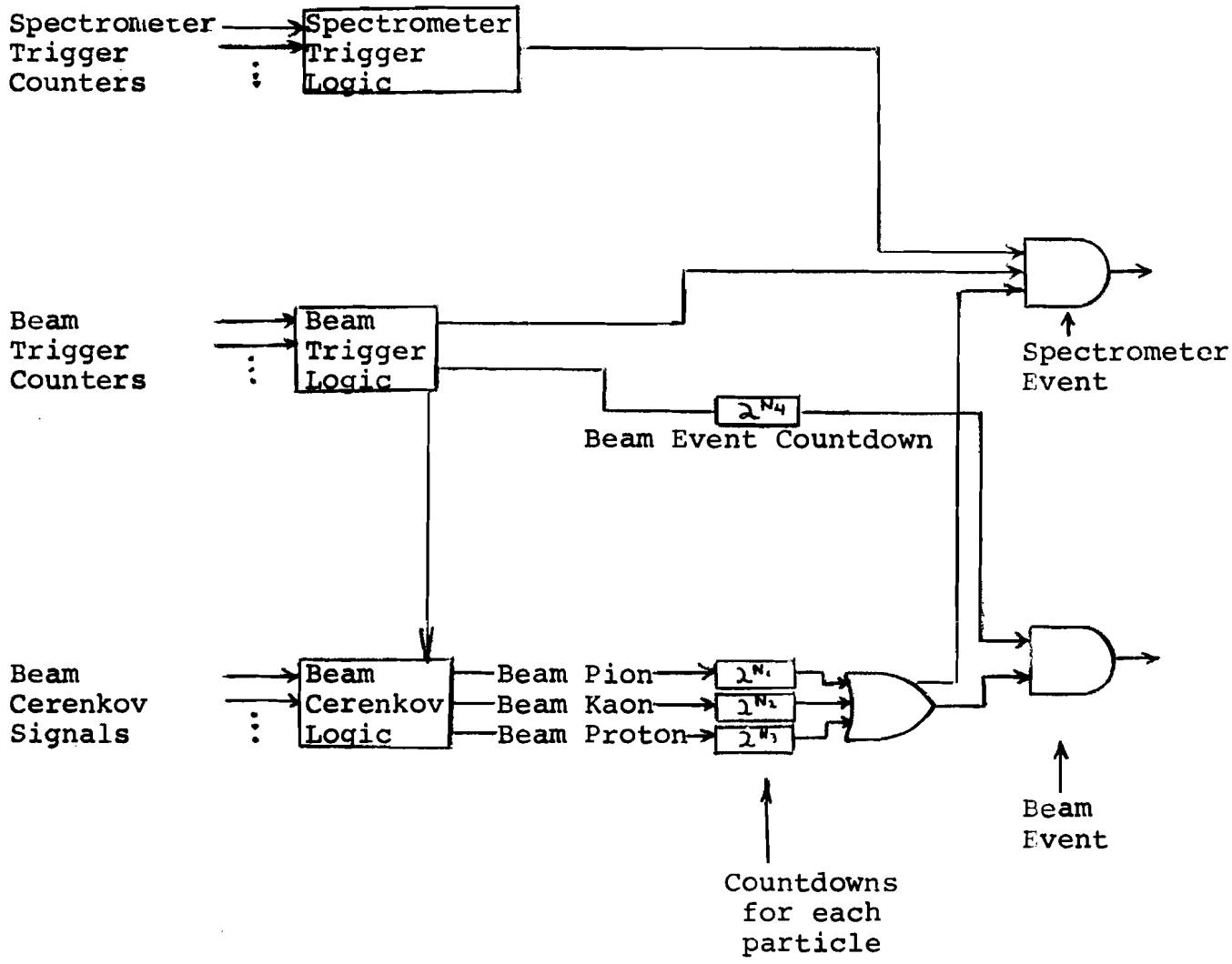

LEGEND:

'OR' Circuit

Coincidence circuit

Fan-out

Fan-in

321B	Quad Updating Discriminator (LeCroy)
T121	Quad Updating Discriminator (EG&G)
164	Dual Discriminator (Chronetics)
158	Pulse Fanout (Chronetics)
365	Logic Unit (LeCroy)
364	Logic Unit (LeCroy)
G →	Input to EG&G C121. 'Fast Kill' gate is applied to the strobe input

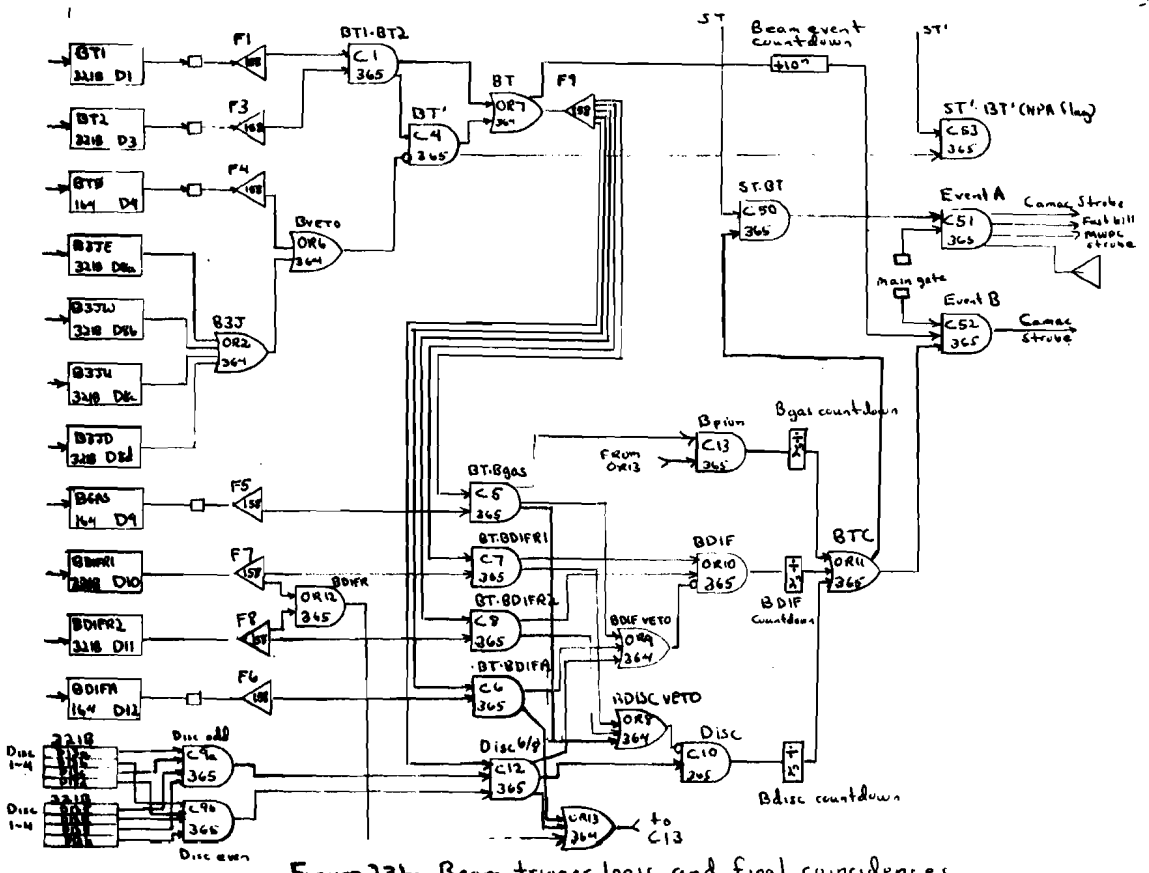

Figure 23b: Beam trigger logic and final coincidences

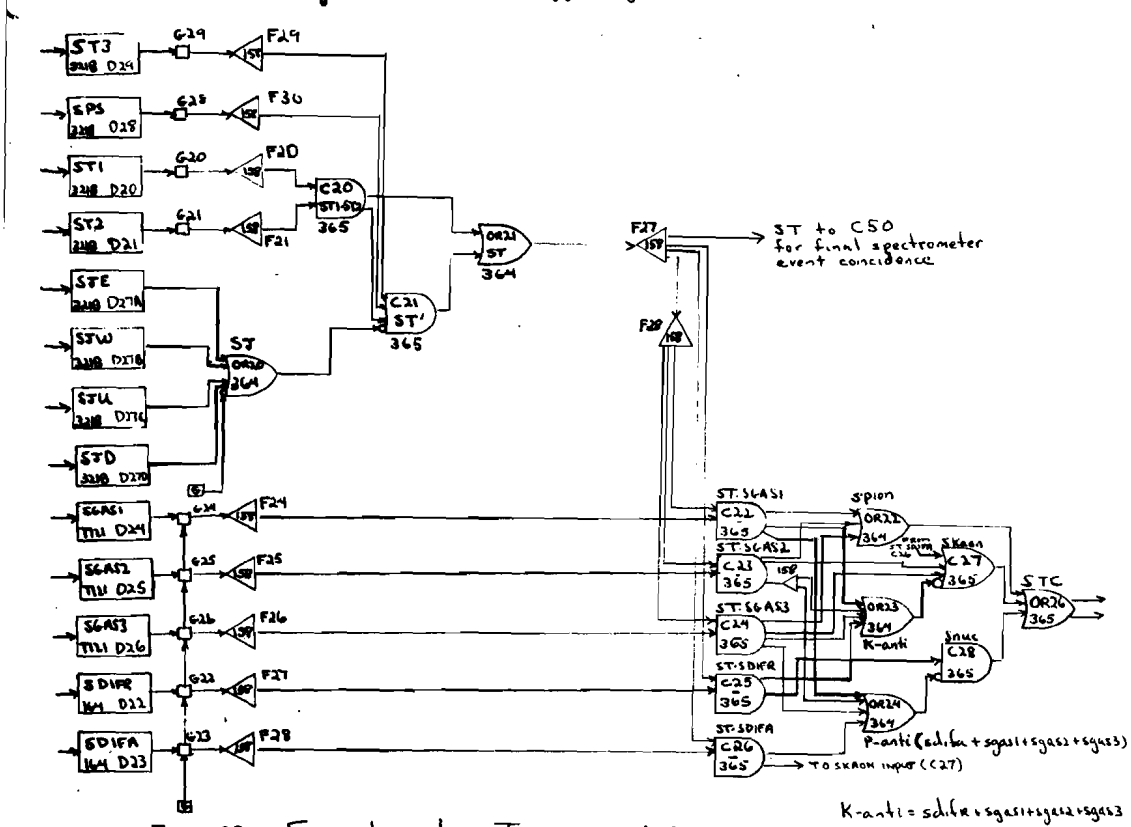

Figure 23c: Spectrometer Trigger and Cerenkov Logic

F. Target System

The following targets were available for this series of experiments:

Content	Length
Hydrogen	20"
Hydrogen	10"
Dummy (empty)	20"
Dummy (empty)	10"
Deuterium	20"
Deuterium	10"

All the target cells were 1" diameter mylar tubes with hemispherical endcaps. The wall thickness was 7-1/2 mils. The dummy cells were identical to the other cells but were evacuated. All six cells were housed in a single aluminum "scattering chamber," which was under vacuum. This chamber had mylar entrance and exit windows before and after each cell. Superinsulation was wrapped around each cell.

The lengths of the cells were known to $\sim$ .1% by surveying them when they were cold and pressurized.

The liquid hydrogen was produced and maintained by a closed-loop refrigeration system which used cold helium gas as the refrigerant. A small quantity of hydrogen gas was introduced into the target and came into contact with an aluminum plate that was cooled by the helium. The hydrogen condensed and accumulated in the target cell until it overflowed into a reservoir that sat on top of the target assembly. Two carbon resistors in the reservoir were used to indicate that the target was full. In normal operation, the liquid hydrogen was at atmospheric pressure. A vapor pressure gauge monitored the

target density.

During the experiment, target operation was stable. No boiling or icing was observed. The pipes between the reservoir and the target cell were inclined at 5° to the horizontal so that the cells would stay full as they were tilted to track the scattering angle.

The target assembly could be moved remotely from the counting house to position the desired target on the beam line. Target scans verified the alignment of the cells with the beam. Since the cells are much bigger than the beam spot, the alignment is not critical.

CHAPTER IV

PERFORMANCE AND CALIBRATION OF THE APPARATUS

This section contains a discussion of the tuning and calibration of the apparatus. Several months were required to bring the apparatus to the point where it performed reproducibly and reliably. The material selected for this section describes briefly only those parts of the effort which bear most directly on the measurement of elastic cross sections and the understanding of the possible systematic errors in the experiment.

A. DETERMINATION OF SPECTROMETER PROPERTIES

1. Transfer Matrix

The Transport model of the spectrometer predicts the transfer matrix between any two points. We are particularly interested in the transfer matrix between the target midplane and the spectrometer's horizontal image plane. The predicted matrix will be applicable to the spectrometer only if certain conditions are satisfied. Some of these conditions are 1) accurate placement and alignment of all magnets; 2) accurate knowledge of the excitation functions - $\int g d\ell$ (where g is the field gradient) and $\int B d\ell$ vs current for all quadrupoles and dipoles; 3) high field quality (small higher order multipole terms) in the magnets; 4) high stability and accurate calibration of the power supplies.

Many studies were carried out to determine the transfer matrix. The conclusion of these studies was that the transfer matrix of the model spectrometer was a good approximation to the transfer matrix of

the true spectrometer.

The key factor in all these studies was the ability to bring the M6 beam directly into the spectrometer (recall that the spectrometer is at 0° with respect to the beam). All properties of the beam particle at the entrance to the spectrometer have already been measured by beam hodoscopes. By following the trajectories of these fully tagged particles through the spectrometer, one could determine the transfer matrix. For example, the most general linear relation one can write between some (one of x_i, y_i, θ_i, or ϕ_i) incident coordinate ξ_k and the spectrometer quantities (x_s, y_s, θ_s, ϕ_s and $\delta_s = \delta_i$) $\vec{X}^s$ is

$$\xi_k = \sum_{i=1}^{6} \alpha_i X_i^s$$

(we take $X_6^s = 1$ so that α_6 is an offset). Since for each event all the ξ_k's and X_i^s's are measured, it takes only a few events to determine a set of α_i. The 'best values' of α_i are determined from a run of many (N) events by minimizing the quantity

$$\chi^2 = \sum_{j=1}^{N} \{\xi_k^j - \sum_{i=1}^{6} \alpha_i X_i^{sj}\}^2$$

where j denotes the sum over all the events. The set of best values $\{\alpha_i\}$ is the transfer matrix. The extension of this procedure to determining second order matrix elements is straightforward. The fitting procedure can also retrieve the relative calibration of the beam momentum hodoscope and the spectrometer momentum measurement. It is necessary to perform these fits under a variety of conditions - .e.g. broad illumination of the spectrometer or narrow illumination of specific

regions - in order to look for variations of the transfer matrix in different parts of the aperture. The transfer matrices determined in this way agreed with the values predicted by Transport to within a few percent. There were, however, small time dependent instabilities and variations in these coefficients. These were traced to power supply regulation and stability problems. Under these circumstances, the available evidence indicated that the model transfer matrix gave an adequate representation of the magnetic properties of the spectrometer. That matrix (Table 8) was used throughout the data analysis.

In a second less formal approach, specific transfer matrix elements were measured on-line by using the verniers and the AVB to direct pencil beams with specific initial conditions into the spectrometer. An example of such a measurement was a quick procedure to check the vertical focus. If the spectrometer was in focus, changing the angle of the beam entering it should produce no motion of the spot at the MWPC V4 located at the vertical image plane. The AVB was used to change the angle of the beam at the target without changing its position there. $\Delta Y(V4)$, the shift in position at V4, gives a direct measure of $R_{34}^{0\rightarrow V4} = \Delta Y(V4)/\Delta\phi_{AVB}$. When the spectrometer was correctly focused, the spot did not move so that $R_{34}^{0\rightarrow V4} = 0$.

The most crucial of these studies was the determination of the transfer matrix at the spectrometer focal plane in the parallel region. This measurement provided an independent check on the solid angle calibration of the spectrometer and was used in determining the absolute normalization of the data.

The spectrometer jaw counters were set to a fixed vertical opening ΔY (usually 2.54 cm). Collimators were closed to form a pencil beam. The AVB was powered until the beam had been deflected so that half of it was on the upper jaw. The position of the beam was monitored by the ratio $R = (ST1 \cdot ST2 \cdot \overline{Sjaws} \cdot BT)/(ST1 \cdot ST2\ BT)$ (see Figure 24a; BT means that a beam trigger was required). When R = 50%, the beam was half-way onto the jaw. Let I_1 be the current that produces this deflection. Then the AVB current was changed to swing the beam onto the lower jaw. Let I_2 be the current required to center the beam on the lower jaw (R = 50%). If α is the AVB coefficient in milliradians of deflection per amp (at the known beam momentum), then the transfer matrix element R_{34} is given by

$$R_{34}(\text{vertical focal plane}) = \Delta Y/|I_1 - I_2|\alpha$$

There is no magnet which allows one to swing the beam through a large angle in the horizontal plane, so R_{12} cannot be determined in exactly the same way. Instead the matrix element R_{12} is determined by reversing the polarity of the front quad triplet. This interchanges the horizontal and vertical properties, so that the vertical plane now has the properties that used to belong to the horizontal plane. Repetition of the procedure measures R_{12} (horizontal focal plane). Figure 24b shows the results of one of the calibrations. This study was performed at each energy and agreed with Transport typically to $\sim$ 3%.

Figure 24: Calibration of Spectrometer Solid Angle
a. Set-up

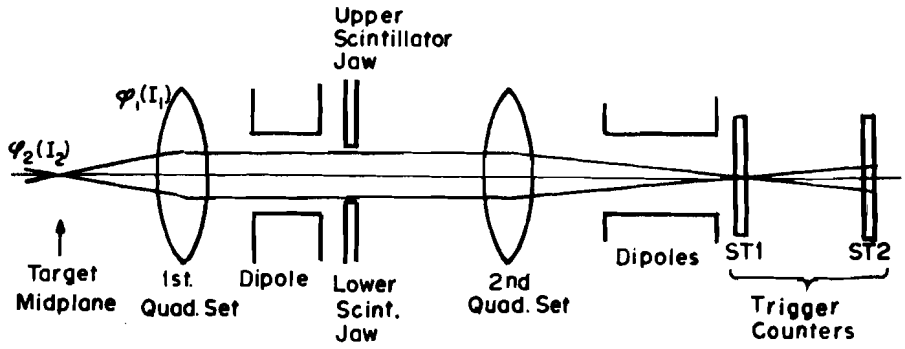

$$\text{'Transmission'} = R = \frac{ST1 \cdot ST2 \cdot \overline{SJ} \cdot BT}{ST1 \cdot ST2 \cdot BT}$$

b. Calibration of the vertical angle scale (70 GeV/c)

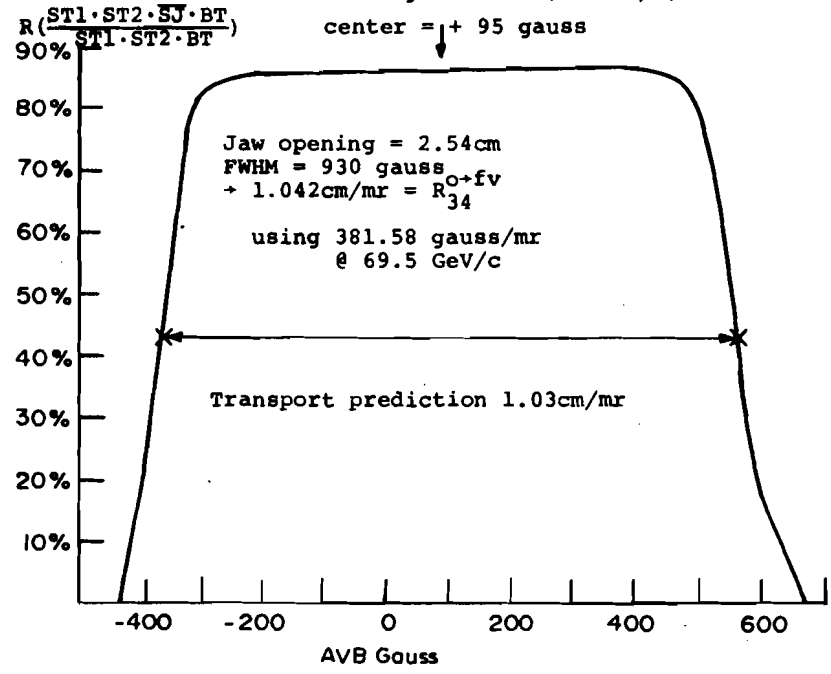

2. Resolution in t and MM^2

The design resolution of the spectrometer-beam system is determined by three factors:

a) the magnifications and momentum dispersions at the various MWPCs.

b) the granularity (wire spacing, hodoscope size) of the detectors in the beam and the spectrometer which do the tracking.

c) multiple scattering of the particles in the material in the beam and spectrometer and in the hydrogen target.

A full calculation of the predicted resolutions, including the effects of multiple scattering, has been carried out[22] and is shown in Figure 25 together with the resolutions achieved during our experiment. It is apparent that the MM^2 resolution actually achieved is 20% to 50% worse than the predictions. We have attributed this to the power supply regulation problems we encountered.

3. Acceptance

Determining the acceptance of the spectrometer is complicated by the fact that the angular acceptance is only about ten times greater than the angular resolution. We have, therefore, concentrated on determining only a suitable uniform acceptance region rather than the total acceptance function. By uniform acceptance, we mean a region defined by

$$
\begin{aligned}
|x_p| &\leq \Delta x/2 \\
|\theta_p| &\leq \Delta\theta/2 \\
|y_p| &\leq \Delta y/2 \\
|\phi_p| &\leq \Delta\phi/2 \\
|\delta_s| &\leq \Delta\delta/2
\end{aligned}
$$

such that all particles whose initial coordinates (x_p, θ_p, y_p, ϕ_p, δ_s) at the target midplane lie within this region will transmit through the spectrometer.

The uniform acceptance region has been determined in three separate ways:

1) by an analytic calculation using a simple model of the spectrometer apertures.

2) by probing the spectrometer with various pencil beams of particles to find the edges of the aperture.

3) by varying the cuts in the off-line analysis to see if they change the cross sections.

Each method has its strengths and weaknesses. Method 2, for example, requires beam time to study the transmission of the large numbers of different initial rays that can occur. It is also hindered by the inability to create all of interesting initial conditions with the available verniers and the AVB. In particular, one only has limited ability to swing the beam in the horizontal plane. From Method 2, we have gotten good measurements of the vertical angle acceptance (using the AVB) as a function of the vertical position at the target (using the vernier V12). By changing the relative momentum of the beam and the spectrometer, we have determined the momentum acceptance. Method 3 is very powerful but time-consuming. This method has been especially useful in determining the horizontal angle acceptance since the scattered flux has a nearly flat distribution in horizontal angle. The horizontal position acceptance is also very easy to check. Method 1 is the riskiest method because it required some approximations and deals with an idealization (model) of the spectrometer. It has the advantage of presenting a complete picture all at once. This method is described in Appendix 3. It should be remarked that all three

Figure 25. Total Resolution $\sigma(MM^2)$ at $t = 0.1\ (GeV/c)^2$

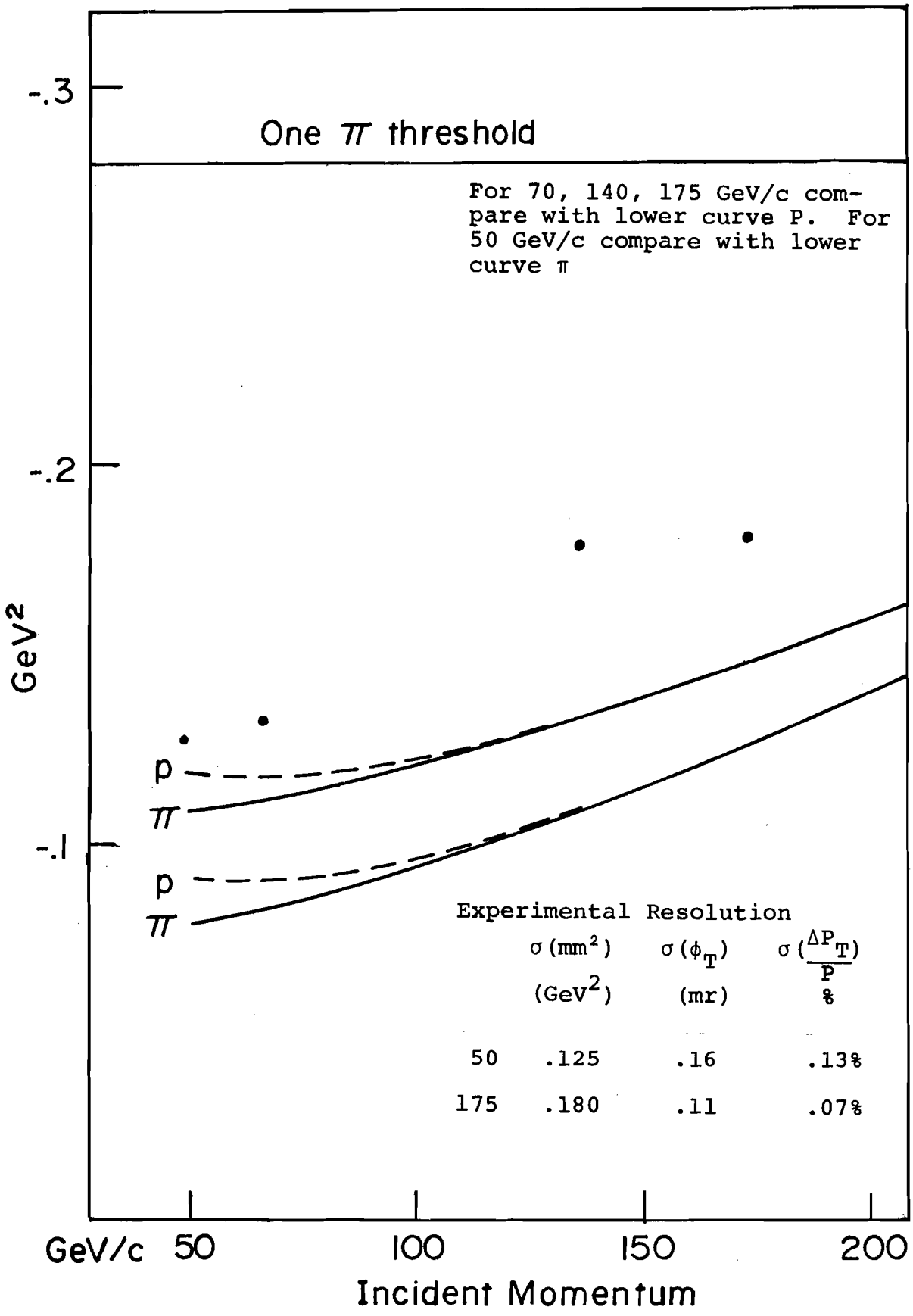

methods give similar answers on the uniform acceptance region. Method 3 is the final arbiter of any slight disagreements.

The uniform acceptance region used in the analysis was:

$$|\theta_p| \leq .75 \text{ mr}$$
$$|\phi_p| \leq 1.4 \text{ mr}$$
$$|\delta_p| \leq 1.75 \%$$
$$|x_p| \leq 8 \text{ mm}$$
$$|y_p| \leq 5\tfrac{1}{2} \text{ mm}$$

The trade-off between y_p acceptance and ϕ_p acceptance was tilted in favor of y_p in order to guarantee that the whole target is seen at large scattering angles.

B. CALIBRATION OF THE t-SCALE

The t-scale is calculated from the known magnetic properties of the AVB system. The integrated magnetic field strength - $\int Bd\ell$ - for each magnet was determined by mapping the field inside the magnet at 2" intervals with an NMR probe. The fringe fields were mapped with a Rawson-Lush rotating coil at 2 cm intervals. The fringe field mapping was done both with and without the mirror plates which were attached to the magnets to keep the fringe fields away from nearby phototubes. The total $\int Bd\ell$ for each magnet was determined by these means to $\sim$ .1 % Each magnet had its field carefully calibrated against the field in the 3' dummy magnet which was connected in series with the 3 AVB magnets. This was important because we actually set the field by means of a Rawson-Lush rotating coil located in the dummy magnet. The calibration against the dummy magnet was known to a few hundredths of a percent. We have attached an uncertainty of $\sim$ .5% to our knowledge of the t-scales based

on our knowledge of the AVB integrated field strength.

C. ALIGNMENT OF THE BEAM AND SPECTROMETER

The beam hodoscopes will correctly measure angles with respect to the beam axis only if the beam is accurately centered on them. Similarly, the spectrometer MWPC's must be centered on the spectrometer axis. Finally, the beam and spectrometer axes must make an angle of 0°. The beam vernier magnets and the AVB were used to effect the alignment. It was learned early in the experiment that the spectrometer was inclined upward with respect to the beam at an angle of $\sim$ .2 mr. A small current was set in the AVB to send the beam through the spectrometer along the true axis. This current was called the "AVB offset" and scaled well with energy (verifying the fixed angle offset). The AVB current settings for a given angle had this offset added in.

This experiment was virtually immune to small horizontal misalignments ($\lesssim$ .1 mr) in angle between the beam and spectrometer but quite sensitive to vertical misalignments. This can be seen from the fact that

$$t \sim P_b^2\{(\phi_{AVB} + \phi_P - \phi_I)^2 + (\theta_p - \theta_I)^2\}$$

and $\left.\frac{d\sigma}{dt}\right|_{e\ell} \sim A\, e^{bt}$ where b is a number between 11 and 8, typically. An error in t of Δt causes a fractional error in the cross section of $b\Delta t$ for small Δt. An error in the horizontal angle of Δ_θ causes an average error in t of

$$\overline{\Delta t} = P_b^2\, \Delta_\theta^2 + 2\, P_b^2\, \overline{\theta}_p\, \Delta_\theta - 2\, P_b^2\, \overline{\theta}_i\, \Delta_\theta$$

Since $\overline{\theta}_s$, $\overline{\theta}_b$ < .1 mr, for Δ_θ < .1 mr,

$$\overline{\Delta t} << .001$$

and the cross section error is always less than 1%. An error in the vertical angle of Δ_ϕ causes an error in t whose leading term is

$$\Delta t \sim 2\ P_b^{\,2}\ \phi_{AVB}\ \Delta_\phi$$

At 175 GeV/c, a misalignment Δ_ϕ = .02 mr at ϕ_{AVB} = 5 mr causes an error

$$\overline{\Delta t} \sim .006$$

For protons, b is about eight in this region so that there would be a 5% error in the cross section.

It would have been difficult to maintain the vertical alignment to .01-.02 mr. We used the following procedure to desensitize ourselves to vertical misalignments. First we steered the beam down onto the target ('AVB +') from above and measured a cross section. Then we steered the beam up onto the target from below ('AVB -') and measured a cross section. The two runs were then averaged together as two systematically different measurements (that is, they were weighted equally and not according to their statistical weights). If there was an offset Δ_ϕ, then for AVB+, instead of scattering at $t = P^2\ \phi_{AVB}^2$, we were actually scattering at

$$t_+ = P^2(\phi_{AVB} + \Delta_\phi)^2$$

so that

$$\left.\frac{d\sigma}{dt}\right|_{+} = A\, e^{bp^2(\phi_{AVB} + \Delta_\phi)^2} \sim A\, e^{bp^2\phi^2_{AVB}}\,(1 + 2\, bp^2\phi_{AVB}\Delta_\phi)$$

For AVB-,

$$t_- = p^2(\phi_{AVB} - \Delta_\phi)^2$$

so that

$$\left.\frac{d\sigma}{dt}\right|_{-} = A\, e^{bp^2(\phi_{AVB} - \Delta_\phi)^2} \sim A\, e^{bp^2\phi^2_{AVB}}\,(1 - 2\, bp^2\phi_{AVB}\Delta_\phi)$$

A direct average

$$\overline{\frac{d\sigma}{dt}} = \frac{\left.\frac{d\sigma}{dt}\right|_{+} + \left.\frac{d\sigma}{dt}\right|_{-}}{2} = A\, e^{bp^2\phi^2_{AVB}} = \frac{d\sigma}{dt}\,(t = p^2\phi^2_{AVB})$$

gives the correct cross section at the nominal t value of $p^2\phi^2_{AVB}$ to first order in Δ_ϕ. The validity of this procedure does not depend on the functional form of the cross section. It only requires that the error Δ_ϕ be sufficiently small that the second order contributions in the Taylor series expansion of the cross section in Δ_ϕ are negligible.

If the offset Δ_ϕ is larger, one can perform a logarithmic averaging

$$\ell n \left.\frac{d\sigma}{dt}\right|_{+} = \ell n\, A + bp^2(\phi^2_{AVB} + \Delta_\phi{}^2 + 2\,\phi_{AVB}\,\Delta_\phi)$$

and

$$\ell n \left.\frac{d\sigma}{dt}\right|_{-} = \ell n\, A + bp^2\, (\phi_{AVB}^2 + \Delta_\phi{}^2 - 2\, \phi_{AVB}\, \Delta_\phi)$$

then

$$e^{1/2(\ell n \left.\frac{d\sigma}{dt}\right|_{+} + \ell n \left.\frac{d\sigma}{dt}\right|_{-})} = A\, e^{bp^2(\phi_{AVB})^2}\, e^{bp^2\Delta^2\phi}$$

$$= \frac{d\sigma}{dt}\,(t = p^2\phi_{AVB}{}^2)\ x\ e^{bp^2\Delta^2\phi}$$

The remaining error $e^{bp^2\Delta_\phi{}^2}$ is never more than .2% and is usually ignored. The logarithmic average obviously reduces to the linear average for small Δ_ϕ. The linear and logarithmic average gave the same results to hundredths of a percent a 50 and 70 GeV/c. At 140 GeV/c and 175 GeV/c, Δ_ϕ was sufficiently large that it was necessary to use the logarithmic average.

The averaging of the AVB+ and AVB- cross sections removes the effect of any average misalignment between beam and spectrometer. See Figure 26b. Steering shifts in the beam due to drifts in magnets are directly measured by By and Bϕ hodoscopes. Even an error in the position of the By or Bϕ hodoscope with respect to the beam is averaged out by the AVB+, AVB- procedure (26c). The alternation of AVB+ and AVB- scattering is the key to making good measurements with the spectrometer.

Figure 26. Elimination of Vertical Angle Alignment Problems by Averaging AVB + and AVB - Cross Sections

(a) Perfect alignment

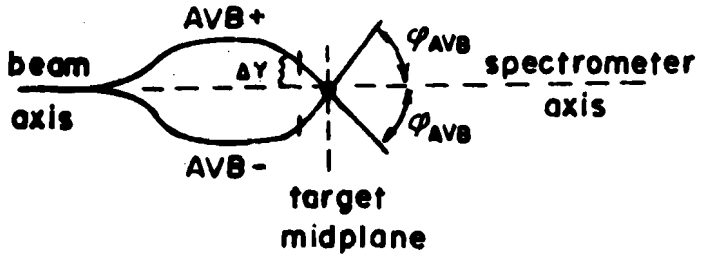

1) Spectrometer axis is at zero degrees with respect to the beam axis upstream of the AVB.

2) When the hodoscope is set 127 mils x ϕ_{AVB} = ΔY from its 0^{o} position, the beam is exactly centered on the hodoscope.

(b) Angular misalignment

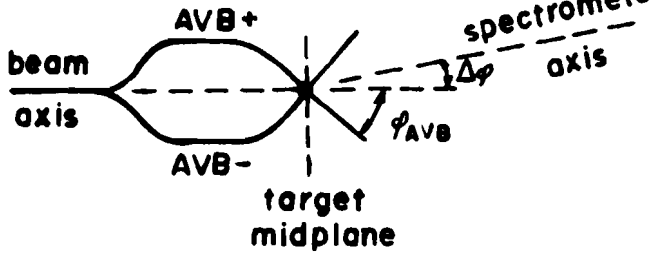

Spectrometer axis and beam axis are misaligned by $\Delta\phi$. For AVB + run, scattering angle is ϕ_{AVB} + $\Delta\phi$. For AVB - run, scattering angle is ϕ_{AVB} - $\Delta\phi$. Average of two runs gives correct cross section at ϕ_{AVB}.

(c) Mispositioning of beam on Y-hodoscope

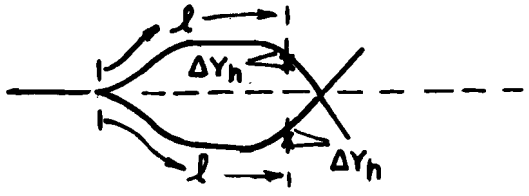

Central beam axis goes through Y-hodoscope at $+\Delta Y_h$ on AVB+. Apparent angle offset is $+\Delta Y_h/\ell$.

Central axis goes through Y - hodoscope at $-\Delta Y_h$ on AVB -.

Apparent angle offset is $-\Delta Y_h/\ell$.

The average of the two cross sections cancels out the error. This is only true if the hodoscope is moved the correct amount between AVB + and AVB -.

D. MOMENTUM MATCHING OF BEAM AND SPECTROMETER

The magnetic length of the main ring dipole magnets used in the beam and spectrometer was known only to a few tenths of a percent. This means that from field strengths alone the absolute momentum of the beam is known only to $\sim$ 1%. This is not critical because the elastic cross sections are changing very slowly with energy. It is important, however, to match the beam and spectrometer momentum. This is done by centering the beam at the target and narrowing its momentum acceptance by nearly closing the collimator C3. The fields in the bend magnets of the spectrometer are varied until the beam spot is centered on the wire plane H2 at the horizontal image plane. Once the spectrometer is calibrated in this manner to the beam, the MM^2 peak will show up at $M_p^2 = .88$. In fact, if the spectrometer is slightly misset with respect to the beam, the calibration can be recovered by finding the center of the observed elastic peak at MM^2_{obs}. Then the momentum offset Δ_p is

$$\Delta_p = \frac{MM^2_{obs} - M_p^2}{2 M_p}$$

Thus, it is not even necessary to precisely match the two momenta. The elastic peak calibrates the relative momentum scale. A miscalibration of the relative momentum scale also produces a slight error in the t-scale, which can again be repaired by calibrating against the peak to learn the true spectrometer momentum setting.

The momentum-settings of the beam and spectrometer were monitored continuously by field probes (Rawson-Lush rotating coil probes) located in 3' dummy magnets. One dummy magnet is in series with the

beam bend magnets. The other dummy magnet is in series with the spectrometer bend magnet.

E. ABSOLUTE MOMENTUM CALIBRATION

The absolute t-scale of this experiment did not depend on knowing precisely the absolute beam momentum. As noted, the AVB really sets $P\theta$ so a given excitation current sets the same t values regardless of momentum. In the calculation of the cross section it is necessary to know the correspondence between t and angle - that is, the absolute incident momentum - to calculate the Jacobian between $d\sigma/d\Omega$ and $d\sigma/dt$. This experiment had the unique ability to make an absolute momentum calibration of the beam. The feature that made this possible was the laser interferometer which measured the absolute index of refraction of the gas in the Disc Cerenkov counter. (Usually the pressure of the radiator is measured. This is related to the index of refraction by the elasticity of the gas which is not a very well known quantity.) The mass difference between the pion and proton is known very precisely. The index of refraction of the counter is set so that the pion light is centered in the Disc annulus. The index of refraction is now varied (additional helium is admitted) until the proton light is in the annulus. The number of fringes Δf detected by a photocell in the interferometer measures the absolute change in index of refraction. Δf is related to the central momentum P_b^c by

$$\Delta f = 1.667 \times 10^7 \frac{M_p^2 - M_\pi^2}{P_b^{c2}}$$

Since it is possible to locate the centers of the pion and proton peaks to within a few fringes and the difference between the peaks is a few thousand fringes this method is accurate to $\sim$.2%.

It should be noted that the measurement of the Transport coefficients at the focal plane requires one to calculate the angle from the AVB current. The absolute beam momentum must be known to do this correctly.

Typically, the Disc calibration agreed with the nominal beam calibration to within 1%. We always relied on the Disc value.

CHAPTER V

DATA-TAKING

The basic data taking cycle was

1) empty target-AVB+
2) full target-AVB+
3) full target-AVB-
4) empty target-AVB-

We usually restricted the length of runs so that a full four run cycle took between an hour and a half and two hours. At most kinematic settings, several of these four-run cycles were needed to acquire the desired statistics.

A computer-generated run plan contained a list of all the AVB and spectrometer settings required to cover the t and MM^2 intervals of interest. It provided a list of all the Cerenkov counter settings, the AVB currents for each angle, the position of the By hodoscope, etc. Estimates of the running time based on anticipated beam flux and extrapolations of cross sections from lower energies were also computed.

The spectrometer momentum acceptance is so large that a single spectrometer setting contained the elastic peak and the inelastic spectrum out past the resonance region ($MM^2 \gtrsim 4$ GeV^2). The spectrometer magnets did not have to be changed at all during the elastic scattering measurement. Only the AVB field had to be changed to vary the scattering angle.

The main differences in running conditions among the energies reported here were

1) The number of angle settings (AVB settings) required to span the t interval out to $\sim -.7$ GeV^2.
2) The maximum scattering angle (which was associated with the problem of vertical height acceptance).
3) The minimum scattering angle needed to reach small t at high energies.
4) The total rate and composition of the beam
5) Efficiencies of Cerenkov counters.

Points 1 and 2 are related. The t-bite of the spectrometer is approximately

$$\Delta t \sim 2\, p_b^2\, \phi_{AVB}\, \Delta\phi_{acc}$$

where $\Delta\phi_{acc}$ is the size of the uniform acceptance in vertical angle. The spectrometer has a small t-bite at 50 GeV and several AVB settings are required to span the t interval. At 175 GeV/c, the t-bite is so large that the AVB setting at 4 mr covers the t interval from -.2 to -.9. The maximum scattering angle is related to the maximum t value by

$$\phi_{max} \sim \sqrt{\frac{-t_{max}}{p_b^2}} \quad .$$

At 50 GeV/c we had to go to angles of $\sim$ 16.5 mr. As discussed above, we started to worry about the vertical height acceptance. We therefore added to our basic run cycle four additional runs (full, MT, AVB+,

AVB-) on 10" targets. Just enough data was taken on the 10" target to get a cross section for the majority particle (most abundant particle in the beam) which was π^+. This was compared with data on the 20" target. The conclusion was that the whole 20" target was in view out to at least 16 mr. Table 10a lists all the kinematic settings.

At high energies (140, 175 GeV/c), it was difficult to get down to small t. At 175 GeV/c, $-t = .05$ implies working within 1.3 mr of the beam. Under these circumstances, the beam is actually in the spectrometer. Some of it is striking aperture stops and making spray and some is propagating through to the end. Thus, there is a high background rate of bad events and straight-through beam. To reduce this background, we took two steps. First, we brought the spectrometer jaw counters into the event trigger. These are set to veto anything that is at an angle of less than $\sim$ 1.2 mr from the beam. This eliminates triggers on straight-through beam and much of the spray. Second, a steel "dump block" is brought in just behind the jaw counters. This block is at a larger angle from the center of the spectrometer than the jaw counters and therefore does not define the acceptance (see Figure 27). It is introduced to cut down the counting rate in the MWPCs so that their electronic circuitry will not get into dead time problems. Since the remaining background was beam related, it was removed by the empty target subtraction. Moreover, all the background showed up at very small vertical angles so that a simple vertical angle cut removed it (at the cost of the lowest few t bins). This procedure allowed us to get to t values as low as -.05 at high energies. There is, of course, some concern that this procedure may have additional systematic errors.

When the beam was set up to transport positively charged particles, the rates were always high. We set a limit (by closing collimators if necessary) of $\sim 2.5 \times 10^6$ particles per pulse to avoid accidental coincidence problems.

The approximate composition of the beam at each energy is shown in Table 9 (these numbers are corrected for the efficiencies of the beam Cerenkov counters). Obviously, at 50 GeV/c we are rich in pions and moderately comfortable with respect to protons. At 175 GeV/c, we are very rich in protons and moderately comfortable with respect to pions. At both energies, we are very poor in kaons. At low t, where we were computer limited, we were able to use the beam countdown to get 45% pion events, 45% proton events, and 10% kaon events. The paucity of kaons had this implication for the experiment: in order to get moderate statistics on kaons (say $\sim$ 5000 events) we had to run for such a long time that we acquired very large statistics on on πs and Ps. This meant that our uncertainties were always systematics-dominated on πs and Ps but statistics-dominated on Ks. Our analysis reflects this fact. The proton and pion analysis applies very tight cuts while the kaon analysis is somewhat more relaxed.

Small changes in Cerenkov counter deployment were necessitated by efficiency considerations. The deployment of Cerenkov counters is shown in Table 10b.

Figure 27. SETUP FOR SCATTERING AT VERY SMALL ANGLES

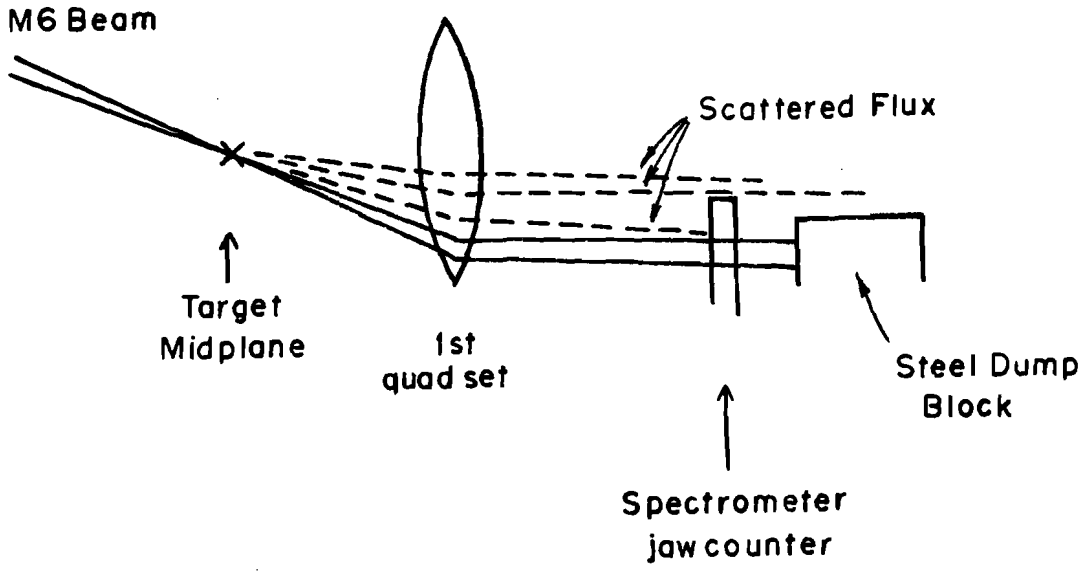

TABLE 9

Particle Composition* of the M6 Beam

	π**	K	P
50	77.5%	2.5%	20%
70	65.8%	3.2%	31%
140	22.6%	2.6%	74.8%
175	10.8%	1.7%	87.5%

*We present the composition of the flux arriving at the hydrogen target. Decay corrections must be applied to the kaons to infer the flux at the production target.

**'Pions' include $\sim$ 1% muons and 1% electrons at all energies.

TABLE 10

Details of the Run Plan

a. Kinematic settings for elastic scattering (the spectrometer momentum is set 1% below the beam momentum for elastic scattering.)

Momentum	Angle setting
50 GeV/c	3.5, 5.0, 6.5, 8.0, 9.5, 11.0, 12.5, 14.0, 15.5 mr
70 GeV/c	3.5, 4.5, 6.0, 9.0, 10.5 mr
140 GeV/c	2.375,* 4.0, 5.5 mr
175 GeV/c	2.5,* 4.0 mr

*means that the special small angle running procedure employing the dump block was used.

b. Deployment of Cerenkov Counters
(entries are: pressure (PSIA) - gas - sensitivity)

	50	70	140	175
B_{gas}	9.5-He-π	8.4-He-π	2.5-He-π	1.7-He-π
B_{dif}	46.5-He-k	64.7-He-p	34.4-He-p	30.3-He-p
B_{disc}	He-p	He-k	He-k	He-k
S_{gas1}	8.0-He-π	6.3-He-π	2.6-He-π	1.5-He-π
S_{gas2}	54.0-He-π+k	32.6-He-π+k	9.5-He-π+k	1.6-He-π
S_{gas3}	63.5-He-π+k	36.4-He-π+k	9.5-He-π+k	1.6-He-π
S_{difr}	evacuated	9.9-He-p	28.0-He-p	26.8-He-p
S_{difa}	evacuated	-	28.0-He-π+k	26.8-He-π+k

(At 70 GeV/c S_{dif} is operated in threshold mode with the anti-coincidence mirror out.)

CHAPTER VI

ANALYSIS OF THE DATA

The analysis of the data proceeds in three stages or passes:

Pass I: Event-by-event analysis: event reconstruction, sorting of events into unnormalized distributions for each run.

Pass II: Run combination and calculation of cross sections.

Pass III: Application of final physics and efficiency corrections; fitting, tabulation, and plotting of results.

Each stage will be described briefly.

A. Pass I: Event-by-event analysis

Events are read in from the data tape and their bit patterns are unpacked and decoded. Beam events and spectrometer events are treated as follows:

Beam event decoding: The bits representing the status of the beam Cerenkov counters are examined and the incident particle is identified as a pion, kaon, nucleon, or ambiguousity. The beam hodoscope bits are decoded and a coordinate is calculated for each hodoscope. The incident coordinates x_i, θ_i, y_i, ϕ_i, and δ_i are calculated. The information associated with this event is passed to "histogramming" or "sorting" routines which enter it into various distributions accumulated for each run.

Spectrometer event decoding: The beam Cerenkov counters are examined to determine the incident particle type. The spectrometer Cerenkov bits are unpacked and examined to determine the scattered

particle type. The beam hodoscopes are decoded and incident coordinates are calculated. The MWPC struck wire addresses are examined and a coordinate is calculated for each wire plane. The track at the back of the spectrometer (see Section III3) is determined. The spectrometer track and the incident coordinate x_i are used to calculate the production coordinates x_p, θ_p, y_p, ϕ_p, and δ_p (Section III4). Finally, kinematic quantities, t, MM^2, ϕ_T, and P_T, are computed. The information for the decoded event is passed to sorting routines which enter it into various distributions.

The geometric reconstruction is standardized for all energies reported here. Hodoscope bit patterns are valid if there is a single hit or two adjacent hits in a hodoscope. Counts are maintained of events with no hits in a hodoscope and of events with non-adjacent hits. Counts of zeroes and other non-valid patterns are maintained for each chamber. The spectrometer tracking algorithms do not require a valid track in each of the ten chambers. Certain combinations of chambers with valid tracks have sufficient information to calculate the trajectory. Each of these combinations has been studied and those which do not degrade the overall resolution are considered valid.

The particle identification is accomplished by comparing the pattern of Cerenkov counter hits with a truth table. The truth table defines the valid patterns for each particle type. The truth tables used to identify particles differ among the four energies and are shown in Table 11.

Pass I also includes some general histogramming facilities which make it useful for preliminary studies. The particle identification truth tables are optimized in these studies. Acceptance cuts are determined.

TABLE 11

Truth Tables for Particle Identification*

	Beam Particle Identification				Spectrometer Particle Identification			
	B_{gas}	B_{difR}	B_{difa}	B_{disc}**	S_{gas1}	$S_{gas2,3}$	S_{difR}	S_{difa}
50 GeV/c								
π	✓	x		x	✓			
K	x	✓		x	x	✓		
P	x	x		✓	x			
70 GeV/c								
π	✓	x		x	✓			
K	x	x		✓	x	✓		
P	x	✓		x	x		✓	
140 GeV/c								
π	✓	x		x	✓			
K	x	x		✓	x	✓	x	
P	x	✓		x	x			
175 GeV/c								
π	✓	x		x	✓			
K	x	x		✓	x	x		✓
P	x	✓		x			✓	

✓ means presence of signal required

x means absence of signal required

blank means not used

---

*Pressure settings for the counters are given in Table 10. Beam masks are mutually exclusive. Spectrometer masks are not mutually exclusive. The order of the search determines which definition is used if more than one is possible. The order is: pions, kaons, protons.

**B_{disc} is a logic signal formed from the eight disc phototube signals. It requires three of the four even numbered counters and three of the four odd numbered counters to have fired.

Pass I generates as output many statistics summaries and two different kinds of distributions.

i) diagnostic histograms and scatter plots: these quantities, include detector profiles, distributions of calculated quantities, histograms which verify the validity of cuts, correlation plots between beam particle type and spectrometer particle type, etc. These are used to make a judgement concerning the performance of the apparatus during a run.

ii) Yields Planes (scatter plots of events in momentum and angle):

Individual spectrometer events are sorted into two dimensional distributions called "yields planes" which form the basis of the cross section calculation. Separate yields planes are maintained for each of the following reactions:

$$\pi + p \rightarrow \pi + x$$

$$K + p \rightarrow K + x$$

$$p + p \rightarrow p + x$$

There are two different kinds of yields planes. In one, events are binned according to ϕ_T and P_T (Type 1). In the other, they are binned according to ϕ_p and P_T (Type 2). The range in the momentum variable P_T corresponds to a (missing mass)^2 interval of 0 to $\sim$ 2 GeV/c^2 so that both elastic events and low MM^2 inelastic events enter the yields distributions. This allows us to see both the shape of the elastic peak and the shape of the nearby inelastic cross section which is a potential source of background. The use of two different angle variables reflects two different ways of including the beam direction and

angular divergence in the calculation of the cross section. If the binning is in the variable ϕ_T, then the beam angle information is used explicitly for each event to decide what its scattering angle is. If the binning is in ϕ_p, the effect of the incident angles must be incorporated in an average way for all the events. Pass I calculates the average properties of the beam - its first and second moments - for each incident coordinate from the beam event sample.

The horizontal angle, θ_p, is treated in the calculation of the cross section as a pure azimuthal angle. Since it is not an azimuthal angle, a small correction is required. Each yields plane has associated with it a definite cut on horizontal angle. Only events satisfying the horizontal angle requirement are entered into the yields plane.

The requirements for admission of an event into a particular yields plane are:

1) appropriate reaction type based on identification of the incident and scattered particle.

2) 'successful' reconstruction of the incident and scattered trajectory. The requirements on the incident track are different for the yields plane in ϕ_p and the yields plane in ϕ_T. The former does not use the incident angle information for each event and therefore requires good tracks in BP and BX only. (BP measures beam momentum and BX is required in the spectrometer decode algorithm). The latter needs incident angle information for each event and requires a good track in each beam hodoscope for each event that enters it.

3) survival of all geometric acceptance cuts. For Type 1, cuts are applied to δ_s, ϕ_p, and θ_p. These cuts permit only events which are in the uniform acceptance region to enter the plane. For Type 2, cuts are applied to θ_p and δ_s to restrict events to the uniform acceptance in those variables. ϕ_p is limited only by the size of the distribution for Type 2.

A total of five yields planes are created by Pass I for each run. These are described in Table 12. Figure 28 shows how one of these distributions looks.

The yields planes for each run and the parameters which describe them are written out to magnetic disk storage for use by Pass II. Auxiliary information which is required for the normalization of these yields is also written out to the disk. This includes total beam flux for each run, the composition of the beam by particle type, the moments of the beam distributions, the beam and spectrometer reconstruction efficiencies, the kinematic settings, and the length and content of the target.

The flux 'BT' for particles of type i is determined from a combination of the flux scaler reading, NB, and information obtained from the beam event sample. The flux scaler is first multiplied by f_1, the fraction of particles of this type in the beam. This fraction is obtained from the beam sample:

$$f_1^i = \frac{(\#\text{ of beam events satisfying Cerenkov requirements for this particle type})}{\text{total \# of beam events}}$$

TABLE 12

Description of Yields Planes

a. Types of Yields Planes

Type 1

Hodoscope requirements: a good* track in each of the five beam hodoscopes.

Production coordinate cuts:**

$|\theta_p| < .75$ mr
$|\phi_p| < 1.4$ mr
$|\delta_s| < 1.75\%$

Coordinates of the yields plane:

ϕ_T, δ_T

Limits: $-.40 < \delta_T < 1.50\%$, $-2.0 < \phi_T < +2.0$

*'a good track' means a single hit or a single pair of adjacent hits.

Type 2

Hodoscope requirements: a good track in the BP and BX hodoscopes. No ambiguous tracks in any hodoscope.

Production coordinate cuts:**

$|\theta_p| < .75$ mr
$|\phi_p| < 1.8$ mr
$|\delta_s| < 1.75\%$

Coordinates of the yields plane:

ϕ_p, δ_T

Limits: $-.40 < \delta_T < 1.50\%$, $-1.8 < \phi_p < +1.8$

b. Description of the five yields planes:

	π	K***	P
Type 1	✓		✓
Type 2	✓	✓	✓

***A Type 1 kaon yields plane would have had insufficient statistics to be of much value.

**These are modified if the spectrometer jaw counters are in the trigger.

DISTRIBUTION OF SCATTERED PROTONS IN TRANSFER PSIV,DELTA

PSIV (.1 MR)	(HORIZONTAL DISPLAY TRUNCATED TO 30 BINS)																					
-59	0	0	0	0	0	0	0	0	0	0	0	0	0	0	0	0	0	0	0	0	0	0
-57	0	0	0	0	0	0	0	0	0	0	0	0	0	0	0	0	0	0	0	0	0	0
-55	0	0	0	0	0	0	0	0	0	0	0	0	0	0	0	0	0	0	0	0	0	0
-53	0	0	0	0	0	0	0	0	1	0	0	0	0	1	0	0	0	0	1	0	0	2
-51	0	0	0	0	0	0	1	0	0	0	3	0	1	1	1	0	0	0	1	0	1	0
-49	0	0	0	0	0	0	0	0	0	1	3	2	1	1	0	0	1	0	2	1	0	0
-47	0	0	0	1	0	0	1	0	1	0	2	2	1	1	2	1	0	1	2	1	1	2
-45	0	0	0	0	0	0	0	0	2	4	4	5	1	0	1	4	0	0	1	2	0	1
-43	0	0	0	0	0	0	1	0	3	5	7	4	1	1	2	0	0	1	1	2	1	3
-41	0	1	0	0	0	0	1	1	5	11	15	4	1	1	1	2	1	1	2	0	1	2
-39	0	0	1	0	0	0	1	1	13	27	15	8	3	1	1	1	0	3	0	1	1	3
-37	0	0	0	0	0	0	1	10	31	47	22	5	3	3	3	1	2	7	5	3	3	3
-35	0	1	0	1	0	1	4	12	52	50	25	11	3	4	3	3	4	5	2	8	6	8
-33	1	1	0	1	2	3	11	52	91	80	26	8	8	4	3	7	5	4	4	7	12	5
-31	0	0	1	0	2	5	19	69	132	90	30	10	3	5	7	2	7	5	7	3	6	7
-29	0	0	0	0	4	5	42	150	185	89	23	6	3	3	5	7	4	4	10	5	11	10
-27	0	0	2	1	3	11	40	153	161	62	14	5	2	4	5	4	4	6	5	6	11	9
-25	0	1	0	0	0	3	10	35	41	15	1	5	2	0	1	3	1	0	0	1	2	4
-23	0	0	0	0	0	0	0	1	0	0	0	0	0	0	0	0	0	0	0	0	0	0
-21	0	0	0	0	0	0	0	0	0	0	0	0	0	0	0	0	0	0	0	0	0	0
SUM	1	4	4	4	11	28	132	484	718	481	190	75	33	30	35	35	29	37	43	40	56	59
	-37	-32	-27	-22	-17	-12	-7	-2	2	7	12	17	22	27	32	37	42	47	52	57	62	67

DELTA (.01%)

TOTAL EVENTS: 2957 TRANSFER MOMENTUM UNDERFLOWS: 0 TRANSFER MOMENTUM OVERFLOWS: 0

OUTPUT ON EPIC1 : TYPE 1101 RECORD IN NUP170 (R1855508)
SELECTED: PERFECT EVENTS WITHIN ALL ACCEPTANCE CUTS

Figure 28. EXAMPLE OF A YIELDS PLANE
$p + p \rightarrow p + x$, type 1, 175 GeV/c

The fraction reflects the choice of particle identification signals used to identify the particle. The efficiency of the counters with respect to this choice is automatically included in f_1. Since a scattered event is used in the analysis only if the incident particle which initiated it satisfied certain criteria - e.g. good beam hodoscope signature, incident coordinates satisfying some geometric cuts, we must determine what fraction f_2 of the incident flux of this type of particle satisfied those requirements. This is also computed from the beam sample:

$$f_2^i = \frac{(\#\text{ of beam events of this particle type satisfying beam geometry requirements})}{\text{total beam events of this particle type}}$$

The efficiencies of the hodoscopes are included in f_2. The total flux is then

$$'BT_i' = f_1^i \times f_2^i \times NB$$

The following points should be noted:

1) In order for this flux determination to be appropriate for the cross section calculations, identical requirements must be placed on the beam events entering the numerators of f_1 and f_2 as are put on the incident particle of a scattering (spectrometer) event entering the yields plane. If different types of yields planes have different beam requirements, separate fractions f_1 and f_2 must be computed for each type. Pass I does this for each yields plane it creates and writes the fractions out onto the disk.

2) Because the fractions f_1 and f_2 are obtained from a finite sample, there is a sampling error. This contributes a very small increment to the overall statistical error of each cross section.

B. Pass II: Conversion of Yields to Absolute Cross Sections

Two different calculations are required to convert the two types of yields planes to absolute cross sections.

The first step in both calculations is the same: the summation over the elastic peak in the variable P_T to form an elastic yield for each angle (ϕ_T or ϕ_p) bin. We define the elastic peak as an interval in MM^2 extending from 0 to 1.5 GeV^2/c^4, assuming that the center of the distribution is at .88 GeV^2/c^4. If the peak is not centered at a P_T corresponding to .88 (due to a relative missetting of beam and spectrometer momentum), the interval is shifted to include a P_T range corresponding .62 GeV^2/c^4 on the high MM^2 side of the peak and .88 GeV^2/c^4 on the low MM^2 side of the peak (see Figure 29). This interval is large. The interval between the center of the peak and the high MM^2 limit is 3-1/2 $\sigma_{MM}{}^2$ at 175 GeV/c and is 4-1/2 $\sigma_{MM}{}^2$ at 50 GeV/c. Inelastic threshold lies within the cut. The reasons for choosing this large interval are 1) the inelastic background is very small out to $t \sim -.7$. 2) the wide cut desensitizes us to small residual errors in the location of the peak. With a wide cut, the main effect of an error is to slightly change the size of the inelastic contamination. No gross error in the number of elastic events is possible. 3) the outscattering of events from the peak due to nuclear reactions, multiple scattering, and decays extends quite far away from the main peak (defined, for example, as $\pm$ 3 $\sigma_{MM}{}^2$ from the peak center). Most of the outscattering is included in our cut. (A residual correction which is

Figure 29 MM^2 Cut on Elastic Events

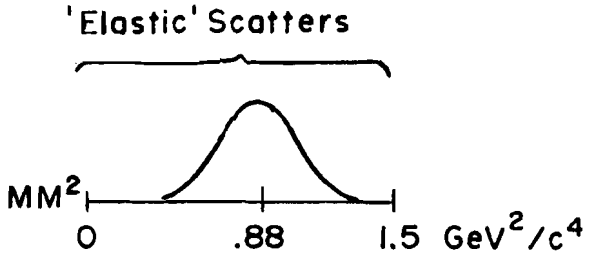

a. The MM^2 cut if beam and spectrometer momentum are properly set relative to each other.

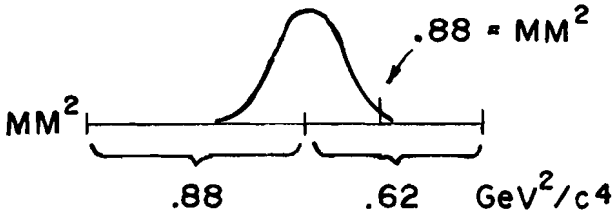

b. If spectrometer or beam is misset, peak does not fall at $MM^2 = .88$. Cut is located relative to found peak.

of order 1/2% is applied for outscattering.) 4) the fixed, energy-independent cut will be shown (Section VIIE) to simplify the correction for inelastic background contamination. 5) the wide cut includes essentially all double scattering events which occur. We correct for this by means of a simple calculation with the large cut. We avoided the possibility of including varying amounts of double scattering and thereby complicating the correction.

1. Computation of the Cross Section for Type 1 Yields

The calculation of a cross section from the yields plane is accomplished by first writing an integral relating the yield in a bin to the cross section and then inverting it. The yield (Type 1) is defined for a bin in transfer vertical angle and fixed horizontal angle (θ_p) acceptance.

$Y^e(\phi_T^c, \Delta\phi_T, \Delta\theta_p)$ = # of counts within the elastic peak in angle bins defined by relations 1 and 2 below. The superscript "e" indicates that the summation over the elastic peak has already been performed.

$$1) \quad \phi_T^c - \Delta\phi/2 < \phi_T < \phi_T^c + \Delta\phi/2$$

$$2) \quad -\Delta\theta_{p/2} < \theta_p < \Delta\theta_{p/2}$$

that is, ϕ_T^c is the center of the bin in vertical transfer angle, $\Delta\phi_T$ is the width of the bin, and $\Delta\theta_p$ is the horizontal angle acceptance.

The yield is related to the cross section by:

$$3)\quad Y^{e}(\phi_T^{c},\Delta\phi_T,\Delta\theta_p) = \rho_{\ell H_2} N_A \Delta z' BT' \int \frac{d^2\sigma}{d\phi_T d\theta_p}(\phi_T^{2}+\theta_T^{2})\, B(x_i,\theta_i,y_i,\phi_i)$$

$$\times\ \varepsilon(x_i,\theta_p,y_i,\phi_T+\phi_i)\ \times\ dx_i dy_i d\phi_i d\theta_i d\theta_p d\phi_T$$

where the limits of integration in θ_i and ϕ_i are such that $\phi_T+\phi_i = \phi_p$ lies within the uniform acceptance and $\theta_T+\theta_i = \theta_p$ satisfies relation 2. The limits in ϕ_T are defined by relation 1. The limits in x_i and y_i extend over the whole incident coordinate distribution satisfying the geometric requirements for this yields plane. The other quantities appearing in Equation 3 are:

a) $\rho_{\ell H_2}$ is the density of the liquid hydrogen target

b) N_A is Avogadro's number

c) Δz is the length of the target

d) 'BT' is the total incident flux associated with this yield plane. Its computation from the flux scaler and the beam event sample was discussed in the previous section.

e) $B(x_i,\theta_i,y_i,\phi_i)$ is the incident beam phase space distribution. It is normalized so that

$$\int B(x_i,\ \theta_i,\ y_i,\ \phi_i)dx_i dy_i d\theta_i d\phi_i = 1$$

where the integral extends over the whole range of each coordinate permitted by the geometric cuts on the beam for this yields plane.

f) $\epsilon(X_p, \theta_p, y_p, \phi_p)$ is a geometric efficiency (acceptance) function for scattering from the production coordinates x_p, θ_p, y_p, and ϕ_p into the spectrometer. This function takes on two values: a <u>one</u> if the spectrometer transmits (accepts) a particle with these four quantities at the target midplane and a <u>zero</u> if it does not. In Equation 3, we have used the fact that $\theta_T + \phi_i = \phi_p$ and $X_i \sim X_p$ and $y_i \simeq y_p$.

g) $\frac{d^2\sigma}{d\phi_T d\phi_p}(\phi_T^2 + \theta_T^2) = \frac{d\sigma}{d\Omega}(\phi_T^2 + \theta_T^2)$ is the differential cross section for scattering into the bin of solid angle $\Delta\theta_p \Delta\phi_T$ defined by relations 1 and 2.

Equation 3 can be simplified as follows: The beam phase space at the target has been found to have no correlations that actually affect the cross section so that:

$$B(x_i, \theta_i, y_i, \phi_i) \simeq B_x(x_i)\, B_\theta(\theta_i)\, B_y(y_i)\, B_\phi(\phi_i)$$

where the one dimensional profile functions $B_g(g_i)$ are normalized as follows:

$$\int_{\substack{\text{Region of } g_i \\ \text{within beam} \\ \text{cuts for this} \\ \text{yield plane}}} B_g(g_i)\,dg_i = 1$$

The B_x and B_y integrals are 1.

An additional simplification arises from the fact that we have demanded that events entering the yields plane fall within the uniform acceptance region. $\epsilon = 1$ everywhere within the integration region.

Equation 3 now reduces to

$$3') \quad Y(\phi_T^c, \Delta\phi_T, \Delta\theta_p) = \rho_{\ell H_2} N_A \Delta z' BT' \times \int d\phi_T d\phi_i B_\phi(\phi_i) \int d\theta_p d\theta_i B_\theta(\theta_i) \frac{d^2\sigma}{d\Omega}(\theta_T^2+\phi_T^2)$$

It has been demonstrated previously that the horizontal angle θ_T contributes very little to the overall scattering angle. We take advantage of this by expanding the cross section in a power series about ϕ_T^2

$$\frac{d\sigma}{d\Omega}(\theta_T^2+\theta_T^2) = \frac{d\sigma}{d\Omega}(\phi_T^2)\left\{1 + \frac{d/d\theta_T^2(\frac{d\sigma}{d\Omega})\Big|_{\phi_T^2}}{\frac{d\sigma}{d\Omega}(\phi_T^2)}\theta_T^2 + \text{higher order terms}\right\}$$

We define

$$b' = \left\{\frac{d}{d\theta_T^2}(d\sigma/d\Omega)/d\sigma/d\Omega\right\}\Big|_{\phi_T^2}$$

$$\left(\text{If } \frac{d\sigma}{d\Omega} \propto e^{bp^2(\phi_T^2+\theta_T^2)}, \quad b' = bp^2\right)$$

Then integrals over θ_i and θ_p become

$$I_\theta = \int \{1 + b'(\theta_i^2 + 2\,\theta_i\theta_p + \theta_p^2)\}\, B(\theta_i)d\theta_i d\theta_p$$

$$= \Delta\,\theta_p \{1 + (\sigma_{\theta_i}^2 + \frac{\Delta\theta_p^2}{12})b' + (\text{terms proportional to } \overline{\theta_p}, \overline{\phi_i})\}$$

where

$$\sigma_{\theta_i}^2 = \int B(\theta_i)\,\theta_i^2\, d\theta_i \text{ and } \overline{\theta}_p, \overline{\phi}_i \simeq 0.$$

Equation 3 is now

$$3'') \quad Y(\phi_T^c, \Delta\phi_T, \Delta\theta_p) = \rho_{\ell H_2} N_A \Delta z' BT' \Delta\theta_p \{1 + b'(\sigma_{\theta_i}^2 + \frac{\Delta\theta_p^2}{12})\}$$

$$\times \int B_\phi(\phi_i)\, \frac{d\sigma}{d\Omega}(\phi_T^2)\, d\phi_i d\phi_T$$

The bin size $\Delta\phi_T$ can be chosen sufficiently small so that $d\sigma/d\Omega$ can be moved outside the integrals. Finally,

$$\frac{d\sigma}{d\Omega}(\phi_T^2) = \frac{Y(\phi_T^2, \Delta\phi_T, \Delta\theta_p)}{\rho_{\ell H_2} N_A\, \Delta z\, 'BT' \Delta\theta_p \varepsilon \underbrace{\{1 + b'\sigma_{\theta_i}^2 + b'\,\Delta\theta_p^2/12\}}_{C_1}}$$

where

$$\varepsilon = \int B_\phi(\phi_i)\, d\phi_i d\phi_T$$

ϕ_i such that $\phi_p = \phi_T + \phi_i$ stays within the ϕ_p (uniform) acceptance.

The integral ε is evaluated numerically for each run from the beam event sample. The evaluation of ε and b' is discussed below.

The integration region for ε is shown in Figure 30a. $\pm \Delta\phi_p/2$ defines the uniform acceptance region chosen for the analysis. Since $\phi_i = \phi_p - \phi_T$, contours of constant ϕ_T are 45° straight lines on the (ϕ_i, ϕ_p) plane. The transfer coordinate bin, restricted to the uniform acceptance region, covers the shaded area of the (ϕ_i, ϕ_p) plane. The Jacobian between ϕ_i, ϕ_p and ϕ_i, ϕ_T is 1 so that the integral can be written

$$\varepsilon = \int\int_{\text{shaded area}} B_\phi(\phi_i)\, d\phi_i d\phi_p$$

Figure 30b is a plot of these integrals for different transfer coordinate bins within the spectrometer aperture. These integrals have a direct interpretation as the fraction of the beam seen by the transfer bin through the acceptance cut. The flat region means that these ϕ_T bins see the whole beam. The ε values fall off for ϕ_T bins which cannot receive contributions from some part of the beam.

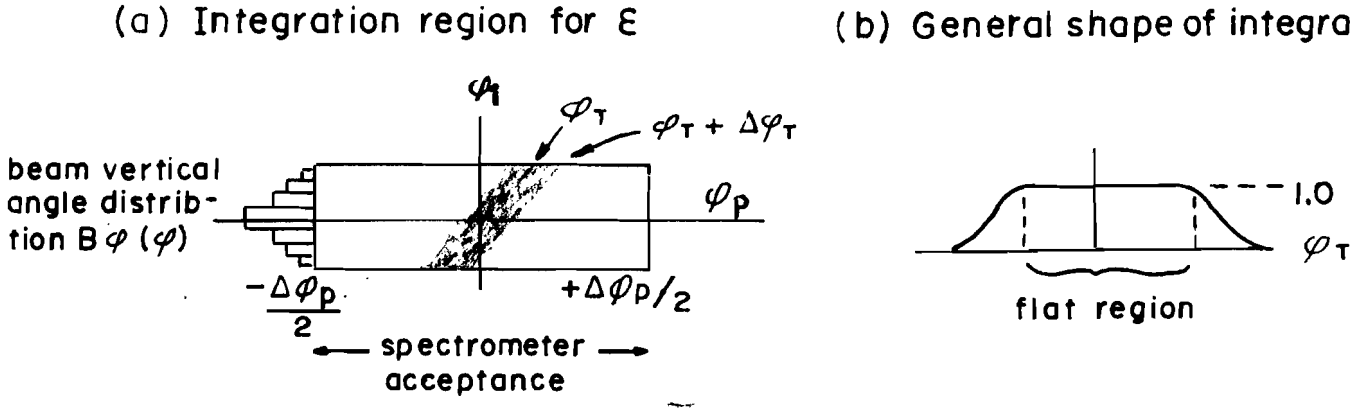

FIGURE 30: Integration Region for acceptance integrals

The term C_1 can be calculated exactly only if the differential cross section $d\sigma/d\Omega$ is known. In practice, C_1 is very close to 1 and can be estimated quite accurately. We have calculated the cross section by first setting $C_1 = 1$. This cross section is then fitted and the results of the fit are used to calculate b'. A revised cross section is then calculated. Since b' is known to change very slowly between t = 0 and t = 1.0 for elastic scattering, C_1 is primarily a scale correction. The largest correction is at 175 GeV/c for protons and varies from about 5% to about 3% over the t-range. At 50 and 70 GeV/c, the effect of C_1 is to change the result by less than 1% everywhere.

2. Calculation of the Cross Section from Type II Yields

For Type II yields we have

$$Y^2(\phi_p{}^c, \Delta\phi_p, \Delta\theta_p) = \begin{array}{l}\#\text{ of events within the elastic}\\ \text{peak in angle bins defined by}\\ \text{relations 1 and 2 below.}\end{array}$$

$$1)\quad \phi_p{}^2 - \Delta\phi_p/2 < \phi_p < \phi_p{}^c + \Delta\phi_p/2$$

$$2)\quad -\Delta\,\theta_p/2 < \theta_p < \Delta\theta_p/2$$

that is, $\phi_p{}^c$ is the center of the bin in vertical production angle (ϕ_p), $\Delta\phi_p$ is the width of the bin, and $\Delta\theta_p$ is the horizontal angle acceptance.

The yield is related to the cross section by

$$3)\qquad Y^2(\phi_p{}^c,\ \Delta\phi_p,\ \Delta\theta_p) = \rho_{\ell H_2} N_A \Delta z' BT' \int \frac{d\ (\phi_T{}^2+\theta_T{}^2)}{d\Omega}\ \varepsilon(x_p,\theta_p,y_p,\phi_p)\ x$$

$$\theta_x(x_i)B_\theta(\theta_i)B_y(y_i)B_\phi(\phi_i)\ x$$

$$d\theta_i\ dx_i\ dy_i\ d\phi_i\ d\theta_p\ d\phi_p$$

Again $\varepsilon = 1$ everywhere within the uniform acceptance and $\int B_x(x_i)dx_i = \int B_y(y_i)dy_i = 1$. Finally, $d\sigma/d\Omega$ is expanded around $\phi_p{}^c$

$$3')\qquad Y^2(\phi_p{}^c,\ \Delta\phi_p,\ \Delta\theta_p) = \rho_{\ell H_2}\ N_A\ \Delta z' BT'\ \frac{d^2\sigma}{d\Omega}(\phi_p{}^{c2})\{1 + 2b'\phi_p\bar{\phi}_b + b'\frac{\Delta\theta_p{}^2}{12} + b'\sigma_{\theta_i}{}^2$$

and other terms and

$$+\ 2\ b'^2\ \phi_p{}^2\ \sigma_{\phi_i}{}^2\}\ \Delta\theta_p\ \Delta\phi_p$$

Only the terms which are significant (i.e. above the one percent level) appear in 3'. Finally,

$$3'')\qquad \frac{d^2\sigma}{d\ \Omega}\ (\phi_p{}^c) = \frac{Y^2(\phi_p{}^c,\ \Delta\phi_p,\ \Delta\theta_p)}{\rho_{\ell H_2} N_A \Delta z' BT' \Delta\theta_p \Delta\phi_p\{1 + 2b'\phi_p\bar{\phi}_b + b'(\Delta\theta_p{}^2/12 + \sigma_{\theta_i}{}^2)}$$

$$\underbrace{+\ 2\ b'^2\phi_p{}^2\sigma_{\phi_i}{}^2\ \ldots\}}_{C_2}$$

The term C_2 contains the same term, $b'(\Delta\theta_p{}^2/12 + \sigma_{\theta_i}{}^2)$, which appeared in the Type I yields calculation. This is the correction for ignoring the contribution of the horizontal angle to $\phi^2 = \phi_T{}^2 + \theta_T{}^2$. The term $2'\phi_p\bar{\phi}_b$ takes into account the average angle of the beam particles.

In Type I, each event is entered into the yields plane according to both the scattered and incident angle so that the average angle of the beam is taken into account implicitly. The term $2b'^2\phi_p^2\sigma_{\phi_i}^2$ corrects for the fact that, even if $\bar{\phi}_i = 0$, the angular divergence of the beam changes the average $(\text{angle})^2$ of the ϕ_p bin.

The C_2 term is larger than the C term encountered in the Type I calculation. C_2 has, moreover, a much stronger t dependence due to the appearance of terms in ϕ_p. Iterative techniques guarantee that these corrections are computed accurately.

Choice of Type I or Type II Calculation:

The correction terms are easier to compute for Type I yields. On the other hand, many more events are entered into the Type II yields because of the relaxed beam track reconstruction requirement. Thus, the Type I calculation is less vulnerable to systematic errors but the Type II calculation has better statistical accuracy.

We have taken the view that whenever the Type I yields have sufficient events so that we are limited by the systematic uncertainties, we would use them for the cross section calculation. When we are statistics limited in the Type I yields, we switch to Type II yields.

In practice, this means that pion and proton cross sections are calculated from Type I yields and kaon cross sections from Type II yields. Comparisons of the Type I and Type II calculations for pions and protons have been carried out. Parameters obtained from fits to Type I and Type 2 cross sections agree to about 1%.

Nonuniform acceptance and ratio techniques for minority particles:

The acceptance cuts eliminated about 50% of the events. In order to improve the statistical accuracy of the K^+P cross section, a ratio technique was used to calibrate the non-uniform acceptance of the spectrometer. Then the K^+P cross sections could be obtained using the whole aperature. First, the pion cross section was obtained using only the uniform acceptance. The cross section was fitted so that its value $d\sigma/dt\big|_f^\pi$ was known at each angle ϕ. A cross section $d\sigma/dt\big|_{nu}^\pi$ obtained from a bin in the nonuniform acceptance at the angle ϕ was related to the fitted cross section value by

$$\left.\frac{d\sigma}{dt}\right|_f^\pi = \bar{\varepsilon} \left.\frac{d\sigma}{dt}\right|_{nu}^\pi$$

where $\bar{\varepsilon}$ is the average acceptance of the bin. The $\bar{\varepsilon}$ obtained by ratioing the two pion cross sections is applied to the kaon cross section for the same angle bin ϕ in the nonuniform acceptance.

$$\left.\frac{d\sigma}{dt}\right|^k = \left.\frac{d\sigma}{dt}\right|_{nu}^k \bar{\varepsilon} \ .$$

The statistical error on $\bar{\varepsilon}$ made only a small contribution to the overall error. This ratioing procedure amounts to using the flux of scattered pions to Monte Carlo the spectrometer acceptance.

3. Run Combination

Elastic cross sections for several runs are combined as follows: The elastic cross sections for each run are converted back to elastic yields and associated fluxes. The total yield for all full target runs,

Y_f, is accumulated. The total flux, B_f, for all full target runs is also accumulated. Similarly, Y_e and B_e, the cumulative yield and flux for all empty target runs are computed. The full target cross section, $\frac{d\sigma^f}{d\Omega}(\phi)$, is

$$\frac{d\sigma^f}{d\Omega}(\phi) = \alpha C_f \, Y_f/B_f$$

where α represents all the usual constants and C_f is the correction for spectrometer transmission losses, absorption in the hydrogen target, and spectrometer detector efficiency (averaged over all combined runs). The "empty target" cross section, $\frac{d\sigma^e}{dt}$, is

$$\frac{d\sigma^e}{d\Omega}(\phi) = \alpha \, C_e \, Y_e/B_e$$

where C_e is the correction for spectrometer transmission losses and average detector efficiency. The true cross section is

$$\frac{d\sigma}{d\Omega}(\phi) = \alpha \{C_f \, Y_f/B_f - C_e \, Y_e/B_e\}$$

The angle ϕ corresponds to a central t-value

$$-t = \frac{(P_b{}^c\phi)^2}{1 + (P_b{}^c \, \phi^2)/2 \, M_p} \quad .$$

(Pass II corrects for bin size effects so that the cross section can be plotted at the central t-value). Conversion to $d\sigma/dt$ is accomplished by multiplying $d\sigma/d\Omega$ by the Jacobian J:

$$J = \pi/P_b{}^c P_s \simeq \pi/P_b{}^c(P_b{}^c - |t|/2M_p) \ .$$

The statistical error Δ_f on the full target cross section $\frac{d\sigma^f}{dt}$ is given by

$$\Delta_f{}^2 = J^2\alpha^2 C_f{}^2 \{Y_f/B_f{}^2 + Y_f{}^2/B_f{}^4 \ \sigma_{B_f}{}^2\}$$

$$= \left(\frac{d\sigma^f}{dt}\right)^2 \{1/Y_f + \frac{1}{N_{bev}} \left(\frac{1-f}{f}\right)\}$$

where N_{bev} is the total number of beam events in the full target runs and f = the fraction of beam events satisfying the analysis criteria. The factor (1-f)/f takes into account the correlated statistics associated with the measurement of a fraction of the form A/A+B. The same formula is used to compute the error Δe on the empty target cross section $\frac{d\sigma^e}{dt}$. The error Δ on the final cross section is

$$\Delta\left(\frac{d\sigma}{dt}\right) = \{\Delta_f{}^2 + \Delta_e{}^2\}^{1/2} \ .$$

Cross sections are determined separately for AVB+ runs and AVB- runs and averaged in the manner described in Section IVc.

CHAPTER VII

FINAL CORRECTIONS TO CROSS SECTIONS

Several corrections must be applied to the raw yields and fluxes to convert them to absolutely normalized hadronic cross sections. Two of these, the spectrometer transmission and the spectrometer reconstruction correction, are applied to individual runs by the Pass II programs. These will be discussed more thoroughly in this section. All the other corrections are applied to the combined cross sections (which are the output of Pass II) by a third stage of the analysis - Pass III. Some of these corrections are overall scale corrections and others are t-dependent.

In order to determine these corrections, it was frequently necessary to go back to the original data tapes to do special studies. Other corrections could be calculated from first principles and still others were determined by direct online measurements during the experiment.

Detector Efficiencies

Spectrometer Reconstruction Efficiency: Our spectrometer tracking algorithms successfully reconstructed 95% of the scattered events. Studies showed that the 5% $\pm$ 1% inefficiency was distributed uniformly over the aperture used in the analysis. The total yield for each run was corrected upward by the efficiency determined for that run.

Spectrometer Cerenkov Efficiency and Misidentification: Elastic physics does not require identification of the scattered particle. If the beam particle is correctly identified and the scattered particle appears in the elastic peak, the scattered particle can be assumed to be the same as the incident particle. There is, of course, the risk that the beam particle was misidentified. In this analysis we used both sets of Cerenkov counters although the spectrometer particle identification requirements were fairly relaxed. Because we have used both sets of Cerenkov counters, any errors in the scattered flux due to particle misidentification are below the .1% level. We have had to pay the following price to achieve this: small corrections had to be made to the observed yields to account for inefficiencies in the spectrometer particle identification. These efficiency corrections never exceeded 3% for protons or 1% for pions and kaons.

Beam Detector Efficiencies: The beam hodoscope and beam Cerenkov efficiencies are taken care of automatically by our use of the beam event sample to determine the effective flux.

Error in Beam Flux due to Beam Particle Misidentification: Beam particle misidentification was reduced to a negligible (less than .1%) level by requiring very strict beam particle identification criteria. A particle had to be positively identified by one counter and have no other counters fire.

Dead Time, Accidental and Rate Corrections: The data acquisition system was made deadtimeless by the fast-gating system. The rates in the spectrometer were always very low compared to the capabilities of the detectors. The only accidental effects were associa-

ted with the counting of the beam flux.

The r-f systems of the main and booster synthrotrons both operate at 53 mHz. The r-f structure is not removed by debunching so that the particles emerge in "r-f buckets" of 1-2 nanoseconds (nsec) duration separated by 19 nsecs. This time structure is preserved in the secondary beams.

Our beam trigger counters had no difficulty counting r-f buckets which contained at least one charged particle but they could not count the number of particles within the buckets. The trigger counters therefore underestimated the total flux. The beam hodoscopes had sufficient granularity so that the simultaneous passage of two particles nearly always left two non-adjacent tracks in at least one hodoscope. Such events were rejected by the analysis from both the beam and spectrometer sample. In the beam flux calculation (Section V) the fraction f_2 automatically includes a correction to the beam flux for the rejection of buckets with more than one particle.

At rates of 1.5-2.5 x 10^6 particles/pulse, fewer than 10% of the r-f buckets contained more than one particle. The rejection of these by the hodoscopes was sufficient to reduce the possible underestimation of the flux to the .2% level. Since the uncertainty in this correction is nearly as large as the correction itself, we have not corrected the result for this effect but have included a .2% systematic error in the systematic uncertainty in the overall scale.

We checked for additional rate and deadtime effects by taking a series of runs with rates of 1, 2, and 3x10^6 particles/pulse. The rate of scattered flux per incident particle satisfying the analysis criteria agreed to within statistics (a few tenths of a percent).

Physics Corrections

A. Absorption and Decay Corrections:

Not all of the particles scattered into the solid angle covered by the spectrometer actually travel all the way to the end of the spectrometer. Some are immediately absorbed in the hydrogen target. Others are absorbed in the material of the spectrometer. Furthermore, if the scattered particle is a pion or kaon, it may decay and be lost. The observed scattered flux must be corrected upward for these losses.

At each energy, we measured these effects by bringing the incident beam directly through the spectrometer. The spectrometer "Trigger Transmission" was taken to be

$$\left\{\begin{matrix}\pi\\k\\p\end{matrix}\right\}\ \text{"Trigger Transmission"} = \frac{\text{Beam}\left\{\begin{matrix}\pi\\k\\p\end{matrix}\right\} \cdot \text{Spectrometer Trigger}}{\text{Beam}\left\{\begin{matrix}\pi\\k\\p\end{matrix}\right\}}$$

This measurement was performed with a very narrow pencil beam. The pencil beam was then scanned across the whole useful spectrometer aperture. The transmission numbers were found to be independent - to a precision of $\sim$ .3% - of the path the particles took through the spectrometer.

The transmission measurements were made first with the empty target cell in place and then with the 20" H_2 cell. The difference provided a measurement of absorption in the hydrogen.

These transmission numbers are not quite the ones which are required to correct the elastic yield. Any particle which causes a trigger, even though it may have been substantially deviated from its original trajectory by a nuclear collision or by decay, counts as a

transmitted particle. Such a particle might have been elastically scattered but might not appear in the elastic peak. To be consistent with our selection procedures for elastic scattering, this particle should not be counted as transmitted.

The simple "Trigger Transmission" must therefore be corrected downward to produce an "elastic peak transmission." This is accomplished by taking a straight-thru run and determining for each particle type the fraction f of transmitted particles whose measured momentum is such that the particle would fail the cut on missing mass. For incident protons, the scatter out of the peak is due to interactions of the protons in the material of the spectrometer. For incident kaons and pions, decays also throw particles out of the peak.

The 'elastic peak transmission' is calculated by multiplying the numerator in the "trigger transmission" by the fraction (1-f) determined for each particle type.

The 'elastic peak transmissions' are shown in Table 13 together with absorption numbers for the hydrogen target. These numbers have been checked by making independent calculations of decay corrections and absorption. The calculated and measured numbers agree to $\sim$ 1%. The measured numbers are used in calculating the cross section.

B. Contamination of Incident Particle Flux by Positrons and Muons: When the beam threshold counter was operated normally - with its pressure between π and K threshold - it was also sensitive to positrons and muons. These particles do not scatter appreciably into the spectrometer because they interact electromagnetically, but they do increase the apparent particle flux. This reduces the apparent cross section. In addition, K^+ mesons may decay after they have been tagged by the

differential counters and the decay products (π^+ or μ^+) may cause a trigger. Such reactions might produce a scattering which looks like $K^+ + P \rightarrow \pi^+ + X$. Since such an event can never be mistaken for an elastic scatter, the only effect is to artificially increase the K^+ flux. Special studies were made on-line to measure these backgrounds so that corrections can be applied. These studies and their results are described below.

Electron Contamination:

Threshold Cerenkov counters in the beam and in the spectrometer were operated below pion threshold so that they were sensitive to electrons. In addition, a shower counter at the back of the spectrometer showed a pulse height spectrum with a clear electron peak when the main beam was steered through it. Since electrons in the neighborhood of the target are expected to be 'beamlike' the only difference between the electron flux at the hydrogen target and at the shower counter is due to the showering of electrons in the material of the spectrometer (a small fraction of a radiation length). The electron flux is taken as the integral of the electron peak in the shower counter divided by the beam pions. This number is usually consistent, within rather large errors, with the counting rate in the Cerenkov counters. The final results are shown in Table 14.

Muon Contamination:

The muons in the beam arise mainly from decays in flight. The muon flux at the hydrogen target was determined by measuring the transmission of particles identified as pions (or kaons) by the beam Cerenkov counters through a 10' long steel block. This block was, in fact, the dipole magnet AVB3 which could be lifted into the beam (see Figure 9).

TABLE 13

Spectrometer Transmission

(Under each particle column 1 gives transmission with empty target in plane. Column 2 gives transmission with hydrogen target in place. Column 3 gives outscattering correction for π and P's. For K's the outscattering is already included. All numbers are in percent.)

Momentum	π	K	P
50	88.1-83.5-1.5	66.2-62.7	85.8-79.5-.5
70	90.7-86.5-0.9	76.7-73.9	90.1-83.5-.9
140	91.6-86.7-1.0	81.8-79.1	92.8-85.8-1.0
175	94.7-90.2-1.5	89.5-86	94.5-81.7-1.5

TABLE 14

Muon and Positron Contamination

Momentum	% μ's in 'pion' beam*	% hadron punch-through	% e^+ in 'pion' beam
50	1.3 ± .2	.2 ± .1	.8 ± .1
70	1.5 ± .1	.5 ± .05	1.0 ± .25
140	2.0 ± .3	.8 ± .2	1.0 ± .1
175	1.6 ± .3	2.7 ± .2	1.0 ± .1

*Error includes uncertainty in punch-through measurement.

A transmission counter (BT0 with its variable hole completely closed) counted the flux of particles passing through the steel. This flux has two components: i) genuine muons, ii) hadron punch-through - that is, complex hadronic showers which produce at least one particle that hits the transmission counter. The two contributions were separated by comparing the transmission of beam protons with the transmission of beam 'pions.' Since the punch-through involves very complicated cascades, we would expect it to be independent of the species of initiating hadron. Then the proton transmission can be taken as a measure of the punch-through. The muon flux is then:

$$\mu \text{ contamination of pions} = \text{'Pion transmission'} - \text{'Proton transmission'}$$

$$\mu \text{ contamination of kaons} = \text{'Kaon transmission'} - \text{'Proton transmission'}$$

The results are given in Table 14.

K^+ Decays in the Vicinity of the Target:

If a K^+ decays after it has been tagged, and still causes a beam trigger, it will also falsely contribute to the kaon flux. This effect is automatically compensated by the spectrometer transmission measurement which corrects the yield up for the apparent loss of this component of the beam. That this effect is negligible, is demonstrated by sending the flux of tagged beam kaons into the steel block to measure the muon transmission.

C. Removal of Electromagnetic Effects from the Cross Sections

Since the objective here is to measure elastic scattering due to the strong interaction, we must correct for two effects of the electromagnetic interaction: Coulomb scattering and radiation.

1. Coulomb Scattering Corrections:

Elastic Coulomb scattering is kinematically indistinguishable from hadronic elastic scattering. To correct for its contribution to the cross section, we use the formula due to Bethe

$$\frac{d\sigma}{dt}(x^{\pm}p) = F_c^2/t^2 \mp \frac{2F_c}{|t|} f_I \cdot (\alpha_{\pm}\cos\varepsilon \pm \sin\varepsilon) \qquad \text{(I)}$$

$$+ (1 + \alpha_{\pm}^2)\, f_I^2$$

where

i) $d\sigma/dt\ (x^{\pm}p)$ is the measured cross section for the process $x^{\pm}p \to x^{\pm}p$

ii) F_c is the amplitude for Coulomb scattering:

$$F_c = \frac{2\sqrt{\pi}}{137\beta} \frac{G_x(t)\, G_p(t)}{1 - |t|/4\, M_p^2} \qquad \text{(II)}$$

In this formula, β is the laboratory velocity of the incident projectile. $G_x(t)$ and $G_p(t)$ are the form factors of the particle x (π, k,p) and of the target proton respectively. The form factors are both taken to have the 'dipole form:'

$$G_x(t) = G_p(t) = \frac{1}{(1 + |t|/0.71)^2}$$

In this case,

$$F_c = \frac{0.01613/\beta}{(1 + |t|/0.71)^4} \; Mb^{1/2} \; GeV \qquad \text{(III)}$$

(Note that the $t/4 M_p^2$ in II is small and has been omitted from III).

iii) f_I is the imaginary part of the nuclear (hadronic) amplitude. In the small t region, the hadronic cross section is well approximated by an exponential in t so that

$$f_I = \frac{\sigma_{TOT}\ (x^{\pm}p)}{4.42} \; e^{Bt/2} \; (Mb/GeV^2)^{1/2}$$

iv) $\alpha_{\pm}$ is the real to imaginary ratio for (x,p) elastic scattering. It is assumed to be nearly t independent.

v) ε is the phase of the coulomb amplitude as calculated by Yennie and West.[24]

$$\varepsilon = -(\ell n\ B'|t| + 0.577)/137\beta$$

where

$$B' = 1/2\ B + 4\ GeV^{-2}$$

The three pieces of data required to compute the correction terms are the total cross-sections, the real to imaginary part ratio, and the forward elastic slope. The total cross sections are taken from Carroll et al.,[25,26] the real to imaginary parts are taken from various sources which are noted in Table 15. The slopes are taken

TABLE 15

Ratio of Real to Imaginary Parts of the Scattering Amplitude at t = 0

Protons: Taken from measurements of Ref. 23.

Momentum	Real/Imaginary
50	-.16
70	-.12
140	-.064
175	-.039

Pions: Taken from calculation of Ref. 29.

50	-.08
70	-.04
140	.00
175	+.02

Kaons: Taken from calculation of Ref. 29.

50	-.04
70	.00
140	+0.05
175	+0.07

from our own data and are the local logarithmic derivatives at $t = \sim.0$. A 20% change in the slope changes the already small corrections 20% leaving at most a 1/2% uncertainty in the final cross sections at low t.

2. Radiative Corrections

Particles which scatter from the protons of the target receive a momentum transfer. When charged particles receive such an impulse they can radiate energy. Under these circumstances, a particle which should have fallen inside of the cut used to select elastic events may actually fail the cut on the low momentum side. The calculated cross section will then be too low. The situation is shown schematically in Figure 31. One can show that the observed cross section is related to the true hadronic cross section by

$$\left.\frac{d\sigma(\theta)}{d\Omega}\right|_{true} = \left.\frac{d\sigma(\theta)}{d\Omega}\right|_{obs} \times e^{\delta(\Delta p)}$$

Where Δp is the distance of the momentum cut from the momentum p of a particle which has elastically scattered at the angle θ. The correction parameter δ is calculated by Sogard:[27]

$$\delta(\Delta p) = \frac{2\alpha}{\pi}\left(\frac{2\mu^2 - t}{Q} \ln\left(\frac{Q-t}{Q+t}\right) - 1\right) \ln\left(\frac{p}{\Delta p}\right)$$

$$Q = \sqrt{t^2 - 4\mu^2 t} \qquad (t < 0)$$

(α is the fine structure constant; μ is the mass of the scattered particle.)

Resolution effects (the fact that the peak is not a sharp line but is smeared by the momentum resolution) have not been specifically included but calculation has shown that they hardly influence the magnitude of the corrections.

Figure 31 EFFECT OF RADIATION ON ELASTIC YIELD

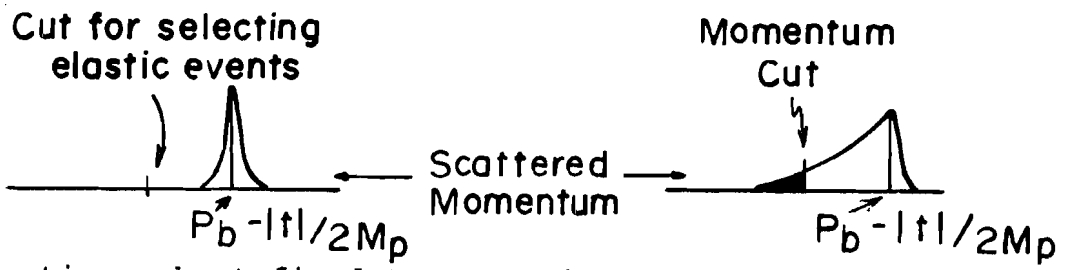

Elastic peak at fixed t. Radiation is turned off.

With radiation turned on, some elastic events radiate enough energy to fall outside the cut (shaded area). The yield inside the cut is too low.

D. Double Scattering Corrections:

A particle which has interacted once in the hydrogen target may interact a second time before it escapes. In this manner, two small angle scatters may simulate a larger angle scatter. The angular distribution of the double scatters is derived below and is shown to have an angular dependence which is different from the single scatters. Failure to remove the double scattering would, therefore, produce errors in the slope parameters of the differential cross section.

The effect of double scattering depends strongly on the shape of the single scattering cross section. The general formula is derived as follows:

Consider a hydrogen target of length ℓ and the coordinate system shown in Figure 32. The probability of a single scatter in the region dz around some point z of the target per unit solid angle $d\Theta_x d\Theta_y$ around Θ_x, Θ_y is

$$P_1(\Theta_x, \Theta_y)dz = n\rho_{\ell H_2} dz \times \frac{d\sigma}{d\Omega}(\Theta_x, \Theta_y)$$

The probability of a double scatter into Θ_x, Θ_y is given by

$$P_2(\Theta_x, \Theta_y)dz = \int_0^{\ell} dz_1 e^{-w_o z_1} \int_{-\infty}^{\infty} n \frac{d\sigma}{d\Omega}(\theta_x, \theta_y)d\theta_x d\theta_y$$

$$\times \int_{z_1}^{\ell} dz_2 \, e^{-w_o(z_2-z_1)} \, n \frac{d}{d\Omega}(\Theta_x-\theta_x, \Theta_y-\theta_y) \times e^{-w_o(\ell-z_2)}$$

where

$$w_o = n\rho_{\ell H_2} \sigma_{TOT}.$$

The extension of the angular integrations to infinity is valid if $d\sigma/d\Omega$ falls to zero very rapidly with angle. The z integrations are independent of the angular ones and produce the result

$$\frac{n^2\ell^2 e^{-w_o \ell}}{2}$$

If we suppose the function $\frac{d\sigma}{d\Omega}(\theta_x,\theta_y)$ factorizes, that is $\frac{d\sigma}{d\Omega}(\theta_x,\theta_y) = f(\theta_x)g(\theta_y)$, then we are left with integrals like

$$I(\Theta_x,\Theta_y) = \int_{-\infty}^{\infty} f(\theta_x)\, f(\Theta_x - \theta_x)d\theta_x \int_{-\infty}^{\infty} g(\theta_y)\, g(\Theta_y - \theta_y)d\theta_y .$$

For our purposes, the cross section can be adequately represented by a sum of Gaussians:

$$\frac{d\sigma}{d\Omega} = \frac{pp'}{\pi} A\, e^{-bpp'(\theta_x^2+\theta_y^2)} + \frac{pp'}{\pi} C\, e^{-dpp'(\theta_x^2+\theta_y^2)}$$

Straightforward evaluation of the resulting integrals yields the result

$$P_2(\phi_p) = \frac{n^2\ell^2}{2} e^{-w_o\ell} \frac{pp'}{\pi} \{\frac{A^2}{2b} e^{\frac{-bpp'\phi_p^2}{2}} + \frac{C^2}{2d} e^{\frac{-dpp'\phi_p^2}{2}}$$

$$+ \frac{2AC}{(d+b)} e^{-pp'(\frac{bd}{b+d})\phi_p^2} \}$$

The elastic cross sections have been fitted with a double gaussian and these fits have been used to generate the corrections. A further iteration of this procedure did not significantly change the results.

Figure 32. GEOMETRY OF A DOUBLE SCATTER: TWO SMALL ANGLE SCATTERS SIMULATE A LARGE ANGLE SCATTER

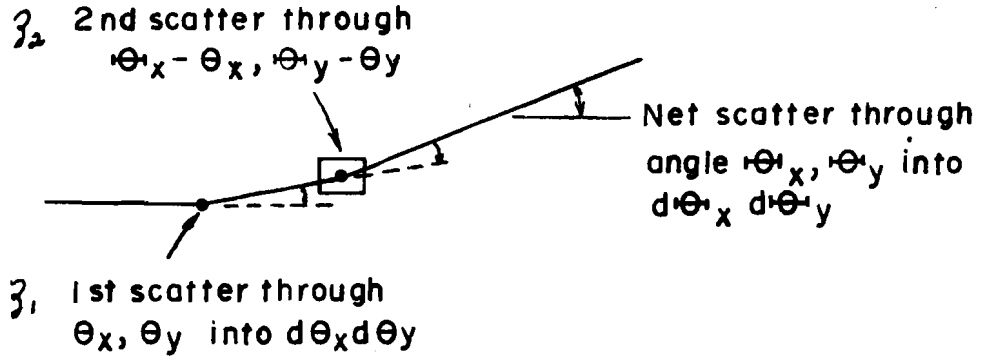

E. Correction for Inelastic Events Falling Inside Mass Cut:

At 50 and 70 GeV/c, the MM^2 resolution is sufficiently good so that we could study the inelastic spectrum down almost to inelastic threshold. We did this at several different t settings and found that at low t ($\lesssim .2$) the inelastic cross section for MM^2 near threshold behaved qualitatively like the elastic cross section. In fact, it appears that at $-t < .2$ GeV^2 the inelastic scattering has a slightly steeper angular dependence than the elastic. At higher t, ($t > .2$) the inelastic seems to fall less steeply than the elastic. The conclusion we reached was that a correction factor C(t) of the form

$$C(t) = 1\%, \qquad -t < .2$$

$$C(t) = 1\%\ e^{-3(t+.2)}, \quad -t > .2$$

gives a reasonable description of the inelastic background falling inside the mass cut for all particle types. The uncertainty is estimated to be $\sim$ 25% of the correction.

At 140 and 175 GeV/c, the MM^2 resolution is worse than at 50 and 70 GeV/c so we could not study the inelastic spectrum very close to inelastic threshold. However, the inelastic spectrum at slightly higher MM^2 had the same t dependence as the 50 and 70 GeV/c spectrum for this mass range. We concluded that the t dependence of the whole inelastic spectrum near threshold did not change much as the energy was changed from 50 to 175 GeV/c. We studied the ratio

$$\frac{d^2\sigma/dtdM^2\ (1.6 < MM^2 < 1.9) \text{ at } 140 \text{ GeV/c}}{d^2\sigma/dtdM^2\ (1.6 < MM^2 < 1.9) \text{ at } 70 \text{ GeV/c}}$$

to see if there was a change in the total number of events produced in this region as a function of energy. The ratio was ~ 1. Finally, we included a correction for the fact that the number of events from above the MM^2 cut which fall inside the cut due to resolution effects increases at 140 and 175 GeV/c due to the larger σ_{MM^2}. This smearing effect was calculated to be about 25%. Therefore, for 140 and 175 GeV/c:

$$C(t) = 1\text{-}1/4\%, \qquad -t < .2$$

$$C(t) = 1\text{-}1/4\%\ e^{3(t+.2)}, \qquad -t > .2$$

again with an uncertainty of 25%. At $t \sim .7$, $C \simeq 4 \pm 1\%$.

Summary of Corrections:

Table 16 is an attempt to give an overview of the significance of the various t-dependent corrections that have to be applied to the data. For 70 and 175 GeV/c, the radiative, Coulomb, double scattering, and inelastic background corrections are shown at a small t value, a medium t value, and a large t value. The radiative corrections are significant only for pions. The Coulomb corrections are never very important. At most, they contribute a few percent correction to the lowest t values for the cross sections for protons at 50 and 70 GeV/c (where the proton real part is $\sim$ 10%). Double scattering is important only for protons (because of the steep t dependence). The inelastic background correction is very small until $-t \sim .6$. In no case do these corrections greatly affect the data or any of the parameters determined from it.

TABLE 16

Typical Contributions of t-Dependent
Corrections to Differential Cross Sections

P (Momen.)	Particle	t	Radiative Correction C_r	Coulomb Correction C_c	Double Scattering Correction C_D	Inelastic Background C_I
70	π	.025	1.01	.98	.998	.99
		.4	1.05	1.0	.99	.98
		.66	1.07	1.0	.98	.96
	P	.026	1.00	.98	.996	.99
		.4	1.00	1.00	.978	.98
		.63	1.00	1.00	.943	.96
	K	.03	1.00	.985	1.00	.99
		.4	1.01	1.00	1.00	.98
		.65	1.02	1.00	.99	.96
175	π	.06	1.02	1.0	1.00	.9875
		.37	1.06	1.0	.99	.98
		.73	1.08	1.0	.98	.94
	P	.06	1.0	.997	.995	.9875
		.37	1.0	.999	.975	.98
		.73	1.0	.999	.92	.94
	K	.06	1.00	1.00	.998	.9875
		.37	1.01	1.00	.995	.98
		.67	1.02	1.00	.99	.95

$$\frac{d\sigma}{dt} = \left.\frac{d\sigma}{dt}\right|_{raw} \times C_r \times C_c \times C_D \times C_I$$

CHAPTER VIII

DISCUSSION OF SYSTEMATIC UNCERTAINTIES

A. Systematic uncertainties on the overall scale:

The major sources are:

1) the knowledge of the spectrometer transmission. The online measurements of transmission are self-consistent to a level of about 1%.* ± 1%

2) the uncertainty in the spectrometer solid angle. Online measurements of the transfer matrix elements at the focal plane (Section IV) agree with TRANSPORT to ∿ 2-3%. ± 2-3%

3) the uncertainty in the efficiencies of spectrometer detectors (MWPCs and Cerenkovs) 1%

4) uncertainties in the accidental corrections .2%

5) a whole host of small effects, e.g. the uncertainty in the muon and electron contamination, the absolute momentum calibration, the horizontal angle alignment of the beam and spectrometer. 1%

We have assigned an overall normalization uncertainty of ± 3% to the data due to systematic effects. This number is a compromise between adding the individual uncertainties listed above in quadrature and adding them linearly.

*Kaons at 50 and 70 GeV/c represent a special case. At 50 GeV/c, ∿ 1/3 of the kaons decay in the spectrometer. The details of which decays appear as elastic scatters and which trigger but are not counted as elastic scatters is complex. There is a resulting scale uncertainty of 3% for kaons due to these effects.

B. Systematic Errors Affecting the t-Scale

1) We have stated that the AVB field strength is known to ∿ 1/4%. The resulting t-scale uncertainty is twice this. 1/2%

2) The alignment between the beam and the spectrometer is measured by the beam hodoscope. The measurement of the vertical angle at the target is especially important. We estimate that the granularity of the hodoscope permits the determination of the alignment to only a few hundredths of a milliradian. This produces uncertainties of ∿ 1/2% in the t-scale. 1/2%

3) In order for AVB+ and AVB- runs to average to the correct answer, the y-hodoscope must be moved exactly the correct amount. We were only able to verify the y-hodoscope calibration of 127 mils/mr to about 1%. This contributes another ∿ 1/2% uncertainty to the t-scale. 1/2%

4) Small missettings of the AVB current or the y-hodoscope position have not been fixed in the analysis. Occasional small wanderings of the field probe which monitored the AVB also occurred. 1/4%

On the basis of the above remarks we assign an overall uncertainty of ∿ 1.5% to the t-scale.

The implications of a 1.5% uncertainty in the t-scale are: 1) linear slope parameters of the differential cross section have a 1.5% systematic uncertainty. 2) individual cross section points will have systematic fractional errors of ∿ $b\Delta t$ where Δt is the absolute uncertainty in t and b is the local logarithmic derivative. At $t = .7$, $\Delta t = .01$. For $b(.7) \sim 6\text{-}8$, the error is 6-8%.

C. Point-to-Point Systematic Errors:

If the size of the vertical angle bins is incorrect due to an error in the knowledge of a transfer matrix coefficient, each bin except the central one is at a slightly different t-value than the nominal one. The t-value of the central bin is fixed by the AVB field. As long as several overlapping central AVB angle settings are taken, the overall t-scale is fixed and the average shape of the angular distribution is correct. Individual points not at the central setting will be in error. Figure 33 shows how an error in the size of a vertical angle bin affects the data. At high energies the measurement is very sensitive to this kind of effect. We have reduced these errors by dropping a few angle bins at each extreme of the acceptance at each angle setting since the effect is largest there. In the remaining overlap regions between two settings the effects pull the cross sections in opposite directions so cancellation occurs. The low-t side of the lowest angle setting and the high-t side of the highest angle setting are uncompensated by overlaps with other runs. We have not reported cross sections for these points.

We have checked for point-to-point errors due to nonuniform efficiency of spectrometer detectors. All such effects are well below the 1% level. Occasionally, binning effects cause glitches in the data. These are known to be binning effects because they disappear when the binning structure is changed very slightly. Usually such points are reported without alteration. If they make unreasonable contributions to the χ^2 of fits they are either eliminated or averaged with nearby points.

D. Systematic errors arising from uncertainties in Coulomb, radiative, double scattering, and inelastic background corrections.

1) Coulomb corrections are significant only near $-t \sim .02$. They are computed to an accuracy of $\sim$ 25%. The uncertainties are due to the knowledge of the real parts and to the question of which slope to choose for the nuclear amplitude.

2) The radiative corrections are the biggest correction for pions at large t. They should be accurate to better than 5% of their value.

3) It is hard to estimate the inaccuracy introduced into the correction due to the choice of the double gaussian to approximate the data. The correction is significant only for protons. From a comparison with a Monte Carlo calculation, we know that it is good to at least $\sim$ 10% of its value. At high t, for protons this implies a contribution of 1% to the overall uncertainty.

4) Inelastic background is about 3-4% at the largest t values. We have assigned an error of 25% of the value. Thus, even at large t it contributes only 1% to the overall uncertainty.

Summary: The main conclusions are:

1) the absolute normalization is known to $\pm$ 3%.

2) the absolute t-scale is known to $\pm$ 1.5%.

3) the point-to-point systematic errors are dominated by our knowledge of the local (within a single spectrometer setting) t-scale.

4) The physics corrections do not contribute to the uncertainty at more than $\sim$ 2% level even at large t.

5) The uncertainty in the t-scale can systematically shift the high t ($-t \simeq .7$) points by $\sim$ 6%.

Figure 33: Effect of a small error in the differential t-scale

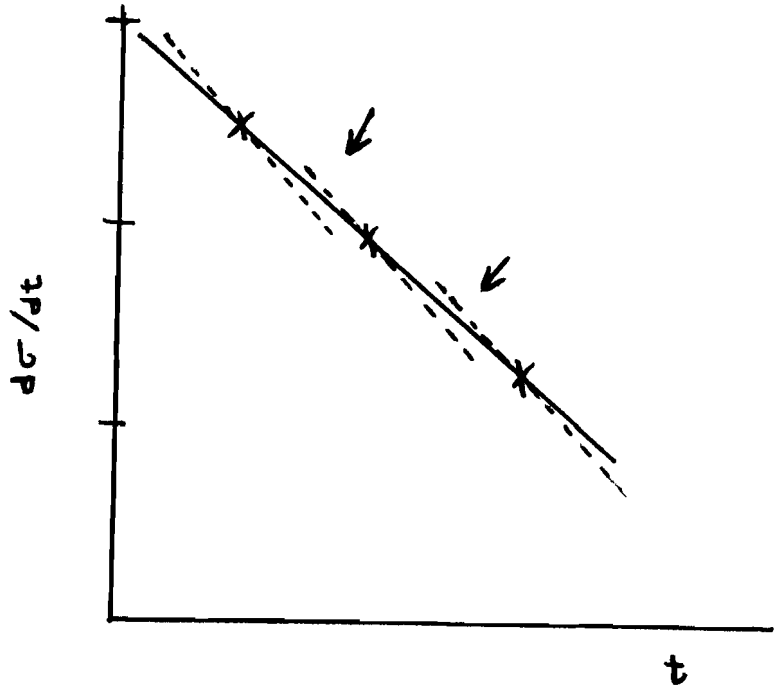

1) x = Central bins of each angle setting
2) Solid curve is true cross section
3) Dashed lines represent data points if the angle calibration within the spectrometer bite is wrong
4) Arrows point to region where errors cancel

CHAPTER IX

RESULTS

The cross sections for π^+P, K^+P and PP elastic scattering at 50, 70, 140, and 175 GeV/c are plotted in Figures 34a, b, c, and d. The error bars reflect statistical uncertainties only. All the data points in these plots are tabulated in Appendix I. The absolute normalization of the data is discussed below. Table 17 presents the same data grouped into coarser t-bins. The smooth curves superimposed on the plots are calculated from the fits described below.

The data is not well represented by a 'simple exponential', $d\sigma/dt = A\ e^{Bt}$, but can be represented by a 'quadratic exponential', $d\sigma/dt = A\ e^{Bt+Ct^2}$. Table 18 presents the results of these fits. In addition to A, B, and C and their statistical errors, the following quantities are given in the table: the t-interval of the fitted data; the off-diagonal elements σ_{AB}, σ_{AC}, and σ_{BC} of the error matrix of the fitted parameters; the chi-square of the fit divided by the number of degrees of freedom, χ^2/degf; the probability in percent of obtaining a χ^2 larger than this if the parameterization is correct and the uncertainties are only statistical in nature; the logarithmic derivative $b(t) = d/dt(\ell n\ d\sigma/dt) = B + 2Ct$ evaluated at $-t = .2$ GeV^2 and its uncertainty (the error quoted on this quantity includes a 1-1/2% systematic error added in quadrature to the statistical error); and b(-.2) determined from a fit to data points with t-values less than .4 only. Under each A value, the Optical Theorem Point (OTP) is given for that energy and reaction.

The absolute normalization of the data was checked by comparing the A-parameter from fits of the kind presented in Table 18 with optical theorem predictions using the total cross section measurements of Ref. 25 and 26 and the real parts of Table 15. On the average, the A-parameter was lower than the optical point by $\sim$ 3%. This result agrees with the observation that the online calibration of the solid angle described in Section IV generally indicated that the true solid angle was slightly smaller than the solid angle obtained from TRANSPORT, which was used in the analysis. The accuracy of these calibration measurements was, unfortunately, insufficient to give quantitative correction factors for each energy.

We recognize also that some of the apparent normalization error could come from the extrapolation of the data to t = 0.0 by means of the fit. In the first place, A, B, and C are heavily correlated so that a small shift in B would improve agreement with the optical point while causing only a slight degradation of the χ^2. In the second place, if the fitting function is inappropriate - for example, if there are breaks in the cross sections at low t - that could bias the comparison. We also recognize that normalization problems can arise from many sources so that there may not be a single overall normalization error associated with all reactions at all the energies.

Despite the problems considered above, the best conclusion we can draw from the available information is that there is a 3% normalization error which is applicable to all reactions at all energies. This error almost certainly comes from an error in the solid angle. We have shown that such an error will not affect the average shape of the differential cross section although (if part of it is associated

with the vertical angle) it will be a source of point-to-point systematic errors. We have, therefore, applied a correction factor of 1.03 to all measured cross sections which are presented in Appendix I. When this correction factor is applied, nine of the A-parameters fall within one standard deviation of the optical point and three fall within two standard deviations. This is a very acceptable result. The residual systematic error on the scale from effects other than the solid angle should be of the order of 1%. Figure 35 presents the comparison of A parameters of Table 18 with the optical points.

Figure 36a, b, and c present comparisons of the B and C parameters of our data with those determined from other experiments. Since the values of A, B, and C from the fit are highly correlated and depend on the t-range of the fits, such comparisons have only limited validity.

The quantity b(-.2) is a better quantity to use for comparing the shape of the cross sections obtained from different experiments. It is a local property of the cross section and is, therefore, less sensitive to the t-interval of the fit than B or C. Also, B and C have a positive correlation; as B gets larger, C also gets larger ($t \leq 0.0$) so that b(-.2) tends to stay the same. Figure 37 presents a comparison of b(-.2) from our data with the same quantity measured in other experiments. In general, our proton data smoothly interpolates the Serpukhov and ISR data and the π^+P and K^+P data join smoothly onto data from lower energies.

The b(-.2) determined only from points with $-t < .4$ is included in Table 18 to show that this quantity is not influenced by the high-t points which have large systematic errors. It can similarly be shown

b(-.2) is not strongly influenced by the few lowest t points which may also have additional systematic errors.

Table 19 shows the results of an alternative parameterization of the data.* We have used a 'simple exponential' to fit the region between $-t = .02$ and $-t = .10$ and another simple exponential to fit the region between $.15 < -t < .50$. This parameterization is motivated by the observations of Carrigan[29] on the possibility of a break (abrupt change in slope) in pp scattering at Brookhaven energies and by the measurements of Reference 15 on PP elastic scattering at ISR energies. We have not presented fits for the low t region at 175 GeV/c because the t-range extends only to .06 GeV^2 and there are insufficient statistics between there and .10 to get a meaningful slope. This parameterization of the 50, 70, and 140 Gev/c data by two simple exponentials seems also to represent the data quite well.

The difference between the B parameter for the low t region and the B parameter for the high t region is $\sim$ 1.5-2.0 GeV^{-2} for both protons and pions. These differences are consistent with the changes of slope implied by $C \sim 2$ to 3 GeV^{-4} obtained from the fits to the quadratic exponential. Additional comments are made concerning these two parameterizations in the next section.

The differential cross section $d\sigma/dt$ can be integrated to give the total elastic cross section σ_{el}. Since we have measured the cross sections only between $-t \gtrsim .05$ and $-t \lesssim .7$ (.8 in some cases), we must extrapolate the low t data to $t = 0.0$ and the high t data to the kinematic limit on t (effectively to infinity). The extrapolation to large

*For these fits we have removed the scale factor of 1.03. We wished to see if this parameterization improved the agreement with the optical points. The statistical accuracy is insufficient to draw firm conclusions.

t is not critical. $d\sigma/dt$ has fallen by over two orders of magnitude at $-t = .7$ and very little of the total elastic cross section comes from the region beyond this. The extrapolation to small t is more critical since an appreciable part of σ_{el} comes from this region. We have performed a numerical integration of the quadratic exponential fit of Table 18:

$$\sigma_{el} = A \int_0^{.8} e^{-B|t| + C|t|^2}$$

The results are given in Table 20. The uncertainties are the quadrature of the statistical errors and the estimated systematic error of $\sim$ 3%.

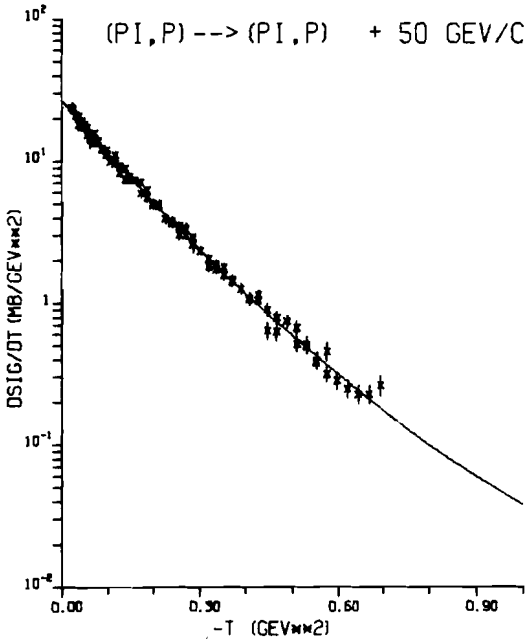

$26.57\ e^{8.70t + 2.14t^2}$

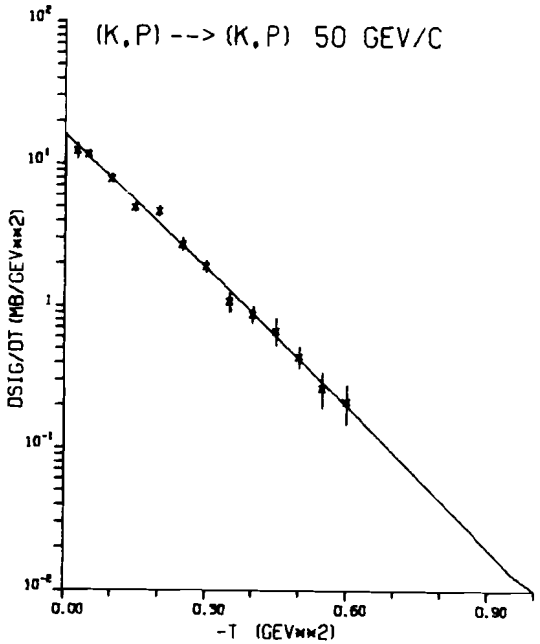

$16.10\ e^{7.15t - 0.32t^2}$

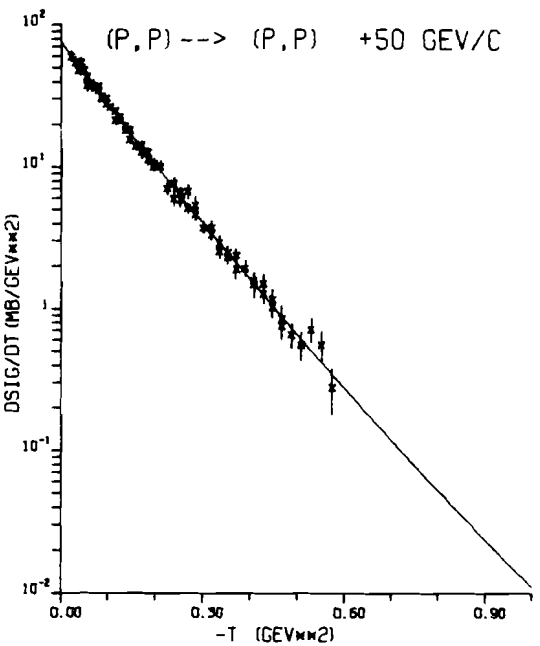

$75.14\ e^{10.15t + 1.33t^2}$

Figure 34a:
Elastic Cross Sections at
50 GeV/c

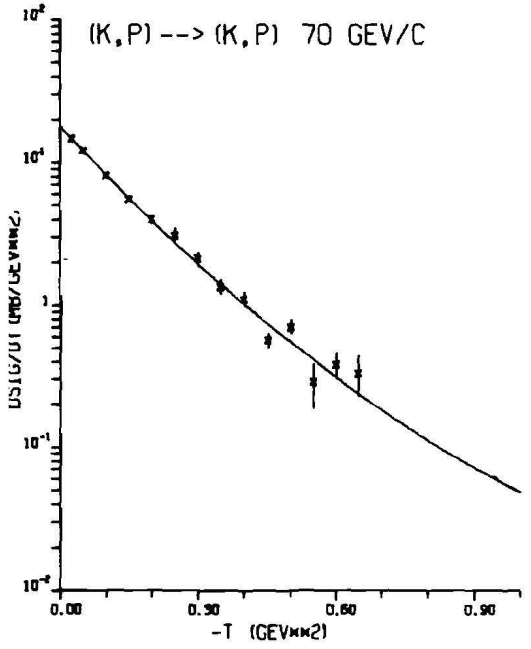

$17.70\ e^{7.88t + 1.77t^2}$

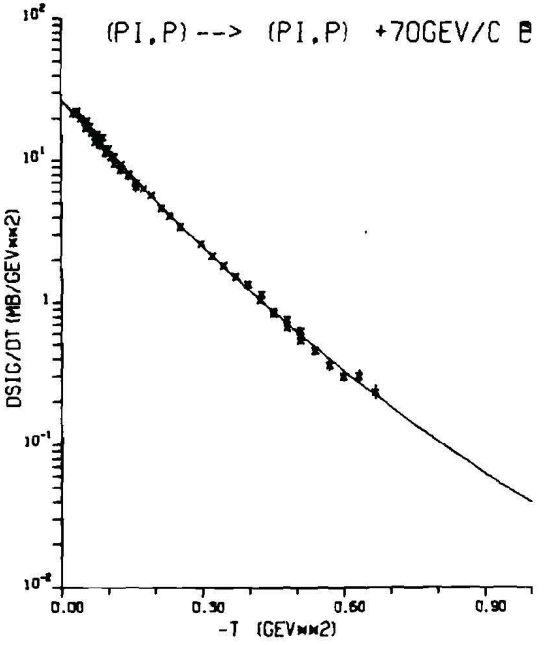

$26.90\ e^{8.57t + 2.04t^2}$

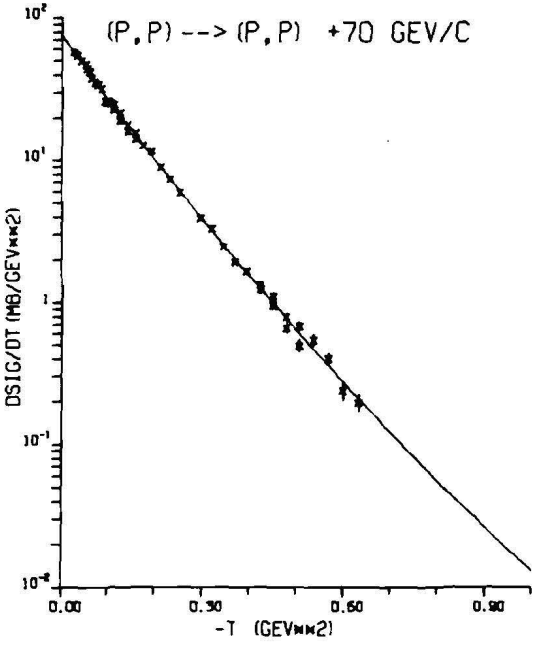

$75.30\ e^{10.45t + 1.78t^2}$

Figure 34b:
Elastic Cross Sections at
70 GeV/c

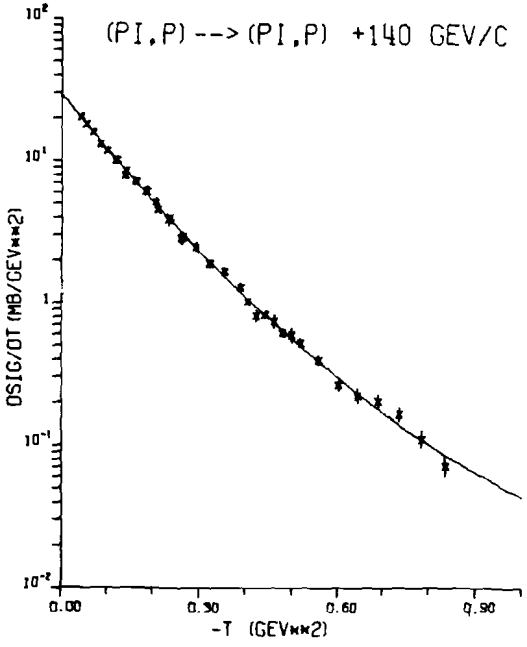

$29.40\ e^{9.33t + 2.80t^2}$

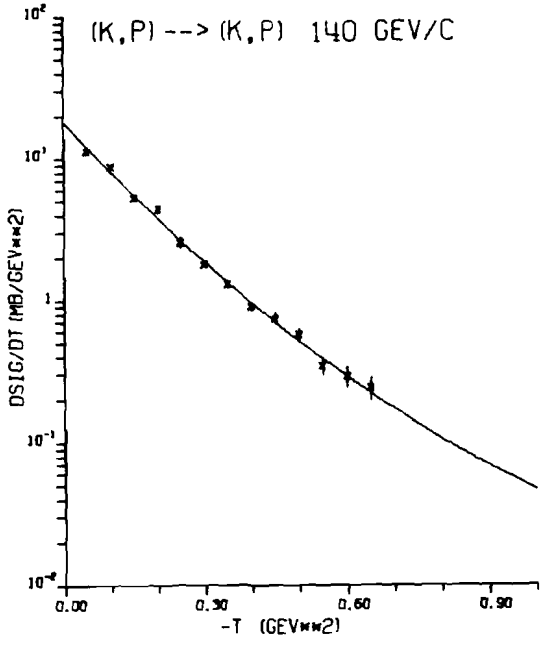

$18.06\ e^{8.24t + 2.24t^2}$

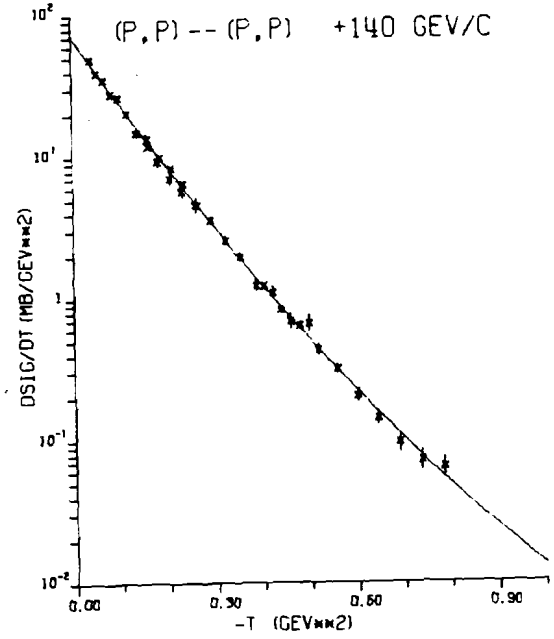

$72.93\ e^{11.23t + 2.61t^2}$

Figure 34c:
Elastic Cross Sections at
140 GeV/c

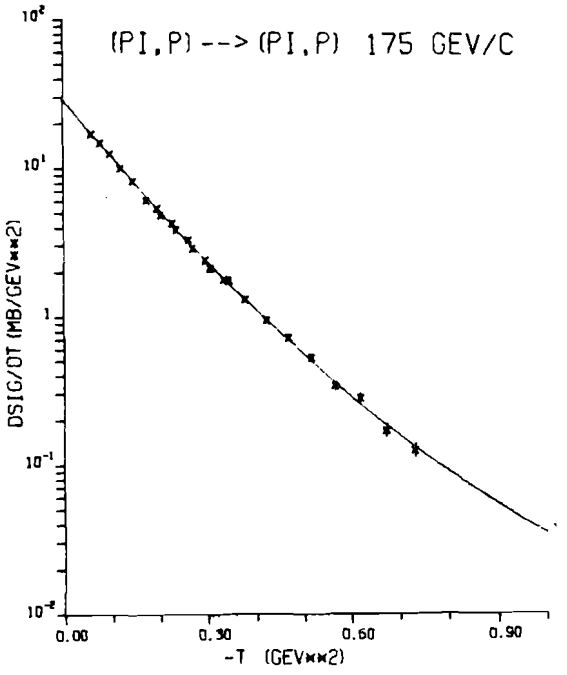

$29.10\ e^{9.14t + 2.38t^2}$

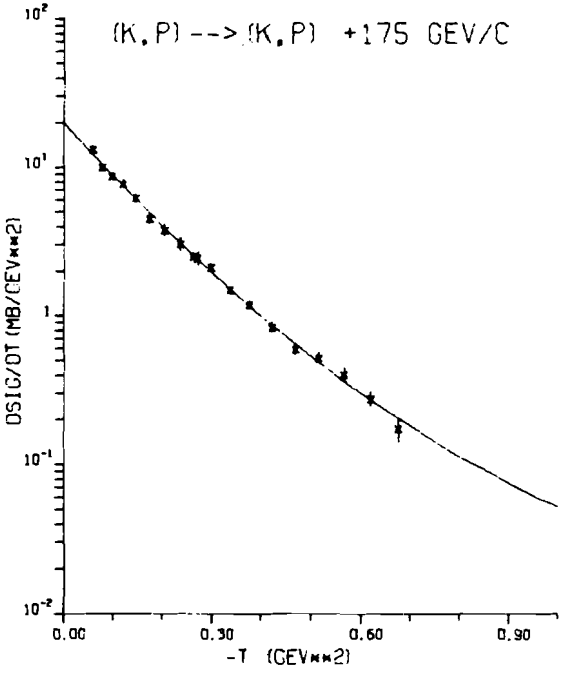

$19.92\ e^{8.58t + 2.63t^2}$

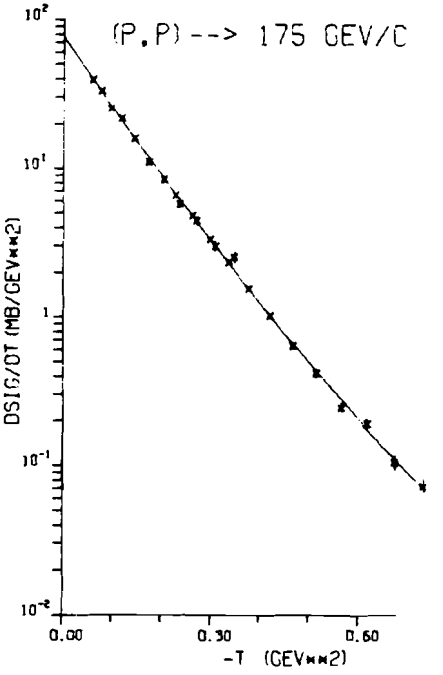

$76.00\ e^{11.21t + 2.25t^2}$

Figure 34d:
Elastic Cross Sections at
175 GeV/c

Table 17: DIFFERENTIAL CROSS SECTIONS FOR ELASTIC SCATTERING

PI,P 50 GEV/C

T GEV**2	DSIG/DT MB/GEV**2	ERROR
0.02	22.23	0.75
0.05	17.39	0.30
0.10	11.23	0.18
0.15	7.48	0.13
0.20	5.11	0.13
0.25	3.48	0.09
0.30	2.36	0.07
0.35	1.65	0.05
0.40	1.14	0.06
0.45	0.83	0.04
0.50	0.63	0.04
0.55	0.41	0.02
0.60	0.28	0.03
0.65	0.23	0.02
0.70	0.25	0.04

(K,P)-- (K,P) 50 GEV/C

T GEV**2	DSIG/DT MB/GEV**2	ERROR
0.02	12.22	1.49
0.05	11.60	0.56
0.10	7.81	0.46
0.15	4.90	0.34
0.20	4.63	0.37
0.25	2.70	0.26
0.30	1.89	0.18
0.35	1.07	0.16
0.40	0.86	0.11
0.45	0.66	0.14
0.50	0.44	0.07
0.55	0.26	0.07
0.60	0.21	0.07

(P,P)-- (P,P) 50 GEV/C

T GEV**2	DSIG/DT MB/GEV**2	ERROR
0.02	57.96	3.08
0.05	45.00	0.74
0.10	27.92	0.34
0.15	16.56	0.37
0.20	10.47	0.29
0.25	6.58	0.24
0.30	3.98	0.19
0.35	2.44	0.12
0.40	1.67	0.13
0.45	1.03	0.08
0.50	0.59	0.09
0.55	0.50	0.07

(PI,P)-- (PI,P) 70 GEV/C

T GEV**2	DSIG/DT MB/GEV**2	ERROR
0.02	23.06	0.90
0.05	17.98	0.33
0.10	11.54	0.21
0.15	7.55	0.11
0.20	5.24	0.10
0.25	3.52	0.11
0.30	2.50	0.05
0.35	1.76	0.04
0.40	1.28	0.03
0.45	0.83	0.02
0.50	0.62	0.02
0.55	0.41	0.02
0.60	0.30	0.02
0.65	0.27	0.02

(K,P)-- (K,P) 70 GEV/C

T GEV**2	DSIG/DT MB/GEV**2	ERROR
0.02	14.71	0.95
0.05	12.04	0.50
0.10	8.12	0.28
0.15	5.57	0.26
0.20	4.01	0.25
0.25	3.10	0.36
0.30	2.12	0.25
0.35	1.36	0.15
0.40	1.11	0.12
0.45	0.57	0.07
0.50	0.70	0.08
0.55	0.28	0.10
0.60	0.38	0.08
0.65	0.33	0.10

(P,P)-- (P,P) 70 GEV/C

T GEV**2	DSIG/DT MB/GEV**2	ERROR
0.02	58.75	1.99
0.05	44.86	0.63
0.10	26.91	0.40
0.15	16.17	0.23
0.20	10.25	0.21
0.25	6.09	0.20
0.30	3.91	0.09
0.35	2.33	0.06
0.40	1.57	0.04
0.45	1.01	0.04
0.50	0.60	0.02
0.55	0.47	0.03
0.60	0.24	0.03
0.65	0.17	0.02

(PI,P)-- (PI,P) 140 GEV/C

T GEV**2	DSIG/DT MB/GEV**2	ERROR
0.05	18.75	0.42
0.10	11.63	0.31
0.15	7.73	0.16
0.20	5.19	0.12
0.25	3.38	0.10
0.30	2.30	0.10
0.35	1.72	0.11
0.40	1.07	0.04
0.45	0.78	0.04
0.50	0.56	0.02
0.55	0.42	0.03
0.60	0.27	0.03
0.65	0.21	0.02
0.70	0.19	0.02
0.75	0.15	0.02
0.80	0.13	0.01
0.85	0.07	0.01

(K,P)-- (K,P) 140 GEV/C

T GEV**2	DSIG/DT MB/GEV**2	ERROR
0.05	11.15	0.57
0.10	8.73	0.34
0.15	5.32	0.28
0.20	4.37	0.25
0.25	2.57	0.22
0.30	1.78	0.08
0.35	1.32	0.07
0.40	0.91	0.07
0.45	0.74	0.06
0.50	0.57	0.05
0.55	0.34	0.05
0.60	0.29	0.05
0.65	0.24	0.05

(P,P)-- (P,P) 140 GEV/C

T GEV**2	DSIG/DT MB/GEV**2	ERROR
0.05	43.11	0.88
0.10	24.60	0.64
0.15	13.61	0.27
0.20	8.56	0.19
0.25	5.36	0.15
0.30	3.25	0.13
0.35	2.05	0.14
0.40	1.27	0.04
0.45	0.76	0.04
0.50	0.54	0.02
0.55	0.34	0.03
0.60	0.21	0.02
0.65	0.14	0.02
0.70	0.09	0.01
0.75	0.08	0.01

(PI,P)-- (PI,P) 175 GEV/C

T GEV**2	DSIG/DT MB/GEV**2	ERROR
0.05	18.27	0.40
0.10	12.09	0.15
0.15	7.62	0.15
0.20	5.03	0.11
0.25	3.50	0.05
0.30	2.28	0.05
0.35	1.59	0.04
0.40	1.09	0.03
0.45	0.79	0.03
0.50	0.58	0.03
0.55	0.37	0.02
0.60	0.31	0.02
0.65	0.19	0.02
0.75	0.11	0.01

(K,P)-- (K,P) 175 GEV/C

T GEV**2	DSIG/DT MB/GEV**2	ERROR
0.05	14.05	0.74
0.10	8.53	0.28
0.15	5.67	0.29
0.20	3.84	0.32
0.25	2.71	0.10
0.30	2.07	0.10
0.35	1.34	0.07
0.40	0.98	0.05
0.45	0.65	0.06
0.50	0.56	0.05
0.55	0.44	0.04
0.60	0.30	0.03
0.65	0.19	0.03

(P,P)-- (P,P) 175 GEV/C

T GEV**2	DSIG/DT MB/GEV**2	ERROR
0.05	44.03	0.73
0.10	25.65	0.47
0.15	14.56	0.35
0.20	8.54	0.38
0.25	5.27	0.05
0.30	3.22	0.06
0.35	2.07	0.04
0.40	1.24	0.03
0.45	0.75	0.03
0.50	0.48	0.03
0.55	0.28	0.02
0.60	0.23	0.02
0.65	0.13	0.01
0.75	0.06	0.01

Table 18: Results of fits to $d\sigma/dt = Ae^{Bt + Ct^2}$

Reaction Energy	t - range	A ± δA	B ± δB	C ± δC	σ_{AC}	σ_{AB}	σ_{BC}	$\chi^2/Degf$ (P(χ^2)) %	b (-.2) ± Δb (-.2)	b (-.2) ± Δb (-.2) -t ≤ .4
50 π^+p	.021-.692	26.57±0.49	8.70±.18	2.14±0.32	0.12	-0.08	-0.06	83.6/77 (28)	7.85±.14	7.82±.14
	OTP = 27.4									
70 π^+p	.026-.665	26.90±0.52	8.57±.17	2.04±0.29	0.12	-0.08	-0.05	62.7/42 (02)	7.76±.13	7.74±.14
	OTP = 27.4									
140 π^+p	.042-.834	29.40±0.69	9.33±.19	2.80±0.27	0.14	-0.11	-0.048	23.9/34 (90)	8.21±.15	8.10±.18
	OTP = 28.0									
175 π^+p	.059-.731	29.10±0.55	9.14±.15	2.38±0.25	0.11	-0.08	-0.036	20.2/21 (51)	8.18±.14	8.20±.14
	OTP = 28.5									
50 pp	.021-.574	75.14±1.60	10.15±.28	1.33±0.64	0.81	-0.40	-0.17	55.7/67 (84)	9.62±.17	9.65±.19
	OTP = 76.2									
70 pp	.026-.632	75.30±1.3	10.45±.19	1.78±0.36	0.38	-0.22	-0.06	60.5/41 (03)	9.74±.16	9.75±.16
	OTP = 75.75									
140 pp	.042-.736	72.93±1.74	11.23±.20	2.61±0.32	0.44	-0.32	-0.062	42.7/32 (10)	10.19±.18	10.17±.20
	OTP = 76.3									
175 pp	.059-.731	76.00±1.54	11.21±.16	2.25±0.27	0.32	-0.22	-0.04	29.1/20 (09)	10.31±.17	10.28±.17
	OTP = 76.8									
50 K^+p	.023-.608	16.10±1.00	7.15±.68	-0.32±1.33	1.02	-0.60	-0.86	93.5/88 (37)	7.28±.26	7.41±.30
	OTP = 16.6									
70 K^+p	.029-.648	17.70±0.85	7.88±.55	1.77±1.03	0.71	-0.42	-0.54	44.9/37 (17)	7.17±.22	6.95±.27
	OTP = 17.2									
140 K^+p	.042-.645	18.06±0.91	8.24±.43	2.24±0.74	0.53	-0.35	-0.31	48.1/33 (04)	7.34±.20	7.36±.21
	OTP = 18.9									
175 K^+p	.059-.674	19.92±0.91	8.58±.36	2.63±0.59	0.42	-0.30	-0.20	11.4/16 (79)	7.53±.19	7.52±.20
	OTP = 19.7									

Figure 35. COMPARISON OF A PARAMETER FROM FIT OF TABLE 18 WITH OPTICAL THEOREM PREDICTION

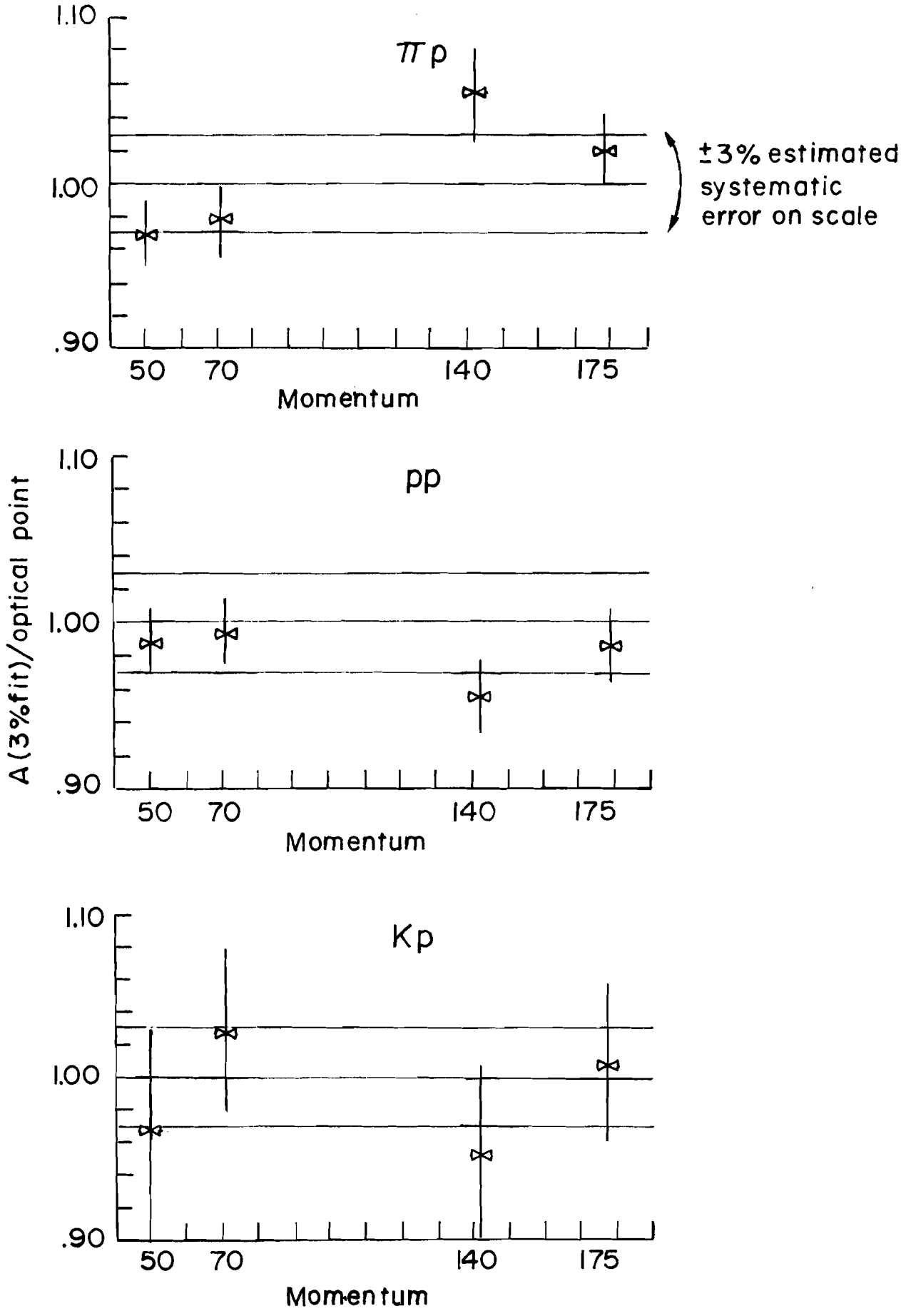

Figure 36. S Dependence of Slope Parameters B and C

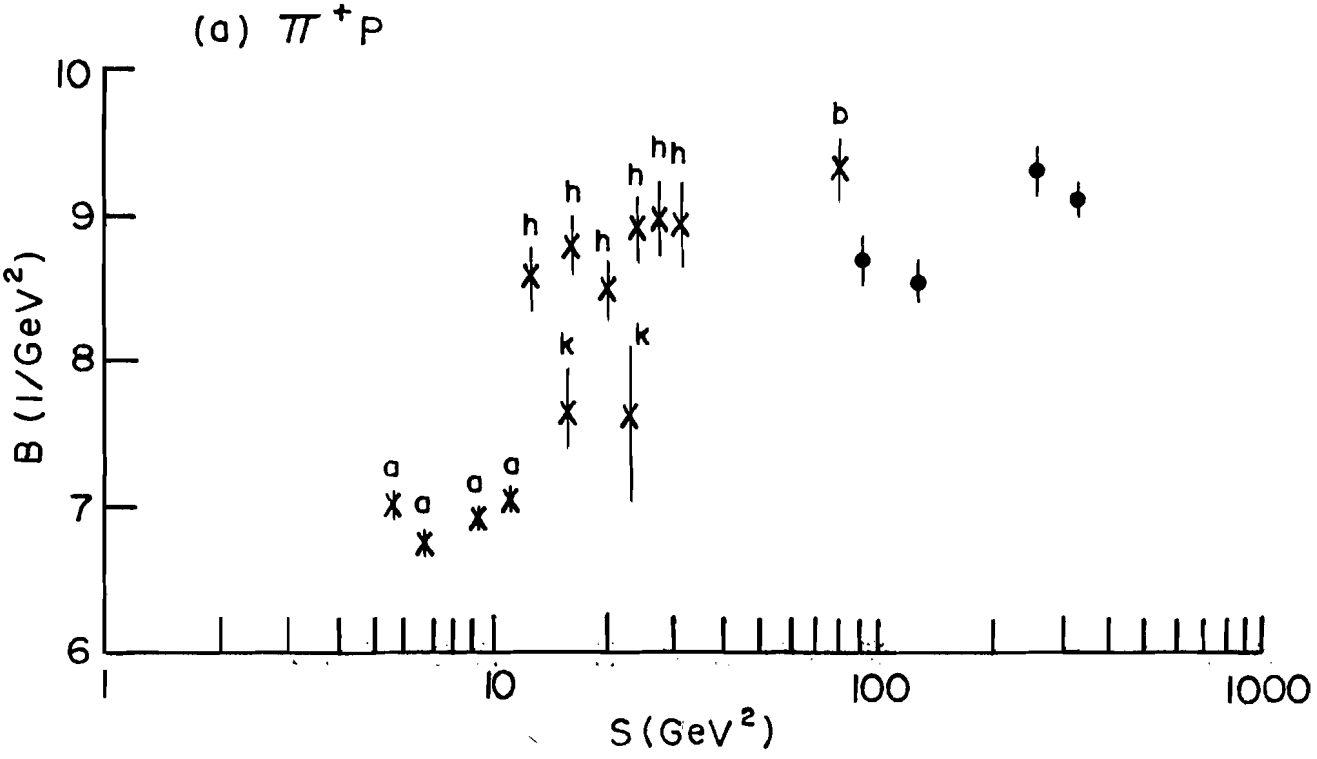

• This experiment

x Previous experiment. Letters refer to subitems of ref. 14

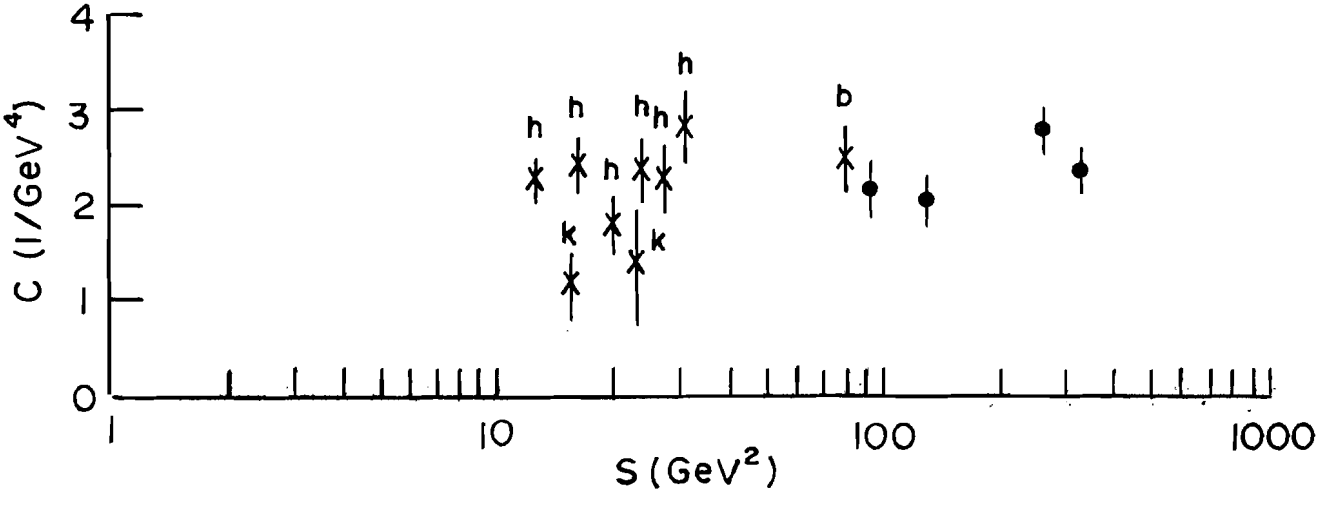

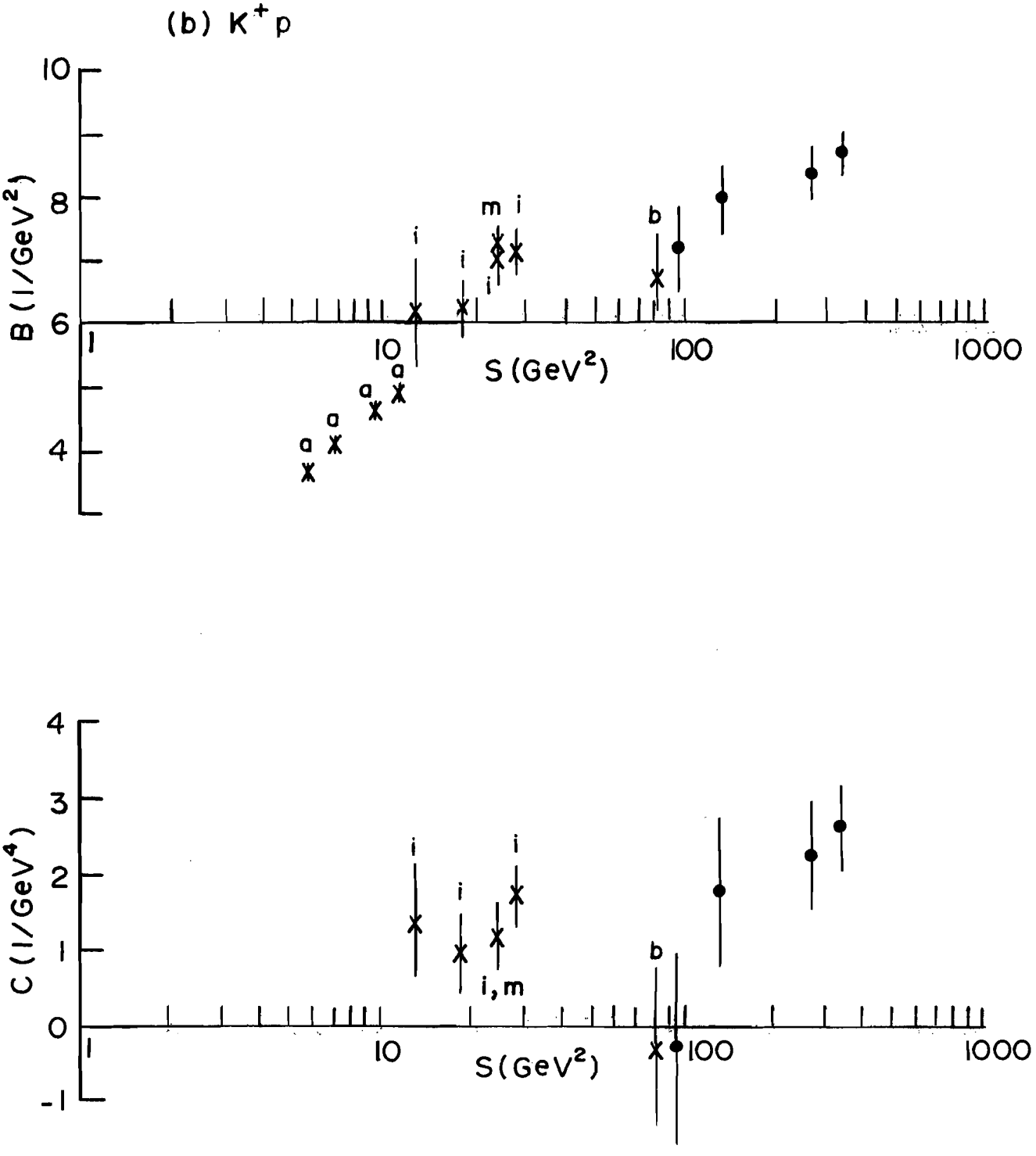
(b) K⁺p
B (1/GeV²)
S (GeV²)
C (1/GeV⁴)
S (GeV²)

(c) pp

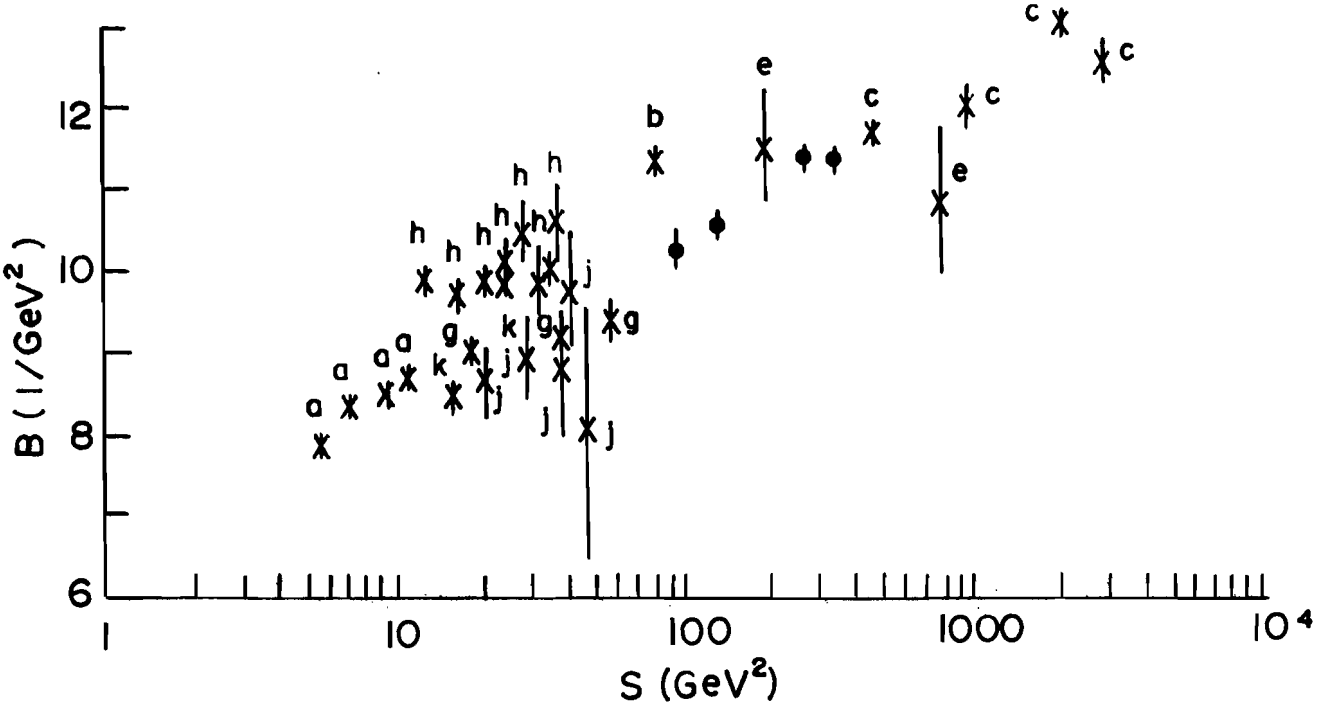
B (1/GeV²)
12
10
8
6
1
10
100
1000
10⁴
S (GeV²)

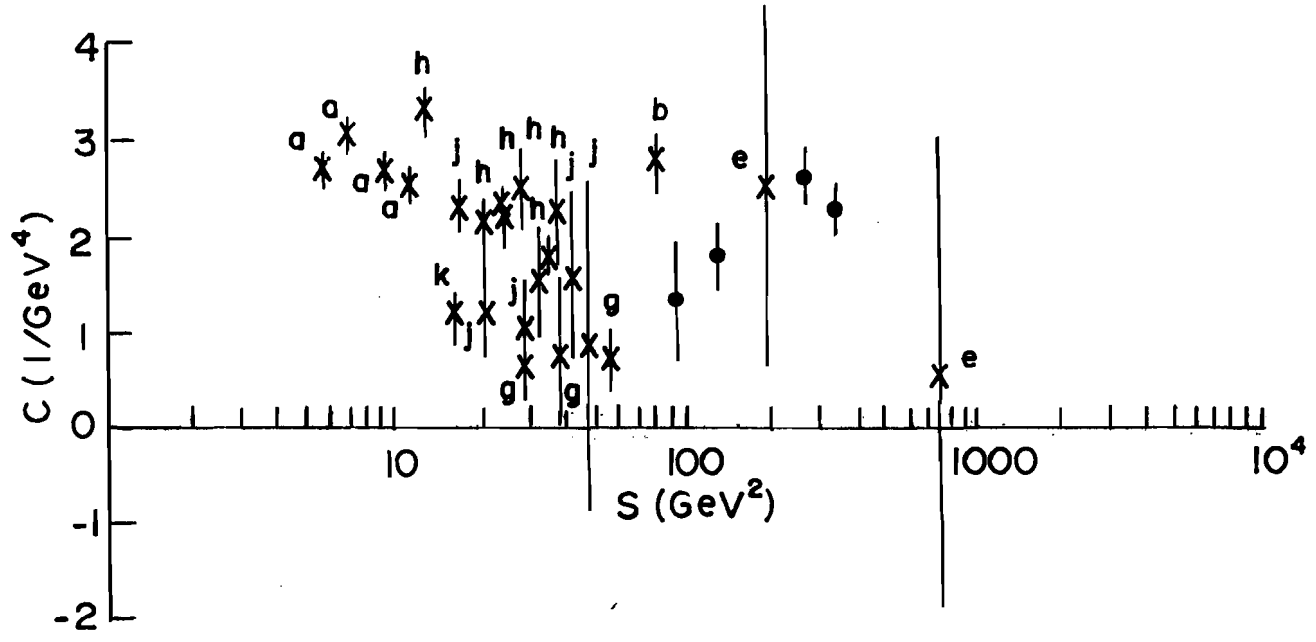
C (1/GeV⁴)
4
3
2
1
0
-1
-2
10
100
1000
10⁴
S (GeV²)

Table 19: Results of fits to Ae^{Bt} for pions and protons

Energy Reaction	t-interval	A ± δA	B ± δB	χ^2/degf	P(χ^2)
50 π^+p	.15-.50	22.2±0.9	7.47±.14	40.1/35	25.0%
70 π^+p	.15-.50	21.0±0.6	7.19±.09	16.3/16	43.0%
140 π^+p	.15-.50	23.6±0.8	7.75±.12	16.1/18	58.0%
175 π^+p	.15-.50	22.5±0.7	7.61±.11	11.9/12	45.0%
50 π^+p	.02-.10	27.1±1.1	9.20±.58	12.7/19	85.0%
70 π^+p	.02-.10	27.6±1.3	9.11±.68	20.0/11	4.6%
140 π^+p	.02-.10	29.3±1.9	9.57±.93	1.2/3	76.0%
50 pp	.15-.50	65.5±3.4	9.37±.20	24.9/36	92.0%
70 pp	.15-.50	64.3±1.9	9.45±.10	20.4/16	20.0%
140 pp	.15-.50	55.0±1.8	9.47±.12	22.1/18	23.0%
175 pp	.15-.50	56.8±1.8	9.62±.11	8.0/11	71.0%
50 pp	.02-.10	70.3±2.6	9.44±.53	15.0/17	60.0%
70 pp	.02-.10	76.0±2.8	11.09±.53	10.1/11	52.0%
140 pp	.02-.10	73.5±4.4	11.26±.88	6.6/3	8.5%

Table 20: Total Elastic Cross Sections and Tests of Geometric Scaling Hypothesis

Energy Reaction	$\sigma_{el} \pm \Delta\sigma^{*}_{el}$ (mb)	σ_{TOT} (mb)	$\sigma_{inel} \pm \Delta\sigma_{inel}$ (mb)	$\frac{\sigma_{el}}{\sigma_{TOT}}$	$\frac{\sigma^3_{TOT}}{\sigma_{el}{}^2}$ (mb)	B** (GeV^{-2})	B/σ_{TOT} (GeV^{-2})/mb
50 π^+p	3.25±.10	23.07	19.82±.10	.141±.004	1162±71	8.70±.22	.377±.010
70 π^+p	3.33±.10	23.16	19.83±.10	.144±.004	1120±67	8.57±.21	.370±.009
140 π^+p	3.39±.11	23.43	20.04±.10	.145±.004	1120±67	9.33±.23	.398±.010
175 π^+p	3.39±.10	23.60	20.21±.10	.144±.004	1144±68	9.14±.20	.387±.008
50 pp	7.60±.38	38.14	30.54±.38	.199±.010	961±96	10.15±.31	.266±.008
70 pp	7.45±.23	38.24	30.79±.23	.195±.006	1007±62	10.45±.25	.273±.007
140 pp	6.79±.22	38.57	31.78±.22	.176±.006	1244±80	11.23±.26	.291±.007
175 pp	7.04±.23	38.76	31.72±.23	.182±.006	1180±77	11.21±.23	.289±.006
50 K^+p	2.22±.26	18.03	15.81±.26	.123±.014	1190±278	7.15±.69	.397±.038
70 K^+p	2.38±.09	18.36	15.98±.09	.130±.005	1093±82	7.88±.56	.429±.031
140 K^+p	2.35±.09	19.23	16.88±.09	.122±.005	1288±99	8.24±.45	.428±.023
175 K^+p	2.52±.09	19.59	17.07±.09	.129±.005	1183±85	8.58±.37	.438±.019

*Error is statistical uncertainty added in quadrature to estimated 3% systematic uncertainty.

**Error is statistical uncertainty added in quadrature to estimated 1 1/2% systematic uncertainty in slope.

Figure 37: S Dependence of Logarithmic Derivative b at $-t = .2$ GeV^2

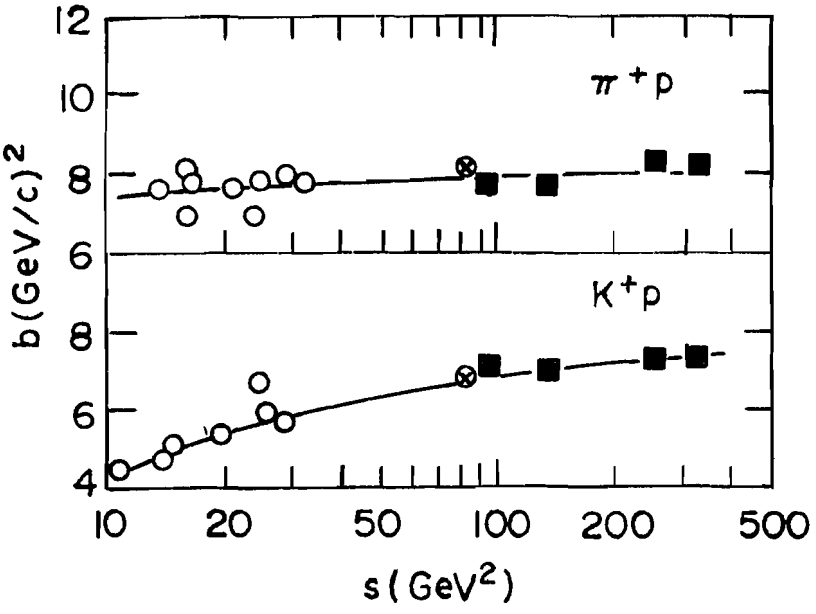

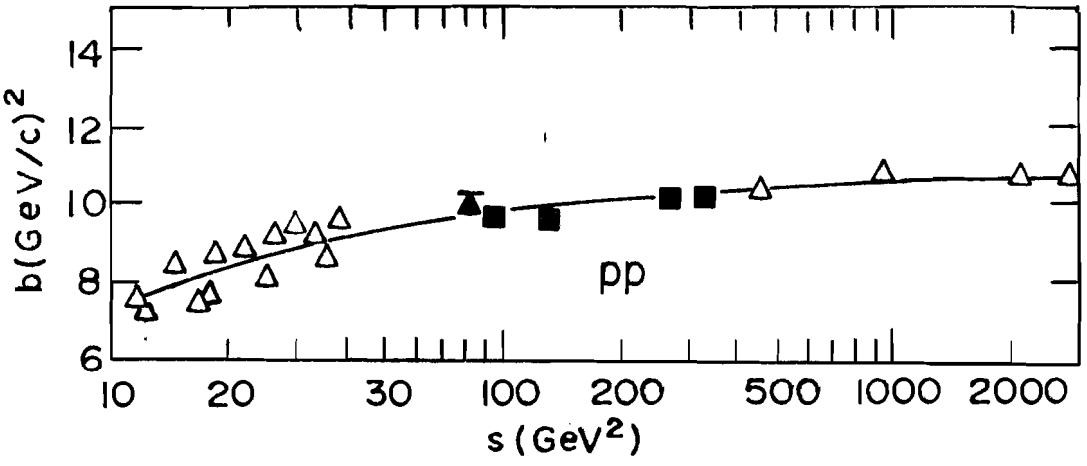

■ This experiment. (size of box represents uncertainty.)

△ ○ Ref. 5.

⊗ ▲ Ref. 14b.

▲ Ref. 14c.

CHAPTER X

PHYSICS DISCUSSION

A. GENERAL FEATURES OF THE ANGULAR DISTRIBUTION

Figures 34a, b, c, and d reveal smooth angular distributions for all the elastic processes throughout the whole energy range. No significant dips or bumps are visible. The differential cross sections are reasonably well described by the quadratic exponential. This implies that there is a linear variation of the slope or logarithmic derivative with t. We have also demonstrated that it is possible to obtain acceptable fits for limited t regions with simple exponentials.

Experimental evidence on proton-proton elastic scattering has suggested that a 'break' or rapid change in slope (logarithmic derivative) occurs in the vicinity of $-t = .1$ GeV^2 (15); Table 19 gives a comparison of the slopes in the low t ($-t < .10$) and high t ($.15 < -t < .50$) regions covered by this experiment. It is obvious that our data is not inconsistent with the presence of a break. The observed change of slope between the two regions is 1.5-2.0 GeV^{-2} for both pions and protons. It is, however, also true that the same net change of slope is compatible with the smooth variation described by a quadratic exponential with $C \simeq 2$ to 3.

The region around $-t = .1$ has been studied intensively at ISR energies by the ACGHT collaboration. They measured the cross section with large statistics ($\sim 10^6$ events) over the two t ranges $.05 < -t < .09$ and $.14 < -t < .24$. They state that their results are well described

by two simple exponentials with different slopes but are not well represented by a quadratic exponential. (A C coefficient of ~ 4 would be required to account for a change in slope of 2 GeV^{-2} between the two t-regions.)

It should be recognized that theoretical models which fit the data in this region reasonably well never have a true break or discontinuity in slope but rather a rapid, but continuous, change of slope. The true behavior of the cross section in this region is likely to be intermediate between the two parameterizations we have tried.

It seems clear that further experimental work will be required to determine the exact nature of the slope changes in pp, πP, and KP scattering near $-t = .1$. Additional analysis of our own data at 70 GeV/c (which has high statistics) may produce some new insights. Since we will probably need to distinguish between the two kinds of behavior on the basis of goodness-of-fit, additional study of the systematic errors will be necessary before definite conclusions can be made.

B. ENERGY DEPENDENCE OF SMALL T ELASTIC SCATTERING

1. Energy Dependence of the Slope Parameter

In the simple Regge pole model, the differential cross section for elastic scattering has the form

$$1) \qquad \frac{d\sigma}{dt} = F(t) \left(\frac{s}{s_o}\right)^{2\alpha(t)-2} .$$

Its logarithm is

$$2) \qquad \ell n \frac{d\sigma}{dt} = \ell n\, F(t) + \{2\alpha(t)-2\} \ell n \frac{s}{s_o}$$

and the logarithmic derivative is

$$3) \qquad b(t) = b_o(t) + 2\alpha'(t) \ln \frac{s}{s_o}$$

where

$$b_o(t) = \frac{d}{dt} \ln F(t) \ .$$

In order to study the s-dependence of slopes, one must be sure to use data taken over the same t-range so as not to confuse the s-dependence with the t-dependence. Table 18 shows that the strongest energy variation in $b(-t = .2)$ occurs for protons. The total change is $\Delta b = .7$ for $\Delta \ln s/s_o = 1.25$ (s_o is taken as 1 GeV^2). This implies an $\alpha' \simeq .25$. At lower energies the rate of shrinkage is greater: $\alpha' \sim .5$–$.6$. Thus, the energy variation in the neighborhood of $-t = .2$ is slowing down across the energy range of this experiment. For protons, $b(-.2)$ nearly attains the value, by 175 GeV/c, that is observed throughout the ISR range.

More insight into the s-dependence is obtained from the fits of Table 19. The slope parameters for the large t region ($.5 < -t < .50$) are, within statistics, energy independent for both pions and protons. The small t slopes show a clear energy dependence for protons, changing by nearly 15% from 50 to 175 GeV/c.

For pions, $b(-.2)$ changes at most by $\sim .3$ GeV^{-2} across our energy span. The statistics are such that it is difficult to decide whether there is no shrinkage or perhaps a very slight shrinkage. For K^+P, there is no doubt that there was rapid shrinkage of the forward peak between the low energy experiments and 50 GeV/c. Whether this shrinkage

persists across our range is difficult to say because of statistical limitations but there is not doubt that the rate of shrinkage has diminished.

2. S-dependence: Geometrical Sealing (G-S)

The hypothesis of geometrical scaling[30] has been proposed to explain the energy dependence of pp elastic scattering and total cross sections at ISR energies. The hypothesis is best stated in impact parameter space. If a(s,b) is the scattering amplitude, then the G-S hypothesis is

$$a(s,b) = a(b/R(s))$$

where R(s) is a radial scale or range parameter which contains all the energy dependence.

If such a range parameter exists, it can be shown that the differential cross section $d\sigma/dt$, the total cross section σ_T, the total inelastic cross section σ_{inel}, and the forward diffraction slope parameter B, depend on it in the following manner:

a. $d\sigma/dt = R^4 f\ (R^2 t)$

b. $\sigma_T \sim R^2$

c. $\sigma_{el} \sim R^2$

d. $\sigma_{inel} \sim R^2$

e. $B \sim R^2$

Since all the s-dependence is supposed to be in the parameter R, the following simple predictions are made:

$$\sigma_{el}/\sigma_T, \quad b/\sigma_T, \quad \text{and } \sigma_{inel}/\sigma_T$$

are all independent of energy.

Table 20 shows these three quantities determined from the fits of Table 18. Both K^+P and π^+P conform to G-S reasonably well. For pp, σ_{el}/σ_T falls in magnitude but by 140 GeV/c it has attained a ratio of $\sim$ .175 which is the value observed across the whole ISR energy range.

G-S also predicts (property 'a') that the function $1/\sigma_T^2$ $d\sigma/dt$ plotted against σ_T x t should be energy independent. We show in Figure 38 a comparison of K^+P at 70 and 175 GeV/c. The vertical axis is σ_T^2 (70)/σ_T^2 x $d\sigma/dt$ and the horizontal axis is $(\sigma_T/\sigma_T(70)$ x t. The data points belong to 175 GeV/c and the smooth curve belongs to 70 GeV/c. Thus, for K^+P, geometric scaling seems to occur at energies as low as 70 GeV/c. We made similar plots for PP and π^+P and found the G-S does not occur at 70 GeV/c for them.

Table 20 also evaluates the ratio σ_t^3/σ_{el}^2 which has been conjectured to be a constant independent of incident particle type. Although the errors are large, this conjecture seems to be confirmed.

Figure 38: Geometric Scaling Test for K^+P

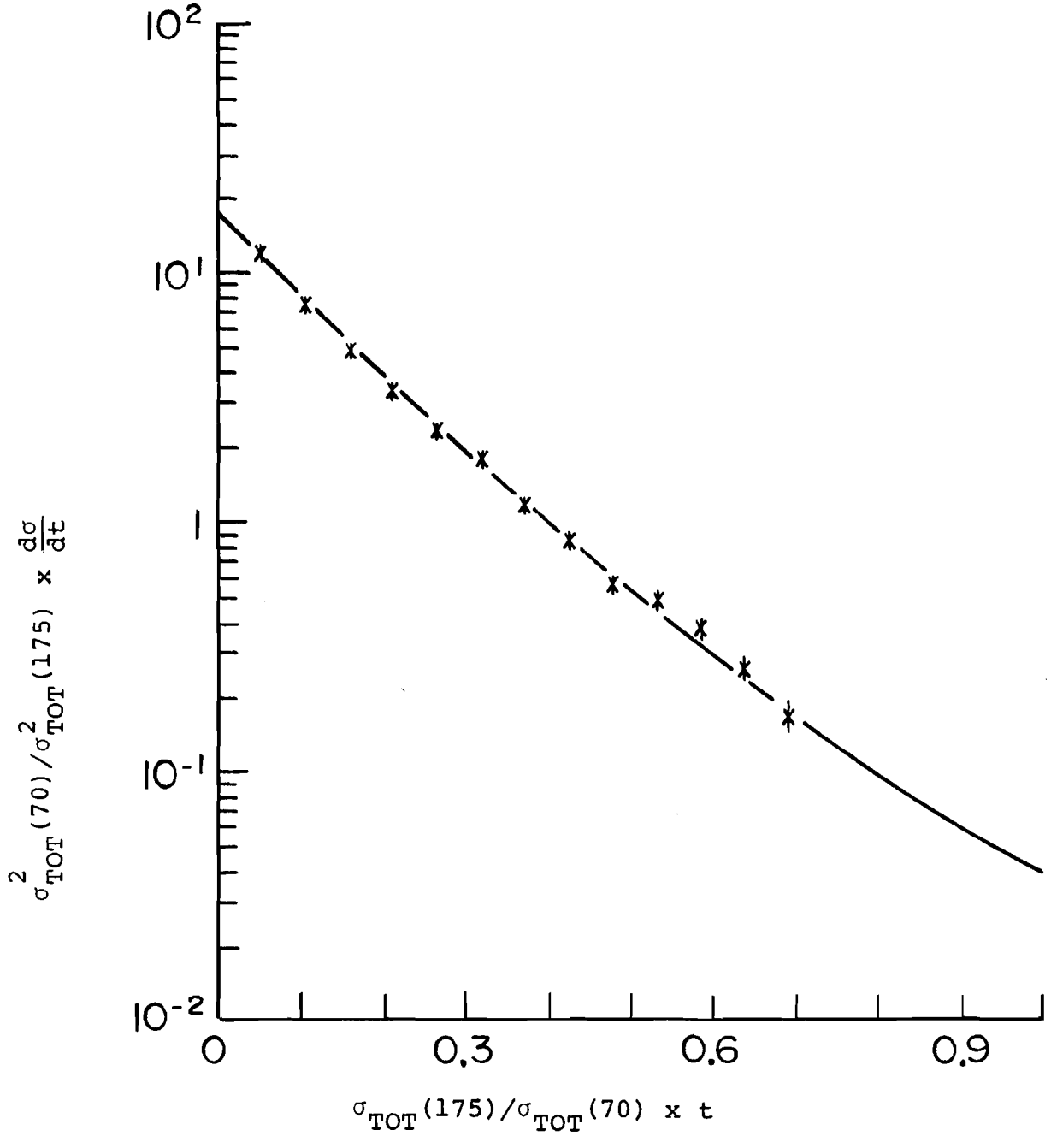

Smooth curve: 70 GeV/c K^+P

Data points: 175 GeV/c K^+P

3. Elastic Cross Sections in Impact Parameter Representation

We have calculated the amplitude a(s,b) for elastic scattering in impact parameter space according to the formulation of Appendix II for the 70 and 175 GeV/c data. For $d\sigma/dt$ we have used the quadratic exponential fits of Table 18 out to a t-value of $\sim$.-8. Beyond -t = .8, we have used a linear exponential which joins smoothly to the quadratic exponential at -t = .8. We have cut the linear exponential off at -t = 1.2. The effect of extrapolating past -t = .8 in this manner rather than just cutting the integration off there is to change the amplitude a(s,b) by a few percent at small b values. Since an analytic function obtained from fits has been used, details of the function a(s,b) are not very interesting so the results are not plotted. The shape is approximately Gaussian with some departures at b > 1 F. Of interest, however, are the central opacity a(s,0) and the range R in b-space of the amplitude which we take as the FWHM:

	R	a(s,0)		R	a(s,0)
70π	.6F	.61	175π	.6	.52
70K	.6F	.56	175K	.6	.55
70P	.7F	.78	175P	.7	.80

Our results indicate that none of the particles approach the black sphere limit a(s,0) = 1. The pion and the kaon look quite similar for b < 1F. The proton has a much larger central opacity and seems also to have a larger radius than either the pion or kaon.

FINAL REMARKS:

In this section, we have discussed the general behavior of the angular distributions and the energy dependence. Considerable insight will be gained from the detailed comparisons of particle and anti-particle cross sections outlined in Chapter 1. This awaits the conclusion of the analysis of the negative polarity data.

The discussion of this section indicates the importance of additional measurements of the shape of the differential cross section near $-t = .1\ GeV^2$. The questions are:

1) What is the true nature of the observed slope transition in pp elastic scattering?

2) Do the other elastic reactions also have breaks? In light of the discussion of Chapter 1, K^+P should behave similarly to PP.

3) How does this behavior change with energy?

The 'break' in pp scattering has received much theoretical attention and is considered an important feature of elastic scattering. It must certainly be associated with the rise in the total elastic cross section at ISR energies. It is, therefore, hoped that the answer to the above questions will be available soon.

BIBLIOGRAPHY

1. K. Fialkowski and H.I, Miettinen, Phys. Lett. 43B, 61 (1973).

   and

   H. Harari and E. Rabinovicci, Phys. Lett. 43B, 49 (1973).

2. See for example, V. Barger and D. Cline, Phenomenological Theories of High Energy Scattering, Chapters 3 and 5, W.A. Benjamin, Inc., New York.

3. D. Horn and E. Zachariasen, Hadron Physics at Very High Energies, Chapter 5, W.A. Benjamin, Inc., New York.

4. L. Van Hove, Rev. Mod. Phys., April, 657 (1964) and References 2 and 3 therein.

5. Lasinski, Nucl. Phys. B37, 1 (1972).

6. Elastic Hadronic Processes, Duality and Absorption, Ann. Phys. (NY) 63, 432 (1971).

7. R. Dolen, D. Horn, and C. Schmid, Phys. Rev. 166, 1768 (1969).

8. M. Davier, H. Harari, Elastic $K^{\pm}P$ Scattering and A Dual Absorptive Model, SLAC-PUB-893 (March, 1971).

9. Aachen, CERN, Geneva, Harvard, Turrin Collaboration. Data presented at the Chicago Conference, 1972.

10. See for example, T.T. Chou, C.N. Yang, Phys. Rev. 170, 1591 (1968).

11. F. Henyey, R.H. Tuan, G.L. Kane, Nucl. Phys. B70, 445 (1974).

12. U. Amaldi et al., Phys. Lett. 44B, 112 (1973). S. Amendolia et al., ibid., 44B, 119 (1973).

13. H.I. Miettinen, Geometrical Description of Hadronic Collisions, Ref. Th. 1906, CERN.

14. A partial list of elastic scattering experiments of positive hadrons in the t range from $\sim$ .05 to 1.0 is:

    a. Ambats, Phys. Rev. D9, 1179 (1974).
    b. Antipov, Preprint, XVII Int. Conf. London, (1974).
    c. Barbiellini, Phys. Lett. 39B, 663 (1972).
    d. Barish, Phys. Rev. D9, 1171 (1974).
    e. Bromberg, Phys. Rev. Lett. 31, 1563 (1973).
    f. Cork, Phys. Rev. 107, 859 (1957).

g. Edelstein, Phys. Rev. D5, 1073 (1972).
h. Foley, Phys. Rev. Lett. 11, 425 (1963).
i. Foley, Phys. Rev. Lett. 11, 503 (1963).
j. Foley, Phys. Rev. Lett. 15, 45 (1965).
k. Harting, Nuovo Cimento 38, 60 (1965).
l. Holder, Phys. Lett. 36B, 400 (1971).
m. Jain, Nucl. Phys. B19, 568 (1970).

15. Barbiellini et al., Phys. Lett. 39B, 663 (1972).

16. Bartenev et al., Phys. Rev. Lett. 31, 1088 (1973).

17. Transport, SLAC-PUB 391 and #75.

18. D. Ayres, et al., Single Arm Spectrometer Facility Threshold Cerenkov Counter Operating Instructions, (ANL, 1974), unpublished.

19. R. Anderson and J. Grant, "A Design of a Differential Cerenkov Counter for Use at High Momentum", to be published.

20. M. Benot et al., Nucl. Instrum. Methods 105, 431 (1972).

21. E.F. Anelli et al., Multiwire Proportional Chambers and Computer Interface Design (BARI, 1971), unpublished.

22. Weitsch, A., Multiple Scattering and Resolution in the FNAL Single Arm Spectrometer (unpublished).

23. Bartenev et al., Phys. Rev. Lett. 31, 1367 (1973).

24. G.B. West and D.R. Yennie, Phys. Rev. 172, 1413 (1968).

25. Carroll et al., Phys. Rev. Lett. 33, 928 (1974).

26. Carroll et al., Phys. Rev. Lett. 33, 932 (1974).

27. M.R. Sogard, Phys. Rev. D9, 1486 (1974).

28. Sidhu, D.P, and Sukhatme, U.P., Real Parts of Forward Elastic Hadronic Amplitudes, BNL-19140.

29. Carrigan, R.A., Phys. Rev. Lett. 24, 168 (1970).

30. A.J. Buras and J. Dias de Deus, Nucl. Phys. B71, 481 (1974).

APPENDIX I

We present below all the individual cross section values used in the fits presented in Table 18. These points have all been multiplied by a scale factor of 1.03 as expalined in the text. The uncertainties are statistical only. Fits to the coarse grid data of Table 17 produce essentially identical results to the fits to the points in these tables. In some cases, the χ^2 of the fits is improved by using the coarse grid data because the systematic errors and binning effects get averaged out by the rebinning.

It should be noted that both sets of data have been corrected for finite bin size and resolution effects so that they represent cross sections at specific t-values. For π^+P and PP the data plotted in Figure 34 is the data of this Appendix. This is also true for K^+P at 175 GeV/c. The K^+P data plotted in Figure 34 at 50, 70 and 140 GeV/c is taken from Table 17 to avoid a confusion of points with low statistical accuracy.

ELASTIC CROSS SECTIONS

PION AT 50.00 GEV/C

T	DSIG/DT	ERROR
GEV**2	MB/GEV**2	MB/GEV**2
0.02102	23.84435	2.21533
0.02559	23.13104	1.99600
0.03061	21.09195	1.91974
0.03609	17.94473	1.65984
0.04201	18.23354	1.64038
0.04837	18.00235	1.59597
0.05519	15.22545	1.75844
0.06246	14.16065	1.87463
0.03609	20.61987	1.05373
0.04201	19.29947	0.83972
0.04837	17.44833	0.75765
0.05519	17.34146	0.75263
0.06246	14.95172	0.69206
0.07017	15.72543	0.69353
0.07833	14.00368	0.65191
0.08694	12.17852	0.63124
0.09600	11.18938	0.68837
0.07017	13.58255	0.73494
0.07833	13.79065	0.57382
0.08694	12.31030	0.52762
0.09600	11.94714	0.50445
0.10551	9.98506	0.47747
0.11546	9.62542	0.46185
0.12586	8.21017	0.44249
0.13670	7.46770	0.39741
0.14799	7.36906	0.47546
0.11546	11.05671	0.65492
0.12586	9.24152	0.44454
0.13670	8.89393	0.41251
0.14799	7.82071	0.39039
0.15973	7.30346	0.37323
0.17191	7.11963	0.37451
0.18454	6.23798	0.33776
0.19761	4.86244	0.31655
0.21112	5.00684	0.34385
0.17191	5.99085	0.45654
0.18454	5.53396	0.37887
0.19761	5.07241	0.36291
0.21112	4.84247	0.33655
0.22508	3.93229	0.30602

0.23949	3.74553	0.30115
0.25433	3.04736	0.26664
0.26962	3.33244	0.29368
0.28535	2.55374	0.30945
0.23949	3.63851	0.21798
0.25433	3.49452	0.17396
0.26962	3.01479	0.15433
0.28535	2.88702	0.15072
0.30153	2.32077	0.13408
0.31814	2.03413	0.12329
0.33520	1.86040	0.12119
0.35269	1.76735	0.12288
0.37063	1.43725	0.12603
0.31814	1.81145	0.15666
0.33520	1.72907	0.13090
0.35269	1.56235	0.12284
0.37063	1.40851	0.11872
0.38900	1.25350	0.10250
0.40782	1.07376	0.09612
0.42707	1.13194	0.09830
0.44676	0.89186	0.09503
0.46689	0.62154	0.09227
0.40782	1.05838	0.10550
0.42707	1.03807	0.08885
0.44676	0.63826	0.08708
0.46689	0.78554	0.07469
0.48745	0.73761	0.07347
0.50845	0.66524	0.07471
0.52989	0.50473	0.06774
0.55176	0.38810	0.05432
0.57407	0.45174	0.06699
0.50845	0.51180	0.06205
0.52989	0.48977	0.05049
0.55176	0.37854	0.04221
0.57407	0.31298	0.03808
0.59680	0.28169	0.03649
0.61998	0.24555	0.03391
0.64358	0.22541	0.03230
0.66761	0.22401	0.03378
0.69208	0.26159	0.04270

ELASTIC CROSS SECTIONS

NUCLEON AT 50.00 GEV/C

T	DSIG/DT	ERROR
GEV**2	MB/GEV**2	MB/GEV**2
0.02102	60.13625	4.69944
0.03061	54.93564	3.97353
0.03609	53.11682	3.79744
0.04201	54.89565	3.88555
0.04837	48.45677	3.63069
0.05519	37.61456	3.71622
0.03609	47.86470	2.39399
0.04201	48.60469	1.91572
0.04837	47.32999	1.79103
0.05519	43.29204	1.66812
0.06246	38.88934	1.60626
0.07017	36.32541	1.51563
0.07833	36.94058	1.54881
0.08694	31.35722	1.45080
0.09600	28.08360	1.58075
0.07017	36.81297	1.59837
0.07833	34.98711	1.31298
0.08694	30.60550	1.24174
0.09600	30.52896	1.14717
0.10551	26.32208	1.10860
0.11546	24.74399	1.06131
0.12586	22.55951	1.03729
0.13670	19.62885	0.96906
0.14799	18.40709	1.04012
0.11546	21.30530	1.40578
0.12586	21.35252	1.08899
0.13670	18.44949	0.99206
0.14799	15.66145	0.90544
0.15973	14.12445	0.84601
0.17191	14.32539	0.84919
0.18454	12.71437	0.78980
0.18454	12.71437	0.78980
0.19761	10.05594	0.70401
0.21112	10.04246	0.79559
0.17191	12.80948	1.29049
0.18454	11.37566	1.03819
0.19761	10.55337	0.98842
0.21112	10.06174	0.96239
0.22508	7.09118	0.81925
0.23949	6.02467	0.75650

0.25433	5.85421	0.67744
0.26962	6.73252	0.79026
0.28535	5.36022	0.83536
0.23949	7.64377	0.62615
0.25433	6.69627	0.46916
0.26962	5.10629	0.41787
0.28535	4.57202	0.37451
0.30153	3.73520	0.34055
0.31814	3.36044	0.33777
0.33520	2.51793	0.27799
0.35269	2.30646	0.27788
0.37063	1.89789	0.29335
0.31814	3.72538	0.44597
0.33520	2.91982	0.35124
0.35269	2.48110	0.28668
0.37063	2.37004	0.27957
0.38900	1.92409	0.25070
0.40782	1.56570	0.22619
0.42707	1.50668	0.22241
0.44676	1.16408	0.20347
0.46689	0.84950	0.20425
0.40782	1.48566	0.29475
0.42707	1.27362	0.19474
0.44676	1.01770	0.16629
0.46689	0.74795	0.14171
0.48745	0.65064	0.12766
0.50845	0.55406	0.12322
0.52989	0.70972	0.13444
0.55176	0.55279	0.12533
0.57407	0.27722	0.09831

ELASTIC CROSS SECTIONS

KAON AT 50.00 GEV/C

T	DSIG/DT	ERROR
GEV**2	MB/GEV**2	MB/GEV**2
0.02325	12.90067	2.94268
0.02805	8.81446	2.23241
0.03329	15.31196	2.53448
0.03899	11.64266	1.95798
0.04513	10.50213	1.72351
0.05173	8.74832	1.74850
0.04513	11.48383	1.92937
0.05173	11.17793	1.99277
0.05877	13.82201	2.06458
0.06626	11.41883	1.82296
0.07420	11.61936	1.84337
0.08258	10.06616	1.71961
0.05877	12.03291	1.49752
0.06626	9.31774	1.80376
0.07420	10.41598	1.44910
0.08258	9.97079	1.54132
0.09142	8.31328	1.45940
0.10070	7.57484	1.41784
0.11043	8.94877	1.52697
0.12060	5.47000	0.97148
0.13122	7.03215	1.11224
0.14229	6.15628	1.19408
0.15380	4.65318	0.89869
0.16576	3.32549	0.77649
0.10070	7.93409	1.32387
0.11043	7.42342	1.27304
0.12060	5.70602	1.19203
0.13122	5.88172	1.18214
0.14229	7.50421	1.27427
0.15380	4.68128	1.09840
0.16576	3.75549	0.98760
0.17817	6.58214	1.33215
0.19102	5.23926	1.06778
0.20431	3.55131	0.87297
0.21805	4.17707	0.95160
0.23223	2.67204	0.78186
0.15380	7.41378	1.84431
0.16576	2.16427	0.95172
0.17817	3.99799	1.30247
0.19102	5.71813	1.55163

0.20431	6.02065	1.63684
0.21805	4.64515	1.61269
0.23223	4.03873	1.36032
0.24685	1.53577	0.82121
0.26192	3.34352	1.09061
0.27743	2.62478	0.93225
0.29339	2.66959	1.02650
0.30978	2.64522	1.23082
0.21805	4.00307	0.68568
0.23223	3.53707	0.61471
0.24685	2.63575	0.53300
0.26192	2.61855	0.51989
0.27743	2.08965	0.47248
0.29339	2.16434	0.46742
0.30978	1.78616	0.43850
0.32661	1.17441	0.34208
0.34389	1.48511	0.40209
0.36161	1.69806	0.41879
0.37976	0.82964	0.29609
0.39836	1.72316	0.45485
0.29339	2.12960	0.55654
0.30978	1.79019	0.52277
0.32661	2.37723	0.62421
0.34389	0.41708	0.24174
0.36161	1.83511	0.51764
0.37976	0.84824	0.34955
0.39836	1.18711	0.40121
0.41739	0.72047	0.32538
0.43686	0.52486	0.26463
0.45677	1.20891	0.43601
0.47712	0.73825	0.33509
0.49790	0.45389	0.26471
0.37976	0.66947	0.27732
0.39836	0.89595	0.32044
0.41739	1.23623	0.38165
0.43686	0.62853	0.26092
0.45677	0.82836	0.32016
0.47712	1.31889	0.37898
0.49790	0.64557	0.24945
0.51912	0.31210	0.18186
0.54077	0.42088	0.21355
0.56286	0.19260	0.13725
0.58538	0.32489	0.19165
0.60834	0.10403	0.10462
0.47712	0.34804	0.17839
0.49790	0.34447	0.15793
0.51912	0.36743	0.16924
0.54077	0.37166	0.17135
0.56286	0.18117	0.10552
0.58538	0.41279	0.17427
0.60834	0.18438	0.10764

ELASTIC CROSS SECTIONS

PION AT 69.50 GEV/C

T	DSIG/DT	ERROR
GEV**2	MB/GEV**2	MB/GEV**2
0.02599	21.65036	1.43594
0.03314	22.25818	1.07764
0.04116	19.82658	0.98425
0.05005	16.92805	0.86851
0.05981	17.30432	0.83580
0.07044	13.47253	0.77196
0.08193	12.81551	0.71812
0.09429	11.38381	0.68189
0.10751	10.55989	0.73661
0.05350	19.17963	0.89927
0.06357	15.63064	0.70847
0.07451	15.21146	0.69108
0.08631	14.47426	0.67956
0.09898	11.99633	0.61588
0.11252	9.50865	0.52917
0.12692	8.60479	0.51424
0.14219	7.84808	0.49484
0.15832	6.53620	0.53020
0.11273	10.56303	0.31075
0.12715	9.36730	0.25016
0.14243	8.00150	0.23563
0.15857	7.00929	0.21305
0.17558	6.34901	0.20400
0.19344	5.69232	0.18731
0.21218	4.58776	0.17149
0.23177	4.06218	0.15739
0.25222	3.42979	0.16751
0.29752	2.58726	0.07287
0.32061	2.12430	0.05768
0.34457	1.82152	0.05256
0.36937	1.53453	0.04748
0.39504	1.35675	0.04554
0.42155	1.04677	0.03959
0.44892	0.83885	0.03473
0.47715	0.66442	0.03060
0.50622	0.53851	0.03297
0.42215	1.13467	0.05720
0.44954	0.85798	0.04533
0.47778	0.76097	0.03751
0.50687	0.62334	0.03779

0.53681	0.45413	0.03061
0.56759	0.36119	0.02946
0.59923	0.30079	0.02313
0.63171	0.30356	0.02562
0.66503	0.23238	0.02616

ELASTIC CROSS SECTIONS

NUCLEON AT 69.50 GEV/C

T	DSIG/DT	ERROR
GEV**2	MB/GEV**2	MB/GEV**2
0.02599	56.98218	3.02781
0.03314	54.78424	2.40379
0.04116	49.74652	2.10174
0.05005	46.97334	1.98521
0.05981	41.96539	1.83868
0.07044	35.26762	1.66869
0.08193	34.38490	1.62516
0.09429	26.27988	1.48827
0.10751	25.28865	1.72488
0.05350	44.14133	1.41646
0.06357	37.99785	1.15513
0.07451	34.11572	1.07738
0.08631	31.98164	1.02931
0.09898	25.43094	0.93410
0.11252	22.81372	0.87965
0.12692	18.84981	0.80270
0.14219	15.87244	0.73404
0.15832	14.13372	0.81801
0.11273	24.72856	0.70489
0.12715	21.48569	0.56148
0.14243	17.45715	0.50521
0.15857	15.37789	0.45843
0.17558	12.64343	0.41783
0.19344	11.52382	0.38542
0.21218	8.88080	0.34729
0.23177	7.29551	0.31562
0.25222	5.91152	0.31452
0.29752	3.91577	0.13256
0.32061	3.29061	0.10047
0.34457	2.47114	0.08938
0.36937	1.93011	0.07890
0.39504	1.63636	0.06589
0.42155	1.32542	0.06321
0.44892	0.95272	0.05727
0.47715	0.78388	0.05147
0.50622	0.49092	0.04824
0.42215	1.24928	0.08655
0.44954	1.10175	0.06899
0.47778	0.65929	0.05638
0.50687	0.67109	0.05123

0.53681	0.53423	0.04780
0.56759	0.39290	0.03997
0.59923	0.23722	0.03350
0.63171	0.19529	0.02690

ELASTIC CROSS SECTIONS

KAON AT 69.50 GEV/C

T	DSIG/DT	ERROR
GEV**2	MB/GEV**2	MB/GEV**2
0.02946	14.02399	1.30904
0.03704	13.57134	1.22448
0.04550	13.36996	1.16706
0.05483	12.74101	1.07714
0.06502	9.68729	1.04783
0.07607	9.66631	1.03862
0.08800	7.86267	0.87477
0.10079	7.13660	0.85474
0.11983	7.54393	0.54622
0.13468	6.18655	0.53617
0.15039	5.84894	0.52609
0.16696	4.79880	0.52632
0.18440	5.04853	0.46459
0.20270	3.47002	0.41310
0.22186	3.39701	0.38203
0.24188	3.28250	0.38193
0.30896	1.99759	0.23707
0.33248	1.39056	0.21631
0.35686	1.45324	0.21613
0.38210	1.30379	0.18508
0.40819	0.99423	0.17461
0.43513	0.98987	0.15387
0.46293	0.35644	0.14340
0.49158	0.89266	0.14316
0.05842	11.23937	1.02643
0.06893	9.59871	0.95576
0.08030	9.95731	0.94636
0.09254	8.19402	0.80293
0.10564	8.63167	0.85492
0.11961	7.02858	0.80386
0.13445	6.32055	0.75269
0.15015	5.28154	0.68083
0.43574	0.75905	0.15386
0.46355	0.33799	0.10242
0.49222	0.82821	0.16359
0.52173	0.43881	0.11226
0.55209	0.28103	0.09673
0.58331	0.50478	0.12492
0.61536	0.28357	0.09621
0.64827	0.33311	0.10600

ELASTIC CROSS SECTIONS

PION AT 138.60 GEV/C

T	DSIG/DT	ERROR
GEV**2	MB/GEV**2	MB/GEV**2
0.04179	20.33752	0.75090
0.05388	18.06731	0.69228
0.06752	15.92040	0.63659
0.08268	13.18267	0.58126
0.09938	12.00900	0.55847
0.11762	10.03451	0.50915
0.13739	7.90817	0.45583
0.15868	7.27914	0.42983
0.18151	6.20902	0.40376
0.20588	5.15427	0.35956
0.23176	3.86278	0.31565
0.25918	2.87790	0.29073
0.12001	10.08521	0.56530
0.13996	8.46896	0.32138
0.16145	7.16383	0.24988
0.18448	6.05928	0.21815
0.20903	4.56019	0.19061
0.23511	3.99352	0.17508
0.26272	2.95538	0.15392
0.29186	2.51062	0.14426
0.32252	1.88254	0.12360
0.35471	1.66261	0.11009
0.38842	1.28664	0.09880
0.42366	0.80896	0.07855
0.46041	0.74422	0.07948
0.49869	0.59391	0.07058
0.40585	1.02205	0.05093
0.44184	0.82518	0.04575
0.47936	0.61589	0.03846
0.51840	0.52265	0.03427
0.55896	0.39285	0.03031
0.60103	0.26632	0.02622
0.64462	0.22136	0.02537
0.68972	0.20401	0.02015
0.73634	0.16362	0.01777
0.78447	0.11090	0.01444
0.83410	0.07194	0.01187

ELASTIC CROSS SECTIONS

NUCLEON AT 138.60 GEV/C

T	DSIG/DT	ERROR
GEV**2	MB/GEV**2	MB/GEV**2
0.04179	49.32886	1.62367
0.05388	39.55704	1.41181
0.06752	35.45720	1.33546
0.08268	28.27986	1.20726
0.09938	26.31747	1.15268
0.11762	20.27910	1.02550
0.13739	15.10361	0.84209
0.15868	13.55744	0.82071
0.18151	9.30038	0.67882
0.20588	7.05803	0.60252
0.23176	5.71992	0.56824
0.25918	4.61180	0.55837
0.13996	15.06264	0.49879
0.16145	11.98671	0.37080
0.18448	10.00478	0.32451
0.20903	8.31864	0.29157
0.23511	6.49993	0.25651
0.26272	4.63739	0.21548
0.29186	3.55576	0.18976
0.32252	2.57434	0.16087
0.35471	1.96327	0.13814
0.38842	1.23955	0.11182
0.42366	1.09071	0.10499
0.46041	0.68718	0.08089
0.49869	0.65822	0.08575
0.40585	1.23532	0.04862
0.44184	0.82076	0.04426
0.47936	0.63733	0.03638
0.51840	0.43330	0.03783
0.55896	0.31466	0.02406
0.60103	0.20491	0.01936
0.64462	0.14117	0.01619
0.68972	0.09578	0.01436
0.73634	0.07184	0.01158
0.78447	0.06426	0.01057

ELASTIC CROSS SECTIONS

KAON AT 138.60 GEV/C

T	DSIG/DT	ERROR
GEV**2	MB/GEV**2	MB/GEV**2
0.04200	10.25736	0.99852
0.05400	10.57869	0.92654
0.06800	11.65481	0.93109
0.08300	11.11316	0.86773
0.09900	8.23595	0.78458
0.11800	8.52011	0.81394
0.13700	5.16137	0.58286
0.15900	5.34706	0.62497
0.18200	5.07812	0.58739
0.20600	3.35477	0.47023
0.23200	3.28861	0.52058
0.10200	8.75095	0.69584
0.12000	6.55187	0.57258
0.14000	6.22537	0.56660
0.16100	4.81869	0.50771
0.18400	5.31803	0.52347
0.20900	4.47520	0.46175
0.23500	2.71064	0.37855
0.26300	2.29722	0.33391
0.29200	1.40723	0.25295
0.32300	1.57852	0.26826
0.35500	1.00879	0.30180
0.38800	1.45278	0.27492
0.42400	0.74173	0.18095
0.46000	0.67070	0.18166
0.27700	2.15235	0.13354
0.30700	1.73434	0.11423
0.33800	1.34206	0.09823
0.37100	1.27311	0.09578
0.40600	0.84269	0.07245
0.44200	0.78221	0.06994
0.47900	0.62370	0.07227
0.51800	0.53354	0.06555
0.55900	0.32471	0.04683
0.60100	0.28761	0.04551
0.64500	0.24730	0.04660

ELASTIC CROSS SECTIONS

PION AT 172.80 GEV/C

T	DSIG/DT	ERROR
GEV**2	MB/GEV**2	MB/GEV**2
0.05890	16.87776	0.37401
0.07680	14.85682	0.31176
0.09710	12.56122	0.27496
0.11990	9.94996	0.23822
0.14500	8.17919	0.21008
0.17260	6.08077	0.18208
0.20250	4.84425	0.16435
0.23480	3.83766	0.14090
0.26950	2.86849	0.12591
0.30650	2.09338	0.10929
0.34600	1.72592	0.09746
0.19450	5.33054	0.15968
0.22610	4.25878	0.08754
0.26020	3.27787	0.06657
0.29670	2.36307	0.05852
0.33550	1.74919	0.05136
0.37670	1.29502	0.04486
0.42040	0.93462	0.03490
0.46640	0.70687	0.03004
0.51480	0.52371	0.02632
0.56550	0.33691	0.02185
0.61870	0.27805	0.01809
0.67400	0.16774	0.01624
0.73160	0.12279	0.01241

ELASTIC CROSS SECTIONS

NJCLEON AT 172.80 GEV/C

T	DSIG/DT	ERROR
GEV**2	MB/GEV**2	MB/GEV**2
0.05890	39.48097	0.90467
0.07680	33.22594	0.78913
0.09710	25.40118	0.65073
0.11990	21.77963	0.57695
0.14500	15.86981	0.49906
0.17260	10.99831	0.41219
0.20250	8.32492	0.36756
0.23480	5.82485	0.31019
0.26950	4.43650	0.26231
0.30650	2.98080	0.22237
0.34600	2.53310	0.19304
0.22610	6.62856	0.09787
0.26020	4.82447	0.07329
0.29670	3.33167	0.06007
0.33550	2.35929	0.05117
0.37670	1.54894	0.04176
0.42040	1.02045	0.03330
0.46640	0.64094	0.02758
0.51480	0.41803	0.02365
0.56550	0.24529	0.01894
0.61870	0.19268	0.01383
0.67400	0.10486	0.01129
0.73160	0.07266	0.00933

ELASTIC CROSS SECTIONS

KAON AT 172.80 GEV/C

T	DSIG/DT	ERROR
GEV**2	MB/GEV**2	MB/GEV**2
0.05890	13.05160	0.69023
0.07680	9.92254	0.54370
0.09710	8.67724	0.48091
0.11940	7.69471	0.44955
0.14500	6.13800	0.39735
0.17260	4.48713	0.37654
0.20250	3.76652	0.31388
0.23480	3.06371	0.29278
0.26950	2.42404	0.25076
0.26020	2.49772	0.11496
0.29670	2.11957	0.10441
0.33530	1.48092	0.07300
0.37670	1.16628	0.07289
0.42040	0.83145	0.06236
0.46640	0.59096	0.05184
0.51480	0.51680	0.04134
0.56550	0.40157	0.04119
0.61870	0.27362	0.03074
0.67400	0.17117	0.03057

Appendix 2

Impact Parameter Representation of Elastic Scattering Data

At high energies, the scattering amplitude is known to be primarily imaginary and non spin-flip. The square root of the elastic cross section is, therefore, a good approximation to the scattering amplitude.

The normalization of the scattering amplitude is fixed by its relation to the differential cross section:

$$d\sigma/d\Omega = |f(\theta)|^2 \sim (f(\theta))^2 \quad (\theta \text{ in c.M.})$$

The partial wave decomposition of the scattering amplitude is

$$f(\theta) = \sum_{\ell=0}^{\infty} (2\ell+1) \frac{e^{2i\delta_\ell}-1}{2i\ K_{cm}} P_\ell(\cos\theta)$$

where $K_{cm} = p_{cm}/\hbar$ (de Broglie relation). The scattering angle is related to t by

$$\cos\theta = 1 + t/2p_{cm}^2.$$

The angular momentum is related to the impact parameter b:

$\ell = Kb$. For small angles, the LeGendre polynomial can be approximated as follows:

$$P_\ell(1 + t/2p_{cm}^2) = J_0(\ell\sqrt{-t}/p_{cm}) = J_0(b/\hbar c \cdot c\sqrt{-t}).$$

At FNAL energies, many partial waves contribute to elastic scattering so that the sum over ℓ can be changed to an integral.

$$f(\theta) = \sqrt{d\sigma/d\Omega} = \sqrt{d\sigma/dt\ p_{cm}^2/\pi} = \frac{K_{cm}}{i} \int_0^\infty b\ db\ a_b(s)\ J_0\ (b/\hbar c \cdot c\sqrt{-t})$$

where the function $a_b(s) = (e^{2i\delta_b} - 1)$.

This expression can be inverted to obtain $a_\ell(s)$ by using the orthogonality condition

$$\int_0^\infty J_0(x\theta)J_0(x'\theta)\theta d\theta = 1/x\ \delta\ (x-x')$$

The result is

$$a_b(s) = -i/\hbar c\sqrt{\pi} \int_0^\infty d(c\sqrt{-t})\ (c\sqrt{-t})J_0(b/\hbar c \cdot c\sqrt{-t})\ \sqrt{d\sigma/dt}$$

If b is in Fermis then $d\sigma/dt$ must be in $(\text{Fermi})^2/\text{GeV}^2$.

$a_b(s)$ may assume a maximum absolute value of 2. The 'black sphere limit' has a purely imaginary scattering angle, that is,

$e^{2i\delta_\ell} = 0$ so that $|a_b(s)| = 1$.

y_p, ϕ_p is any of the infinite family of rectangles which can be inscribed in this polygon. Two possible uniform acceptance regions are shown in Figure A3c. One emphasizes y_p acceptance at the cost of ϕ_p acceptance and the other reverses this situation.

The assumption of square quadrupoles is very restrictive. A much better calculation results from choosing a set of horizontal acceptances (perhaps based on method 2) and propagating this phase space through all the quads. The horizontal size Δx in each quad is used to choose the width of an inscribed rectangle (not necessarily a square). The vertical height of this rectangle is given by $y/2 = \sqrt{R^2 - (\Delta x/2)^2}$ where R is the radius of the vacuum pipe. See Figure 3Ad. This produces a different vertical height for the effective aperture in each quad and introduces into the model the interaction between the vertical and horizontal acceptance, while retaining the simple form of the boundary which makes the calculation very easy. A similar treatment of the horizontal acceptance is complicated by the momentum dispersion which adds a third dimension to the problem. This calculation was also carried out.

Figure A3: Model Acceptance Calculation

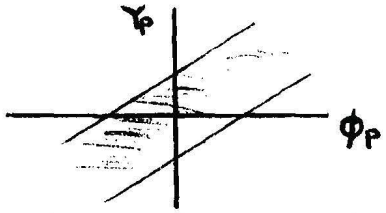

$$\pm\Delta Y = R_{33}Y_p + R_{34}\phi_p$$

a. Projection of a single rectangular aperture on the ϕ_p-Y_p plane.

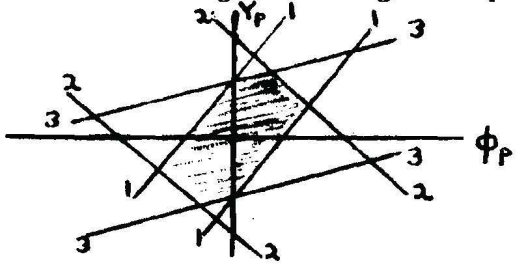

b. Projection of several (3) rectangular apertures on ϕ_p-Y_p plane (shaded area is the acceptance).

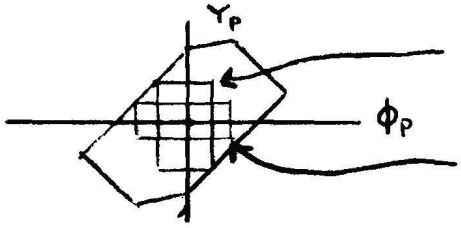

c. Two choices of uniform acceptance region.

side of square is $\sqrt{2}$ R

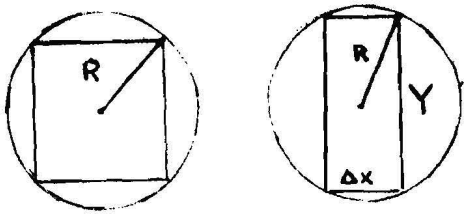

ΔX is 'known' horizontal size at quadrupole. height of rectangle + Y

$$Y = 2\sqrt{R^2 - (\Delta X/2)^2}$$

d. Two models for quadrupole apertures. 1 uses a square of fixed dimension. 2 fixes the horizontal phase space at the target, then traces it to the quad. The size ΔX of the phase space in the horizontal plane determines an inscribed rectangle which approximates the quad aperture.

ACKNOWLEDGEMENTS

Many people contributed to the construction of the Single Arm Spectrometer Facility and the successful execution of Experiment 96. I would like to thank all the members of the collaboration and their technical support staffs for their contributions and for the many things that they taught me. The exposure to many different approaches and styles of doing physics is one of the great advantages of participating in such a large effort.

This experiment could not have been accomplished without the efforts of the people who constructed the synchrotron and the experimental areas and those who are responsible for their operation and maintenance. Their achievements can hardly be overstated. I want particularly to thank the Meson Area staff, John Satti, the engineer for the beam and spectrometer, and Stan Ecklund, the M6 beam line physicist. I thank Travis Minto for his technical support.

I would like to thank Dr. David Ritson, the spokesman for our collaboration, for his efforts on behalf of the experiment and for many useful discussions about the data analysis. Dr. Michael Sogard instructed me on many aspects of the analysis, especially those concerned with radiative effects and other corrections to the cross sections. Drs. John Elias, Andreas Weitsch, and Al Brenner helped get me oriented when I first arrived at NAL.

Lorne Levinson and James Fines are also doing their graduate research on this experiment. Their participation was crucial to the successful execution of the experiment and their friendship helped to soften the sometimes arduous conditions under which we worked.

Dr. Robert Lanou has helped me and taught me throughout my graduate career. I am especially indebted to him for his excellent compilation of world data on elastic scattering.

Thanks are due to Drs. Henry Kendall, Jerome Friedman, and Lawrence Rosenson and their groups for their work on the experiments. Tom Lyons helped me with my chores during the installation period and performed the challenging task of maintaining and improving the apparatus during the experiment. Dr. Robin Verdier wrote most of the analysis program. Without his help in both the computing and the physics, the analysis presented here would be a long way from completion. Drs. Bruce Nelson, Don Barton, and Michael Marx have been advisors, associates, and friends and have helped me in many ways during my graduate education.

Dr. Lawrence Rosenson, my thesis supervisor, was a source of inspiration and encouragement throughout my graduate education. His strong participation in the analysis helped it to converge rapidly. His insistence on quantitative justification for every approximation I wanted to make prevented many serious mistakes.

My wife Paula has been a source of love and support throughout my graduate education. She has borne with tolerance and understanding the hardships imposed on our personal life by my work.

BIOGRAPHICAL NOTE

The author was born [redacted] in [redacted]. He received his secondary education at [redacted]. He entered Harvard University in 1965 and received his B.A. in Physics, Summa Cum Laude, in June 1969. While at Harvard, he was elected to Phi Beta Kappa. The author has been associated with the Rosenson Group since his entrance into M.I.T. in September 1969. For his first two years at M.I.T., he worked as a teaching assistant at the Educational Research Center. The last three and one half years were spent working on the setup, running, and analysis of the experiment described herein. The author is married to the former Paula Levenstein and lives in Boston.